CHALMERS
UNIVERSITY OF TECHNOLOGY

On SPMSM rotor position estimation from standstill and for low speeds

Evaluation of techniques for estimating position and speed of an SPMSM

Master's thesis in Electric Power Engineering

VICTOR JOHANSSON

Department of Electrical Engineering
CHALMERS UNIVERSITY OF TECHNOLOGY
Gothenburg, Sweden 2018

Master's thesis 2018

On SPMSM rotor position estimation from standstill and for low speeds

Evaluation of techniques for estimating position and speed of an SPMSM

VICTOR JOHANSSON

CHALMERS
UNIVERSITY OF TECHNOLOGY

Department of Electrical Engineering
Division of Electric Power Engineering
Chalmers University of Technology
Gothenburg, Sweden 2018

On SPMSM rotor position estimation from standstill and for low speeds
Evaluation of techniques for estimating position and speed of an SPMSM
VICTOR JOHANSSON

Supervisor: Anders Erestam, Husqvarna AB
Examiner: Stefan Lundberg, Electrical Engineering

Master's Thesis 2018
Department of Electrical Engineering
Division of Electric Power Engineering
Chalmers University of Technology
SE-412 96 Gothenburg
Telephone +46 31 772 1000

Cover:

Typeset in LaTeX
Printed by the Department of Electrical Engineering
Gothenburg, Sweden 2018

On SPMSM rotor position estimation from standstill and for low speeds
Evaluation of techniques for estimating position and speed of an SPMSM
VICTOR JOHANSSON
Department of Electrical Engineering
Chalmers University of Technology

Abstract

Knowing the rotor position is essential for performing field-oriented control of permanent magnet synchronous machines. Sometimes, sensorless strategies are employed instead of using sensors in order to estimate the rotor position. This may become troublesome for surface-mounted permanent magnet synchronous machines (SPMSM) since the usual methods rely on saliency properties. In this project, two different methods for estimating the rotor position from standstill through low speeds have been evaluated for an SPMSM for a drill application on behalf of Husqvarna AB. An extended machine model taking saturation and cross-coupling effects into account was developed and several simulations of the discrete-time control system using the position estimation schemes were conducted. A signal injection technique was compared with the statically compensated voltage model (SCVM) due to difficulties in incorporating more suitable choices and also due to time constraints. A simple magnetic pole identification method was implemented and tested in simulations since the estimated angle might have an error of 180 degrees. The results indicate that the rotor position may be estimated from standstill using the signal injection method and that saturation-induced current differences may be used to find the alignment of the magnetic field, thus eliminating the 180 degrees error offset. Further, the results also indicate that the machine can become unstable for sudden load changes but may be stable for slower load changes with the current parameters when using the signal injection technique. The high frequency signal injection scheme was able to estimate the rotor position with a higher steady-state accuracy during high starting loads than the SCVM which could be useful for drill applications. This since it may develop higher starting torque than the SCVM. Usually, SPMSMs exhibit low saliency which make the usual signal injection techniques difficult to use. Therefore, one suggestion is to try to implement and test a low frequency signal injection scheme instead. Therefore, more measurements and simulations should be made before trying to implement these strategies in reality.

Keywords: sensorless, position, estimation, surface-mounted, permanent, magnet, machines, SPMSM.

Acknowledgements

There are some people I would like to thank for helping me with this project in different ways. First, I wish to thank my supervisor, Anders Erestam, who helped me with measurements, planning and who guided me. I would also wish to thank Stefan Lundberg for tips regarding modelling and measurements.

Regarding the measurements and the measurement setups, I also wish to thank Robert Johansson, Peter Vallentin and Jonas Hultin at Husqvarna for their good support and thoughts.

Further, I wish to thank Robert Johansson for the nice discussions and help regarding the machines and the control of them. Without the automated measurement programs Robert wrote, this project would have been a lot more difficult than it already was. Also, I would like to thank Glenn Torsténi at Husqvarna for making some early FEM simulations which gave insights of how the inductance of the machine looked like and how the machine worked, and also Magnus Rosén at Husqvarna for insights regarding measurements and the hardware used. I would also like to thank Håkan Pinzani and Ulf Petersson at Husqvarna for helping me with the estimation of the total moment of inertia of the simulated system.

Also, I would like to thank Johan Berg at Husqvarna for guiding me in the beginning and Peiyuan Chen at Chalmers for helping me with bandwidth selection of the speed controller and the position tracking controller. Lastly, I got some early tips regarding advanced control theory topics from Andreas Andersson at Chalmers, I thank you too.

Victor Johansson, Gothenburg, January 2018

Contents

List of Figures

List of Tables

1
Introduction

The problem of identifying the rotor position in a surface-mounted permanent magnet synchronous machine (SPMSM) for a concrete drill at standstill and for low speeds is investigated in this thesis. The following chapter discusses the background of the project, the aim and scope as well as the chosen scientific method, and related ethical and environmental issues.

1.1 Background

At Husqvarna AB different tools such as concrete drills are developed which can be used at e.g. construction sites. Recently, the trend has gone from using combustion engines to using electric machines for these applications. Compared to combustion engines, electrical machines generally have high efficiency and emit no greenhouse gases which makes them a compelling choice. When used, e.g. on a construction site, the electric machine does not need expensive fuel compared to the combustion motor. This is advantageous since it would reduce the cost of using the equipment the machine is driving. Further, it is less noisy than the combustion engine. However, a possible disadvantage is that it has to be operated relatively close to a power source.

In order to increase the efficiency of the electric drive system used in their products, permanent-magnet synchronous machines (PMSM) have been incorporated into the designs, replacing the older universal motors which generally have low efficiency and uses brushes which need maintenance [1]. PMSMs are brushless and can be operated with high efficiency [2]. Furthermore, PMSMs can be made relatively small [3] and have a high power density [2].

When operating a PMSM, field-oriented control is sometimes used as a control method. This control scheme requires knowledge of the rotor position in order to work. If the rotor position is not accurately determined, the machine might not be able to start [4, p.87]. The rotor position can either be measured, using e.g. an encoder, or it can be estimated. Encoderless (sensorless) control has become an interesting choice since it has some advantages compared to using position sensors, e.g. it makes the system more robust since there are less parts that may malfunction, and the system cost decreases [5]. These sensorless methods rely on estimation of the rotor angle. For nominal speeds, the rotor position can be estimated from the induced back-emf which is found when measuring the terminal voltage and the current drawn by the machine. This method performs well at higher speeds since the back-emf is dominating. At standstill and low speeds, the back-emf becomes too low to measure (zero at standstill) and can not be used for estimating the rotor position

[5]. For salient machines, this problem can be avoided by e.g. using signal injection techniques for low speeds and standstill, as an example [6], but since these depend on saliency, this approach may become troublesome for surface-mounted permanent magnet machines [5].

Husqvarna wants to utilize the benefits of using PMSMs in electric applications and in that way make e.g. more energy efficient products. The machine used is a nonsalient surface-mounted PMSM. When using an SPMSM in a concrete drill application, it was noticed that, with the current angle estimation scheme, the machine could have problems when starting inside a drilled hole. When trying to restart the drill in the hole, the drill started to shake. It was believed that this had to do with the control and possibly lack of a good rotor angle estimate.

1.2 Aim

The aim of this thesis is to come up with a way to estimate the rotor position of a non-salient SPMSM in a concrete drill application and to utilize that in a control system that should be able to start the drill from standstill.

1.3 Scope

The task is to find ways to estimate the rotor position and to control a non-salient PMSM in a concrete drill application during start-up and low speeds. Since this project concerns start-up control, optimizing control and position estimation at nominal speed as well as turn-off procedures are not going to be looked into. When conducting the literature survey, only methods that are applicable to a non-salient SPMSM will be considered in this project. Also, methods which have a risk for rotation in the wrong direction will be discarded, unless they can be modified somehow, otherwise it could harm workers or possibly disconnect the drill. Environmental and ethical aspects will be taken into account as much as possible in order to promote sustainable development and reduce the risks of causing harm to others. Regarding modelling of the SPMSM for simulations of the estimation strategies, the flux harmonics will be neglected and only a fundamental component model of the machine will be developed.

Further, it would be interesting to see if several position estimation methods could be implemented for different speed ranges respectively. However, this could become too complex and the speed or speed range for which the transition between two methods has to be made might be time consuming and difficult to determine. Therefore, these questions are not considered as mandatory and will only be considered if time allows it. If there would be any indication that this way of using several methods would be beneficial, it could be described as a possible part of future work instead.

1.4 Method

There are two main steps in this project. Firstly, a literature review has been conducted in order to gain enough knowledge to succeed with this project. In order to use a sensorless control method from standstill for practical implementations, ways of estimating the rotor position and to make a distinction between the north and the south pole have been found in the literature and are discussed in the literature review. Secondly, the model of the motor and the estimation procedures have been simulated and verified for different test cases. The project was thus entirely theoretical in terms of no practical implementations, only literature review and simulations. In the following parts of this section, a further description of this is given.

The simulations of the motor has firstly been made through "continuous-time" simulations in MATLAB/Simulink using perfect sinusoidal inputs to get acquainted with the system and the PMSM model used. These "continuous time" simulations (hereafter called "continuous simulations") used a continuous-time version of the controllers and estimators. The model of the motor has been ensured to work before implementing the position estimation methods. Therefore, a comparison between the simulated motor and measurements on the real setup has been made for certain test cases to see if the simulated machine behaves as it should. When the model was deemed to be good enough, continuous simulations of the position estimation strategies were made. This was done to ensure that the estimation strategy worked nicely before discretization. Discrete-time simulations were done in order to yield more realistic results. Therefore, discretization of the test setup (controllers and estimators) had to be done. Also, for the discrete-time simulations, an inverter using pulse-width modulation has been implemented resulting in more realistic simulation results.

For the evaluation of the performance of the chosen method, the method was compared with a sensorless scheme based on the voltage model (the statically compensated voltage model, SCVM) [7]. This in order to show whether or not the proposed strategy is better for low speeds than the usual back-emf based scheme.

The standstill evaluation was based on estimation of different initial rotor positions. The startup simulations tested the ability to start with different loads. For all cases, friction load torque was applied. High static friction loads is thought to mimic the situations when the drill gets stuck. Therefore, different static friction loads were applied during the startup tests.

1.5 Ethical and Environmental Aspects

This thesis may aid the development of a working implementation of sensorless control for SPMSMs from standstill through low speeds for concrete drills. An increase in the use of electric drive systems could help decreasing the use of fossil drives in the products, thus reducing the environmental impact of using these products. Sustainable development is not entirely about reducing the environmental impact for products. In fact, sustainable development can be thought of encapsulating ecological, economical and social aspects [8]. In the following paragraphs, aspects on the

project related to sustainable development will be mentioned and discussed. Also, ethical issues regarding the project will be addressed.

The ideas and methods provided to the company through this thesis might be used in order to develop products. Therefore, if the results indicate that a certain method is safe to use and the method proves to be unsafe when it has been implemented in a product there could be several ethical consequences. As an example, the electric drill, for which the PMSM is used, is not currently handheld. However, the control methods and rotor position estimation strategies used in this project might be used for handheld devices. As have been stated before, there is a risk for reverse rotation if the rotor position is not accurately determined. If the motor starts to rotate with high torque and high speed in the wrong direction, the worker holding the drill might get injured. Therefore, the methods has to be safe to use. Also, the control methods should cope with certain situations such as higher loading from sudden movements caused by the worker and so on. This means that the drive system of the drill should not become unstable during normal working conditions. In order to test the methods, load disturbances could be implemented in the simulations.

Also, the methods should not increase the risk for damaging the equipment using the controlled PMSM, e.g. vibrations from signal injection might cause mechanical stress and injection of high frequency signals might cause increased losses and higher temperature which in turn could damage the PMSM. These aspects have to be considered for a real implementation.

It is important that the results, whether they are considered good or bad, are fully presented. The conclusions should be based entirely on the results from the tests conducted in this project no matter what the results may indicate. Also, it can not be expected that scientists who have written the articles, on which the methods tested are based, have the same view regarding disclosing results and actually presenting conclusions based on the results. There might be scientists who wants to give the impression that the results of their research is better than it appears to be. Therefore, the scientific articles reviewed and used in this project should be critically evaluated before choosing possible methods. If some methods have been chosen, it is also important to state possible limitations for these methods since it may impact the final result of the project. Also, instead of trying lots of methods, it is better to try few thoroughly in order to avoid bad results.

As already have been mentioned, the results of this project might have an impact on the use of electric drives in the products for the company. Hence, this could have environmental impacts such as using motors with less emissions and higher efficiency. However, the use of these electric machines have other negative impacts. For example, if the motor parameters are wrongly estimated, the motor control might set higher references meaning that it will draw more power than necessary. There are also issues regarding the motor type. PMSM uses permanent magnets to form a magnetic field and these magnets can be made from different materials, e.g. they can be based on iron or rare-earth metals [9]. The rare-earth metals on the market originates usually from China and the mining and refinement of these metals has caused serious environmental and health issues as well as political and economical issues over the years [10]. As an example, in Baotou, China, radioactive material

has accumulated in a dam during the process of refining rare-earth material which has caused a higher risk for cancer for the people living nearby [10]. Also, since the supply of rare-earth metals depends on the export regulations in China, the price and availability of the material might become a problem [10]. Hence, if the PMSM in this project uses permanent magnets based on rare-earth materials, it might be better to use another type of electric motor which is not dependent on the supply of permanent magnets made from rare-earth metals.

2
Concrete Drill System

This chapter starts with a description of the concrete drill system. Then the machine model is developed. At the end, the modelling of the inverter used to supply the machine is discussed.

2.1 System Overview

In Figure 2.1 a schematic image of the drill setup can be seen The drill is connected through a cable to the power supply which contains power electronics that are used to control the drill. The power supply is connected to the grid, either through a three-phase connection or through a single-phase connection. The drill drives a "drill bit" which in this case is a hollow cylinder with an open end towards the concrete. This is basically a cylindrical concrete saw rather than a "drill". However, it will be called a "drill" in the rest of the thesis for simplicity.

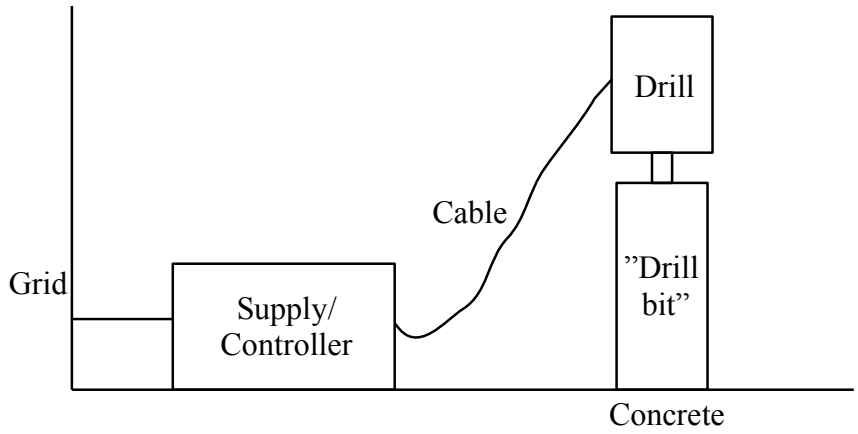

Figure 2.1: Overview of the drill system.

Figure 2.2 shows the details of the equipment in Figure 2.1. The power supply is connected to the grid and contains a rectifier, a boost DC/DC converter, an inverter and controllers. The power supply can be connected to a grid with ratings, for both a 3-phase connection and a single-phase connection, within the interval shown in the figure. The rectified grid voltage can be boosted up to 750 V which is used to supply the machine through the inverter. The controller gets measured signals, such as the DC-bus voltage U_{DC} and the three-phase currents i_{abc}, in order to regulate the speed and the current of the machine (SPMSM) properly, and the controller

outputs a reference voltage which is realized by the PWM-controlled switches of the inverter. The drill machine is connected to the power supply through a cable. Further, the machine used has a nominal speed of 6000 rpm and can output about 6 kW of power. The nominal torque of the machine is about 10 Nm and the cylindrical drill bit is connected on the axis of the machine through gears.

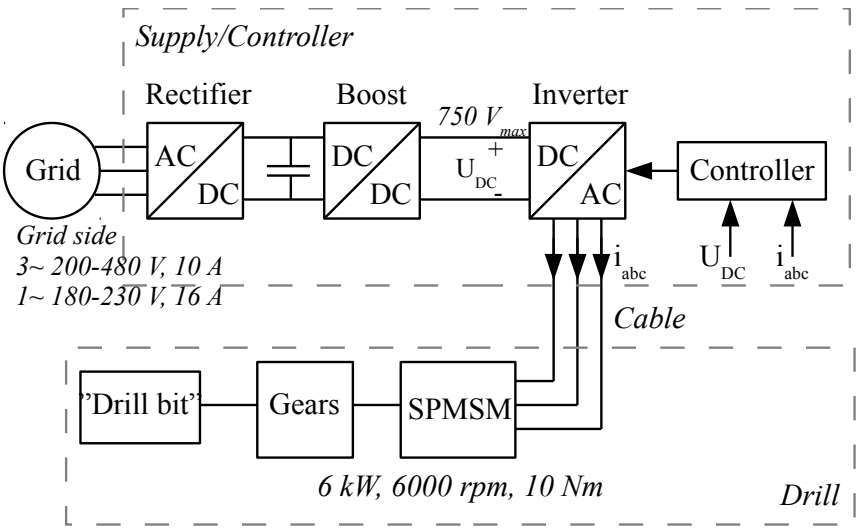

Figure 2.2: Details of the drill system.

Not having a position sensor and thus making the control system "sensorless" is preferable due to several reasons, e.g. without an extra sensor there is less risk for measurement failure and the cost of the system is reduced [5]. It would be better if the position could be estimated using the signals that are already measured and used in the control system, e.g. the currents. Finding a way to do so is what this thesis is all about.

The drilling procedure is described in the following text. The drill is mounted on a stand and is lowered down to the concrete by the user using a handle. The hollow cylinder cuts through the concrete and leaves a cut shaped as the edge of a circle. On the edge of the drill, there are diamonds mounted. The diamonds grinds the concrete as the drill rotates. If the machine is loaded too much it could stop. When the machine is restarted within the hole it may not start properly and can shake. It is believed this is because the rotor angle is not estimated good enough or the machine is too highly loaded. In order to start again, the drill may have to be raised above the hole and then be restarted. As stated earlier, this project's aim is to find a way to identify the rotor position from standstill which could make it possible to start without having to raise the drill from the hole.

2.2 Permanent Magnet Synchronous Machine

One of various PMSM types is the surface-mounted permanent magnet machine (SPMSM). For SPMSMs, the magnets are mounted on the surface of the rotor

making the rotor almost magnetically "round" since the permeability of the magnets is close to the permeability of air [11]. In order to simulate the SPMSM, this chapter considers machine modelling and starts with discussing coordinate system transformations needed for that purpose.

2.2.1 Coordinate System Transformations

The machine can be described in different coordinate systems which can be beneficial in some circumstances, e.g. control. The stationary $\alpha\beta$-frame, seen in Figure 2.3, is a two-phase representation of the three-phase system and the α-axis is aligned with phase a. The dq- and $\widehat{dq}$-coordinate systems, also seen in Figure 2.3, are rotational coordinate systems and rotates with the speed ω_r (the rotor speed) and $\widehat{\omega}_r$ (the estimated rotor speed) respectively. In the $\alpha\beta$-frame, the three-phase AC quantities are represented as rotating vectors while in a rotating frame (having the same frequency as the AC signals), these appear as DC quantities. Hence, for a synchronous machine where the rotor rotates synchronously with the applied AC signals in steady-state, it is easier to develop control systems in the dq-frame than in the $\alpha\beta$-frame.

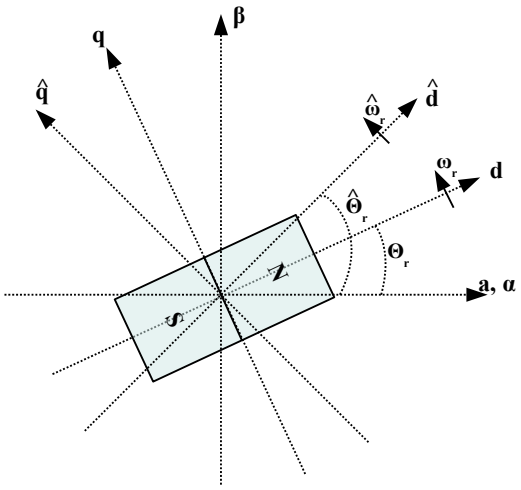

Figure 2.3: Definition of the $\alpha\beta$, dq and $\widehat{dq}$ coordinate systems. Phase a is shown while phases b and c are omitted for a clearer view. The rotor is shown as a rectangular permanent magnet, having a north and a south pole, for simplicity.

The d-axis is aligned to the rotor flux originating from the north pole, as is seen in Figure 2.3. The angular position of the d-axis, and thus the rotor flux, is denoted as θ_r. The estimated speed might not always be equal to the real rotor speed, making the estimated rotor position, $\widehat{\theta}_r$, different compared to θ_r and this could have serious effects for the control system.

The transformation from three-phase quantities to the $\alpha\beta$-frame is done using the Clarke transformation in matrix form (amplitude invariant transformation) as stated in [4]

$$\begin{bmatrix} x_\alpha \\ x_\beta \end{bmatrix} = \begin{bmatrix} \frac{2}{3} & -\frac{1}{3} & -\frac{1}{3} \\ 0 & \frac{1}{\sqrt{3}} & -\frac{1}{\sqrt{3}} \end{bmatrix} \begin{bmatrix} x_a \\ x_b \\ x_c \end{bmatrix} \tag{2.1}$$

The transformation from the $\alpha\beta$-frame to the real dq-frame is done using the following matrix transformation [4]

$$\begin{bmatrix} x_d \\ x_q \end{bmatrix} = \begin{bmatrix} cos(\theta_r) & sin(\theta_r) \\ -sin(\theta_r) & cos(\theta_r) \end{bmatrix} \begin{bmatrix} x_\alpha \\ x_\beta \end{bmatrix} \tag{2.2}$$

where θ_r is found in Figure 2.3 as the real dq-frame position.

If the angle difference between the real dq-frame and the estimated dq-frame is denoted as $\theta_e = \theta_r - \widehat{\theta}_r$, the transformation between the real dq-frame to the estimated dq-frame can be done according to

$$\begin{bmatrix} \widehat{x}_d \\ \widehat{x}_q \end{bmatrix} = \begin{bmatrix} cos(\theta_e) & -sin(\theta_e) \\ sin(\theta_e) & cos(\theta_e) \end{bmatrix} \begin{bmatrix} x_d \\ x_q \end{bmatrix} \tag{2.3}$$

while the transformation from the estimated dq-frame to the real dq-frame can be found to be

$$\begin{bmatrix} x_d \\ x_q \end{bmatrix} = \begin{bmatrix} cos(\theta_e) & sin(\theta_e) \\ -sin(\theta_e) & cos(\theta_e) \end{bmatrix} \begin{bmatrix} \widehat{x}_d \\ \widehat{x}_q \end{bmatrix}. \tag{2.4}$$

2.2.2 Derivation of the PMSM Model

In this section, a fundamental component machine model is going to be derived. This means that the model does not take any harmonics into account, it is only dependent on the fundamental frequency component. A general PMSM circuit can be modelled as the sum of a resistive voltage drop (resistive losses in the windings) and the change in flux linkage over time. This model is described in the following three-phase equation [12]

$$\underline{u}_s^{abc} = R_s \cdot \underline{i}_s^{abc} + \frac{d\underline{\lambda}_s^{abc}}{dt} \tag{2.5}$$

where $\underline{u}_s^{abc}$ is a vector of the three-phase voltages (V), $\underline{i}_s^{abc}$ is a vector containing the three-phase currents (A) while $\underline{\lambda}_s^{abc}$ is the three-phase flux linkage (Wb) and R_s is the stator resistance (Ω). As a part of the total three-phase flux linkage, the rotor permanent magnet flux linkage can be expressed as [12]

$$\underline{\lambda}_{PM}^{abc} = \sum_{n=1,3,5,7,\ldots} \lambda_{PM,n} \begin{bmatrix} cos(n\theta_r) \\ cos\Big(n(\theta_r - \frac{2\pi}{3})\Big) \\ cos\Big(n(\theta_r - \frac{4\pi}{3})\Big) \end{bmatrix} \tag{2.6}$$

where n denotes the harmonic order, $\lambda_{PM,n}$ is the magnitude of the corresponding harmonic. The harmonics are rotor position dependent as seen in (2.6). In the rest

of this thesis, the rotor flux harmonics will be neglected in order to simplify the machine model. In fact, as will be seen later, this approximation is not valid in reality.

The machine equation in (2.5) can further be expressed in the $\alpha\beta$-frame as

$$\underline{u}_s^{\alpha\beta} = R_s \cdot \underline{i}_s^{\alpha\beta} + \frac{d\underline{\lambda}_s^{\alpha\beta}}{dt} \tag{2.7}$$

where $\underline{u}_s^{\alpha\beta}$ and $\underline{i}_s^{\alpha\beta}$ are the $\alpha\beta$-frame stator voltage and current respectively and $\underline{\lambda}_s^{\alpha\beta}$ is the total flux linkage in the $\alpha\beta$-frame. The total flux linkage equals the sum of the flux generated from the windings and the rotor flux (as in e.g. [12] for a three-phase model) Also, the rotor flux is rotating in the $\alpha\beta$-frame with the speed ω_r. Hence, the total flux linkage can be described as $\underline{\lambda}_s^{\alpha\beta} = \underline{\lambda}_{s,w}^{\alpha\beta} + \lambda_{PM} \cdot e^{j\omega_r t}$ where $\underline{\lambda}_{s,w}^{\alpha\beta}$ is the winding flux and λ_{PM} is the rotor flux linkage magnitude (Wb) which is assumed to be constant. Therefore, (2.7) can be further described as

$$\underline{u}_s^{\alpha\beta} = R_s \cdot \underline{i}_s^{\alpha\beta} + \frac{d\underline{\lambda}_{s,w}^{\alpha\beta}}{dt} + j\omega_r \lambda_{PM} e^{j\omega_r t}. \tag{2.8}$$

Using the transformation from the $\alpha\beta$-frame to the dq-frame derived in Section 2.2.1 having the exact rotor position as the transformation angle, the dq-model of the machine can be described as

$$\underline{u}_s^{dq} = R_s \cdot \underline{i}_s^{dq} + \frac{d\underline{\lambda}_{s,w}^{dq}}{dt} + j\omega_r \cdot (\underline{\lambda}_{s,w}^{dq} + \lambda_{PM}) \tag{2.9}$$

where $\underline{u}_{dq}$ and $\underline{i}_{dq}$ are the stator voltage and current respectively, and $\underline{\lambda}_{s,w}^{dq}$ is the stator winding flux linkage. Also, since the permanent magnet flux is constant in the real dq-frame, as seen in (2.9), the flux derivative can be rewritten as the change of the total flux in time since the rotor flux derivative is zero. This gives the final general dq-frame machine equation as (found in e.g. [13])

$$\underline{u}_s^{dq} = R_s \cdot \underline{i}_s^{dq} + \frac{d\underline{\lambda}_s^{dq}}{dt} + j\omega_r \cdot \underline{\lambda}_s^{dq} \tag{2.10}$$

where $\underline{\lambda}_s^{dq} = \underline{\lambda}_{s,w}^{dq} + \lambda_{PM}$. In [13], the flux in the dq-frame is written as a function of the dq-current. Also in [12], the total three-phase flux linkage is assumed to be a function of the current and the rotor position. In this case (and assuming this still holds in the dq-frame), that would translate into $\underline{\lambda}_s^{dq} = \underline{\lambda}_s^{dq}(\underline{i}_s^{dq}, \theta_r)$, then the time derivative of the total dq-flux is a sum of the partial derivatives as

$$\frac{d\underline{\lambda}_s^{dq}}{dt} = \frac{\partial \underline{\lambda}_s^{dq}}{\partial \underline{i}_s^{dq}}\Big|_{\theta_r = const} \cdot \frac{d\underline{i}_s^{dq}}{dt} + \frac{\partial \underline{\lambda}_s^{dq}}{\partial \theta_r}\Big|_{\underline{i}_s^{dq} = const} \cdot \frac{d\theta_r}{dt} = \frac{\partial \underline{\lambda}_s^{dq}}{\partial \underline{i}_s^{dq}} \cdot \frac{d\underline{i}_s^{dq}}{dt} + \frac{\partial \underline{\lambda}_s^{dq}}{\partial \theta_r} \cdot \frac{d\theta_r}{dt} \tag{2.11}$$

where the partial derivatives of the total flux are developed and $\frac{d\theta_r}{dt} = \omega_r$ (rad/s). Hence, the full machine model written in (2.10) in the dq-frame is developed using (2.11) as

$$\underline{u}_s^{dq} = R_s \cdot \underline{i}_s^{dq} + \frac{\partial \underline{\lambda}_s^{dq}}{\partial \underline{i}_s^{dq}} \cdot \frac{d\underline{i}_s^{dq}}{dt} + \omega_r (j\underline{\lambda}_s^{dq} + \frac{\partial \underline{\lambda}_s^{dq}}{\partial \theta_r}). \tag{2.12}$$

For simplicity, the flux harmonics will be neglected in the rest of this report and the partial derivative of the flux with respect to rotor position will be assumed to be zero. This will lead to a less accurate model and the results of the thesis might not resemble the actual performance of the chosen position estimators in a real drive system. With this in mind, the machine model used in this project is

$$\underline{u}_s^{dq} = R_s \cdot \underline{i}_s^{dq} + \frac{\partial \underline{\lambda}_s^{dq}}{\partial \underline{i}_s^{dq}} \cdot \frac{d\underline{i}_s^{dq}}{dt} + j\omega_r \underline{\lambda}_s^{dq}. \tag{2.13}$$

The term $\frac{\partial \underline{\lambda}_s^{dq}}{\partial \underline{i}_s^{dq}}$ has been found to have several different names in the literature but here it is called the incremental inductance (H) [13] and can be expressed as a matrix of partial derivatives

$$\frac{\partial \underline{\lambda}_s^{dq}}{\partial \underline{i}_s^{dq}} = \begin{bmatrix} \frac{\partial \lambda_{d,s}}{\partial i_{d,s}} & \frac{\partial \lambda_{d,s}}{\partial i_{q,s}} \\ \frac{\partial \lambda_{q,s}}{\partial i_{d,s}} & \frac{\partial \lambda_{q,s}}{\partial i_{q,s}} \end{bmatrix}. \tag{2.14}$$

The elements $\frac{\partial \lambda_{d,s}}{\partial i_{q,s}}$ and $\frac{\partial \lambda_{q,s}}{\partial i_{d,s}}$ in (2.14) are termed cross-coupling terms and if there is a change in the current components, these cross-coupling terms will induce a change in the other axis' voltage (e.g. a change in q-current will affect the d-voltage).

According to the literature, e.g. for dq [13] or for three-phase [12], the total flux can further be described as $\underline{\lambda}_s^{dq} = \underline{L} \cdot \underline{i}_s^{dq} + \lambda_{PM}$ where $\underline{L}$ is called the apparent inductance (H) [13] (or absolute inductance as in [12]) and is written in dq as

$$\underline{L} = \begin{bmatrix} L_d & L_{dq} \\ L_{qd} & L_q \end{bmatrix}. \tag{2.15}$$

The absolute inductances are functions of e.g. the current, as seen for the three-phase model in [12] and for the dq-frame model in [13]. The cross-coupling terms, L_{dq} and L_{qd}, are neglected for simplicity and are said to be accounted for in L_d and L_q according to [13]. Hence, these inductances are not really pure d- and q-inductances. The parameter identification will be discussed further in Section 4.1, where the absolute and incremental inductances are calculated for different current combinations to account for saturation effects.

Also, the machine model is not complete without the mechanical model. The two main mechanical equations used are

$$J\frac{d\Omega_r}{dt} = \left[\Omega_r = \frac{\omega_r}{n_p}\right] = \frac{J}{n_p}\frac{d\omega_r}{dt} = T_e - T_L \tag{2.16}$$

$$\omega_r = \frac{d\theta_r}{dt} \tag{2.17}$$

where Ω_r and ω_r are the mechanical and the electrical rotor speed (rad/s) respectively, and n_p is the number of pole pairs of the machine. J is the moment of inertia of the rotating parts. In this project, the moment of inertia was estimated from measurements. It was assumed that the largest contributors to the total moment of inertia of the concrete drill were the rotor itself, the clutch, and the drill bit. The rotor inertia was given from FEM simulations while the clutch inertia and the drill

bit inertia had to be estimated. The moment of inertia of the gear box was omitted and this results in an error in reality. The drill bit is modelled as a hollow cylinder with thin walls, $J = mr^2$. The clutch is modelled as a solid cylinder, $J = \frac{1}{2}mr^2$. The masses and radii for these two components were measured and the respective moments of inertia of the three components were added together to form the resulting moment of inertia of the system. Further, since the drill bit is placed on the low speed side of the gear box, its moment of inertia had to be recalculated to the high speed side of the gear box (the same side the clutch and the rotor is) using

$$J_{high} = \frac{J_{low}}{k^2} \tag{2.18}$$

where J_{high} is the equivalent moment of inertia on the high speed side, J_{low} is the moment of inertia on the low speed side, and k is the gear box ratio (high speed versus low speed).

For now, the load torque, T_L (Nm), is kept as a general term while the electrical torque produced by the machine, T_e (Nm), is expressed as

$$T_e = \frac{3n_p}{2}[\lambda_{PM} \cdot i_{q,s} + (L_d - L_q) \cdot i_{d,s} \cdot i_{q,s}]. \tag{2.19}$$

For nonsalient machines (such as SPMSM), the torque will only depend on the first term in (2.19) since $L_d = L_q$ but to keep generality the full expression is to be used in the report.

The load torque in this project comprises only friction load torque and an extra load constant which could be used for load steps in the simulations. The simulation cases will test the ability to start the drill when it is standing still inside a drilled hole and it is assumed that mainly friction torque is acting on the drill during such a situation. As stated previously, as the drill grinds the concrete, dust and iron parts may get stuck between the drill and the concrete if not completely removed. As more dust accumulates, the friction increases and the drill may get stuck. The friction load torque is a nonlinear function depending on the speed and developed electrical torque. When the machine is stationary and have not yet developed enough electrical torque, the machine experiences a static friction load. In the simulations, this will only act as a barrier for the startup, i.e. if the machine has not developed more than the equivalent static friction load torque when still stationary, the machine will remain stationary. When the electrical torque has reached above this limit and starts to rotate, the friction load torque is constant and a bit lower (kinetic friction). As a conclusion, the following is the equation for the load torque

$$T_L = \begin{cases} T_e & \text{if standstill and } |T_e| \leq C \\ \mu_k mgr \cdot sign(\omega_r)/k + T_{L,ext} & \text{else} \end{cases} \tag{2.20}$$

where C is the static friction torque transformed to the high speed side of the gear box and initially is put to $C = \mu_s mgr/k$ but will be swept in upcoming simulations, μ_s is the static friction coefficient, μ_k is the kinetic friction coefficient, $g = 9.81 m/s^2$ is the gravitational constant, m is the mass of the drill, r is the radius of the drill bit, and $T_{L,ext}$ is the constant extra load torque. The static friction load torque is

acting as a limit for starting. Later on, this static friction is to be swept and can be considered just a constant C. The load torque equals the machine torque when the machine has not overcome the static friction in order to logically describe the zero acceleration with (2.16). The reason why the static friction torque is put to $\mu_s mgr/k$ in the beginning is just to have an easily explained starting point, i.e. having it put to some random number would have been hard to explain since no load data for a normal start was available. Therefore, as a starting point, it is put to the static friction between concrete and steel transformed to the high speed side of the gear box. Further, the load torque is assumed to be acting on the edge of the cylindrical drill bit since it is modelled as a hollow cylinder with thin walls. In reality, the dust may accumulate between the drill walls and the concrete and thus a friction force on the sides of the drill might exist. This force is not modelled, but in upcoming simulations the static friction torque is to be swept and it is assumed that this phenomenon is included into that value (C) then. The kinetic friction load torque acts as the friction load when the rotor rotates and is written as $sign(\omega_r)\mu_k mgr/k$ where μ_k is the kinetic friction coefficient. The static as well as the kinetic friction coefficients needs to be measured for a certain application. However, in order to simplify the project, the static friction coefficient was based on the results of [14] and was chosen as $\mu_s = 0.6$. This friction coefficient is based on steel on concrete, which is not true for this application since it should be the friction coefficients between diamonds and concrete. However, this was not found during the literature review. The kinetic friction coefficient is said to usually be less than the static one [15], but since no value was found for this it had to be assumed and it was chosen to be $\mu_k = 0.5$. The choice of these parameters might affect the outcome of the simulations but it is seen as a minor issue for this project.

Furthermore, the model can be expressed as a nonlinear state-space model which can be implemented in computer software for simulations. The nonlinear state-space model of the machine is derived using (2.13) and can be found in Appendix A together with the full derivation.

2.3 Motor Converter

The machine is supplied with power from the grid through various power electronic stages, seen in e.g. Figure 2.2. The power electronic stage between the grid and the machine is to be modelled here. In order to simplify, the rectifier and the boost converter are not going to be modelled. Instead, the DC-voltage on the output of the boost converter is modelled as a constant DC-bus voltage, U_{DC}. Hence, the only power electronic part that is modelled in this project is the inverter. The schematic over the inverter is seen in Figure 2.4.

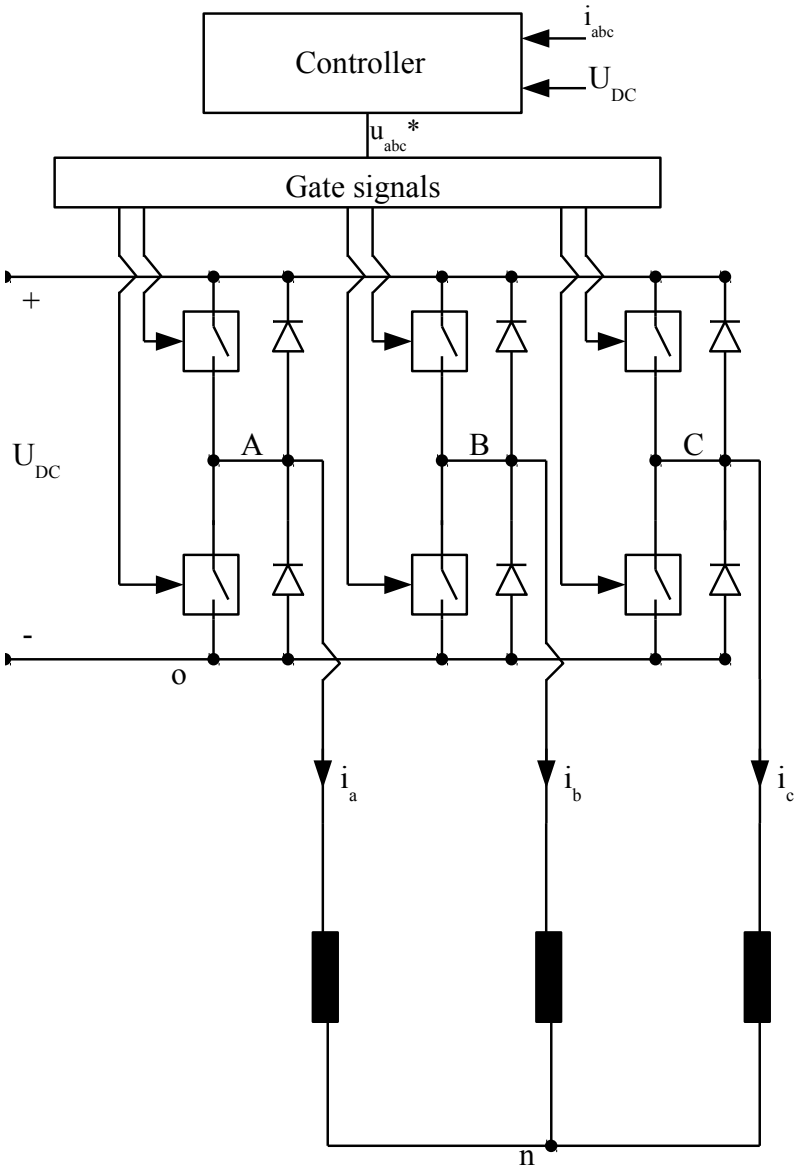

Figure 2.4: The converter supplying the machine.

The three-phase inverter is built up of six switches and six diodes. The switches and diodes are assumed to be ideal. The switches are modelled as being either conducting or not conducting. Further, the gate circuit is not modelled. Instead, gate signals are generated which states whether or not the switches are conducting. The pulse-width modulation (PWM) switching strategy used is based on the symmetrical suboscillation method described in [4]. This method relies upon injection of zero-sequence voltages to increase the voltage magnitude within the linear modulation range [4]. The basics of how to achieve the correct mean output voltage with this method is to be derived next.

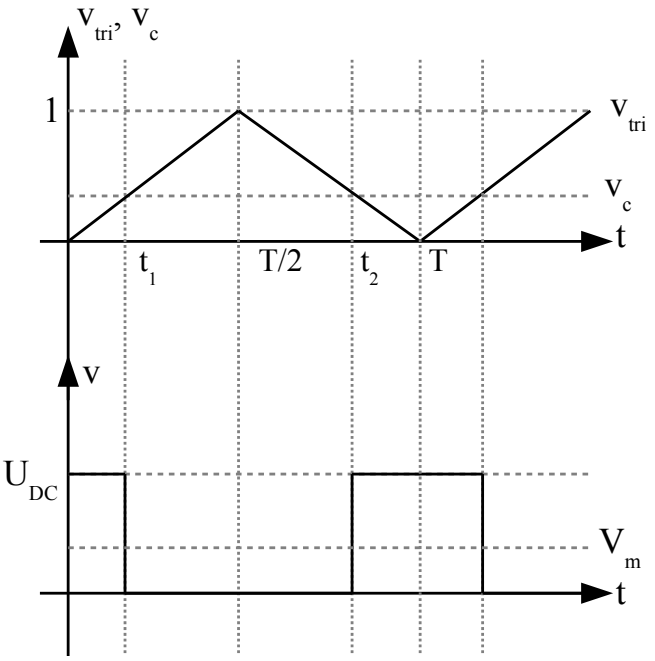

Figure 2.5: The figure shows the development of the output voltage for one switching period.

The suboscillation method relies upon a comparison between a reference signal and a triangular carrier wave [4]. It is assumed that the carrier wave has a much higher frequency than the reference signal, such that, in a switching period, the reference signal seems to be constant. Also, in the following, the letter x refers to any of the phases A, B or C in Figure 2.4, and capital V refers to mean voltage while v refers to instantaneous voltage.

Both the carrier wave and the reference signal are visualized in Figure 2.5, where v_{tri} is the carrier wave, $v_c = v_x^*$ is the normalized reference voltage signal of phase x, U_{DC} is the DC-bus voltage (see Figure 2.4), $v = v_{xo}$ is the resulting output voltage of phase x with respect to point o (see Figure 2.4), and V_m is the mean output voltage. It can be seen that the carrier signal and the reference signal are normalized. Also, in Figure 2.5, only one phase reference signal is seen. In reality, the three-phase reference signals are compared to the triangular wave but it is easier to visualize it this way.

Whenever v_c is greater than v_{tri}, the upper switch in the phase leg (see Figure 2.4) is on and the resulting output voltage becomes $v = U_{DC}$ as seen in Figure 2.5. When v_c is lower than v_{tri}, the output voltage becomes $v = 0$ as the lower switch is on and the upper one is off. At t_1, v_c equals v_{tri} and the upper switch turns off and the lower switch is turned on. The triangular wave can be described as $v_{tri} = \frac{2t}{T}$ within the interval $0 < t < T/2$. Hence, $t_1 = \frac{T}{2}v_c$. Remember, v_c is unitless ($v_c = v_x^*/U_{DC}$). At t_2, $v_c = v_{tri}$ again but the lower switch turns off and the upper switch is on. During $T/2 < t < T$, $v_{tri} = 1 - \frac{2t}{T}$ and this gives $t_2 = \frac{T}{2}(1 - v_c)$. With this, the mean output voltage between points x (any phase) and o can be written as

$$\begin{aligned} V_m =& V_{xo} = \frac{1}{T}\int_0^T v dt = \frac{1}{T}\Big[\int_0^{t_1} U_{DC} dt + \int_{t_1}^{t_2} 0 dt + \int_{t_2}^{T} U_{DC} dt\Big] = \\ =& U_{DC}(v_c + \frac{1}{2}). \end{aligned} \tag{2.21}$$

The real load output voltage (i.e. phase voltage between point x and n) need to be calculated in relation to the neutral point of the machine, as for now the output voltage is in relation to point o. The resulting output load phase voltage is [16]

$$v_{xn} = v_{xo} - v_{no} \tag{2.22}$$

where $v_{no} = \frac{v_{Ao}+v_{Bo}+v_{Co}}{3}$ [16]. As was shown in (2.21), the mean output voltage for any phase is $V_{xo} = \frac{1}{T}\int_0^T v_{xo} dt = U_{DC}(v_c + \frac{1}{2})$. Hence, the mean voltage between the neutral point n and point o can be written as (assuming balanced three-phase voltages)

$$V_{no} = \frac{1}{3}(V_{Ao} + V_{Bo} + V_{Co}) = \frac{1}{3}(v_A^* + v_B^* + v_C^* + \frac{3}{2}U_{DC}) = \frac{U_{DC}}{2}. \tag{2.23}$$

The mean output load voltage is thus $V_{xn} = V_{xo} - V_{no} = U_{DC}(v_c + \frac{1}{2}) - \frac{U_{DC}}{2} = U_{DC}v_c = [v_c = v_x^*/U_{DC}] = v_x^*$. This means that the mean output load voltage of phase x equals the reference voltage of the same phase when using this switching scheme.

So, this suboscillation scheme is realized in Simulink in the following way. The reference signal for each phase, v_c, is calculated and compared with a triangular carrier wave as discussed earlier. This is done as part of the "Gate signals"-block in Figure 2.4. If the reference signal is greater than the carrier wave, the output will equal 1, otherwise the output equals 0. This output is then multiplied with the DC-bus voltage to form v, as seen in Figure 2.5, to mimic the behaviour of the switching in the inverter, seen in Figure 2.4, for each phase. The load voltage is determined from (2.22) and then fed to the machine model. In order to increase the modulation range, the symmetric suboscillation method [4] has been implemented where a zero-sequence voltage has been subtracted from the reference voltage before the comparison with the triangular wave.

3

Review of Rotor Position Estimation Methods

As has been stated in the introduction, the rotor position is needed in order to start the motor successfully. The following sections are covering some basic rotor position estimation methods found in the literature in order to give a better background to the methods chosen later on. The sections cover basic machine-model based methods (back-emf and flux estimation) as well as more elaborate methods relying upon magnetic properties and touches upon other topics as well such as observer-based strategies. Further, there might be other topics not covered as well but the procedures mentioned were among the most commonly found in the literature reviewing process.

3.1 Back-Emf Based and Flux Based Methods

When the rotor rotates, the permanent magnet flux will pass the stator windings and will induce a back electromotive force (back-emf) in these windings. The back-emf is dependent on the rotor position and if the back-emf can be obtained, the rotor position could be estimated. For higher speeds, the induced back-emf in the stator windings of the machine is dominating. This can be seen when examining the machine equation in (2.7) and (2.8). The back-emf can be described as $j\omega_r \cdot \lambda_{PM} \cdot e^{j\theta_r}$ which is proportional to the speed of the rotor and contains information of the rotor position.

The back-emf term can e.g. be expressed as a complex vector in the rotating dq-frame seen in Figure 2.3. The components of the complex back-emf dq-vector can be used to estimate the rotor position and speed [4]. Furthermore, since the back-emf is proportional to the rotor speed, the estimation process fails at low speeds and standstill conditions. A large initial error angle could also make the rotor spin in the wrong direction if started [7]. Thus, back-emf methods are generally not applicable for position estimation from standstill.

The back-emf method presented in [17] is extended such that it can operate for lower speeds. The current controller output voltage contains information of the rotor position error through the back-emf and can be used as input to a PI controller which regulates the error to zero [17]. By dividing the d-axis current controller output (i.e. the d-axis reference voltage) with the estimated speed and the rotor flux magnitude, the rotor position can be tracked. However, the method has to be modified during low speeds [17].

According to [4] and [5], the flux, and hence the rotor position, can be found by simply integrating the back-emf term and this is called the "voltage model". The integration may be modified as a lowpass filter instead to maintain stability and a method known as the "statically compensated voltage model" (SCVM) can thus be derived [4].

In [18], the rotor flux is estimated in the $\alpha\beta$-frame with a rotor flux observer. Using the rotor flux, the needed transformations are done without knowing the exact rotor position [18] using that the ratio between the rotor flux in the $\alpha\beta$-frame and the absolute value of the same equals $e^{j\theta_r}$. Compensations and d-axis current injection is done in order to maintain and enhance control at zero speed and low speeds [18].

3.2 Signal Injection Methods

For machines which have a geometrically salient structure or, especially for surface-mounted PMSMs, have a saturation-induced saliency, the rotor position can be estimated from the current response of an injected voltage. The following sections describes the most common signal injection techniques found. The methods reviewed are high frequency rotating voltage injection, high frequency pulsating voltage injection as well as high frequency square-wave injection.

3.2.1 Rotating Voltage Injection

Rotating voltage vector injection is one of the methods used in the literature. The principle is that the current due to the injected voltage is affected by the different inductance in the dq-axes, and this is used to retrieve the rotor position, see e.g. [19]. This inductance difference (or saliencies) can be due to either geometric reasons or due to saturation [12]. Assume that a voltage vector is injected in the $\alpha\beta$-frame, $\underline{u}_i^{\alpha\beta} = V_i \cdot e^{j\omega_i t}$, as seen in Figure 3.1, with the frequency ω_i and magnitude V_i.

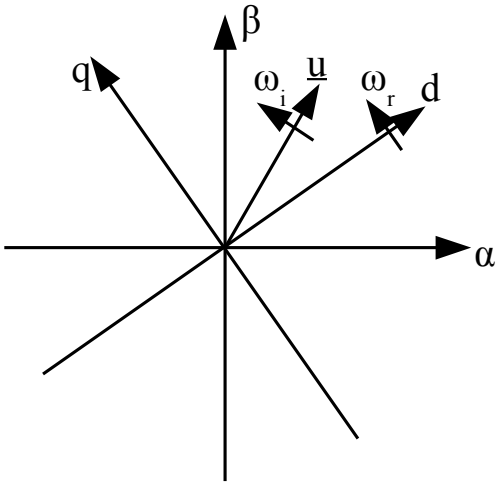

Figure 3.1: The rotating voltage vector in the $\alpha\beta$-frame.

Then, using e.g. (2.13), usually the resistive voltage drop is neglected (inductive voltage drop much higher due to high injection frequency) as well as the rotor-speed dependent back-emf (since low speeds), and a resulting high-frequency model of the motor is defined as $\underline{u}_s^{dq} = \underline{L}\frac{d\underline{i}_s^{dq}}{dt}$, as in e.g. [19], where $\underline{L}$ is the incremental inductance matrix in the dq-frame if comparing with the PMSM modelling previously presented. The injected voltage vector is then transformed into the real dq-frame and the current response is solved for. The dq-current is a quantity that cannot be measured without knowing the exact rotor position. Thus, according to e.g. [19], the current is transformed into the measurable $\alpha\beta$-current

$$\underline{i}^{\alpha\beta} = I_1 \cdot e^{j\theta_i} + I_2 \cdot e^{-j(\theta_i - 2\theta_r)} \tag{3.1}$$

where I_1 and I_2 are dependent on several factors such as e.g. the inductances in the d- and q-axes, and θ_i and θ_r is the injection angle and the rotor position respectively. According to [19], I_2 is dependent on the difference between the d- and q-inductances. Thus, the position dependent signal might become small for SPMSMs. The current response, described in (3.1), can be processed in order to obtain a rotor position estimate [19]. The following text describes some of the methods found during the literature review process.

The authors of the article [20] investigates a similar rotating voltage HF injection method for initial rotor position estimation for SPMSM. A model of the flux linkages in the d- and the q-axis is made, extending the usual flux-current relationship to a second-order polynomial. The second-order harmonic current response components are used to estimate the rotor position. Further, the estimated position is compensated in order to remove an offset linked with the extended flux equation [20].

In another paper [21], a different approach is presented which is said to be useful for nonsalient machines. A lower frequency signal is applied to the machine and the current response is processed in a phase-locked loop observer that estimates the rotor position. The lower frequency of the injected signal will make the rotor oscillate and the back-emf generated affects the current response which makes it possible to determine the rotor position according to the authors of [21].

In [22], a position estimation method is discussed where a rotating voltage signal is applied to a motor and the rotor position is obtained by evaluating the current response amplitudes. The authors also claim that the strategy could be used with nonsalient machines as well. First, the position of the rotor is estimated knowing the injection angle and the current amplitude. Then, the polarity is found by sending pulses in the direction of the estimated d-axis. The saturation level changes whether the pulse is applied in the positive or negative d-axis and this affects the current amplitude. Similar polarity determination procedures are discussed later.

The paper [23] explains briefly a procedure of processing the current response due to injection of a rotating voltage vector. The current is band-pass filtered and demodulated in order to obtain a position error dependent signal. The error signal is used in an observer in order to decrease the estimation error and thus obtain the rotor position. The method seems to work fine, although it is mainly tested during no load or low load conditions for an SPMSM.

Most of the articles found during the rotating voltage injection literature review

made experiments using several hundreds of Hz for the injected signal while the voltage used differ from a few Volts [22] to some hundred Volts [20]. However, [21] was an exception using a rather low frequency (50 Hz). In the end, the chosen parameters will affect the performance of the methods, but also the losses as will be shortly discussed later.

3.2.2 Pulsating Voltage Injection

The pulsating voltage vector injection principle is basically the same as was discussed in the previous section on rotating voltage injection. A pulsating voltage vector in the estimated d-axis is recommended [24], $\underline{\hat{u}}_s^{dq} = V_{inj} \cdot cos(w_{inj}t)$. This will reduce the torque ripple as the estimated dq-frame approaches the real dq-frame compared to injecting in the estimated q-direction [24]. The current response is used to get an angle error signal which is used to estimate the rotor position.

In [20], a pulsating vector is injected into the $\alpha\beta$-frame in the estimated rotor direction. The current response is processed in order to get a position signal and a magnet polarity signal. The position signal is sent to a control system so that the estimated angle is regulated. The estimated rotor position is then identified looking at the polarity signal as well. The voltage amplitude used was 430 V, which is quite high, and the frequency was 500 Hz. According to the authors, the rotating vector method, also presented in the same paper, had a bit better performance and required less computation time than this pulsating vector method.

In [25] the filtered current response of the injection of a high frequency pulsating voltage signal is used as the input of a PLL (phase-locked loop) in order to track the rotor position.

In the dissertation [26], the author presents general information on injection of a high frequency pulsating voltage into an estimated dq-frame. By expressing this voltage in the real dq-frame, this voltage depends on the angle error between the estimated and the actual dq-frame. It is said that for non-salient machines, pulsating vector injection is not performing well enough.

The paper [24] investigates an pulsating vector injection method where a pulsating voltage is injected into an estimated d-axis while the position information is obtained from the current response in the estimated q-axis for an SPMSM. The current response in the estimated q-axis, which depends on the angle error between the estimated and the real dq-frame, is filtered and processed before it is sent to controllers which returns the position and speed. Some experiments were conducted, e.g. where the motor was subjected to a step of 130% of rated torque. The estimation showed somewhat accurate position detection during standstill (maximum about 0.5 rad deviation (29 degrees) when the torque was stepped). However, for low speed, the error signal became noisier but was in a similar error span as the case before. The authors used an injected signal with 100 V amplitude and 850 Hz. The reason why the injection is not done in the estimated q-axis is said to be the increased torque ripple and losses which would be the result from such injections.

In [27], the resistance dependent current response term is used instead of the usual inductance dependent term. The authors of [27] claimed that this approach is easier to implement and that it gives more stable performance since the induc-

tance e.g. varies with the loading conditions. Furthermore, the authors claim that signal injection methods relying on the difference in inductance demand more signal processing and compensations which makes it hard to obtain good performance in reality. But it is also said that, in the end, it depends on the machine type when it comes to which approach is the most suitable.

In [28], it is said that pulsating vector injection methods generally are more accurate than rotating vector injection methods. Instead of injecting the pulsating voltage vector in an estimated dq-frame, a fixed rotating frame is used [28]. With this method, no observer is needed and the rotor position can be obtained directly using some signal manipulation. Also, it is said that usual pulsating vector injection methods may have convergence problems. One drawback mentioned with this method is that since injecting into a fixed-rotating frame, more torque ripple could be induced compared to other pulsating vector injection methods [28]. Further, the method was tested on a PMSM and for a test where the motor was rotating at 75 rpm, the estimation error span was ± 0.174 radians (± 10 degrees) when compensating for delays in the system.

Another article [29] presents a procedure where the angle error is controlled to zero using a PI controller and the current response signal due to the injected HF voltage. According to the author, no dead-time compensation is needed and that non-linearities in the inverter do not affect the results. This is since the signal is demodulated in a certain way such that these effects are removed.

In [30], the principle of pulsating vector injection into the estimated dq-frame is utilized when injecting a low frequency pulsating current into the estimated d-axis. The current is regulated using a current controller as usual. The reference voltage and the measured current drawn by the machine is used to estimate the back-emf due to the oscillations caused by the low frequency current. Since it is developed for nonsalient PMSM it is an interesting candidate. Since the method relies on vibrations at standstill [30], the rotor has to be able to oscillate and this could perhaps be an issue if the drill is completely stuck. However, some mechanical gaps in e.g. the gearbox might be big enough to let the rotor oscillate.

3.2.3 Square-Wave Voltage Injection

In [26], a square-wave voltage injection method in the estimated dq-frame was proposed for nonsalient SPMSMs. The author argued that there might be a problem using sinusoidal injection when the PWM switching frequency and thus sampling frequency is low since the highest injection frequency will be determined by the PWM switching frequency. Hence, using square-wave injection, this problem is avoided. The simulation results looks promising since the SPMSM used manages to stay in control for loads up to rated load during low speed (1 Hz) [26, p.150].

Other methods which injects square-wave pulses to estimate the initial rotor position are e.g. [31][32]. In [33], a voltage pulse train is applied, each pulse at a certain angular position in the stationary frame, and the rotor position is identified based on the evaluation of the current response amplitudes. If the machine is saturated in a certain angle, the inductance will not be the same as for other positions, and the current response to a voltage pulse applied there would have a

higher amplitude.

In [31], a method is presented in which current pulses are injected during standstill and the energy which is dissipated in the machine after the pulse application is estimated. The minimum energy dissipation is found along the real d-axis. Hence, searching for the position which gives the minimum energy dissipation gives the direction of the d-axis.

Signal injection procedures will induce higher losses in the machine since a signal is injected. The type of the injected signal as well as its attributes (amplitude and frequency), and the machine type affects the temperature increase due to the induced losses originating from the injection of high frequency signals [34]. It is important to consider this when choosing an appropriate method since the temperature increase might damage the machine [34] and also from an environmental point of view it is important to minimize losses.

3.2.4 Inverter-Based Methods

The basics of the inverter-based methods can be described as follows. When switching the switches of a three-phase inverter supplying the motor, the current derivative due to switching in the inverter contain information about the position of the flux in the machine [35] [36]. The underlying principle is that the inductance of the three phases is different depending on where the rotor flux is aligned. Hence, the current change over time will be different in the phases. Combining measurements from the three phases, a position vector is formed [35] [36]. This vector depends only on the current derivative measurements and some constants and is derived from the three-phase model of the machine for two measurements [35]. The estimated position may be shifted from the real rotor position due to load [37]. In [38], the current derivative was measured by sampling the current fast enough so that current samples for each switch state in a PWM period was obtained and the use of current derivative sensors were not needed, however it requires a high sampling frequency. Advantages mentioned for these kind of methods is that the rotor position can be estimated in one PWM cycle and that it does not induce extra losses since no extra test vectors are used [37]. However, a disadvantage is that it requires either high sampling frequency [38] or additional current-derivative sensors [35] [36], and it needs to be modified for short voltage pulses during low speeds [36].

There is another type of the inverter-based methods named INFORM [39]. By injecting switch state voltage vectors, the current change is measured and a reactance can be formed which have information about the flux position [39]. The rotor position estimation is done after three switching cycles [36]. Further, it is said that the angle obtained from the INFORM method during higher loads might be shifted from the real INFORM position [39]. A similar position estimation error was found in [40]. In [41], two current measurements per phase per switch state are done in order to see the current rise in all phases. The data is stored in a table which is used to estimate the position. The table is then used with measurements of current to predict the current change and in that way skip the measurement of current derivatives when the machine is running.

3.3 Observer-Based Techniques

When sensorless operation of the machine is used, some states are not measured (e.g. rotor position and speed). These states are, however, needed for appropriate control of the machine. Some use so called observers to estimate these states from measured signals. The next following sections describe some approaches found in the literature.

As an example of the principle of an observer, the basic structure of a linear observer [42] is

$$\dot{\hat{x}} = A\hat{x} + Bu + K(y - \hat{y}) = A\hat{x} + Bu + KC(x - \hat{x}) \tag{3.2}$$

It is basically a state-space system of the estimated states using feedback of the estimation error [42]. A and B are the state-space matrices for the system's state vector, x, and input vector, u, respectively. C is the matrix used for calculating the output y of the state-space model. The quantities marked as $\hat{x}$ and $\hat{y}$ are the estimated state vector and output vector. The input vector u and the output vector y are known since they are measured from the real system. These signals are used in (3.2) to obtain an estimation of the states.

There are several approaches found in the literature using observers of different kinds, e.g. [26], [43], [44]. One approach is to estimate the back-emf using an observer and this requires some movement if used during standstill, e.g. small vibrations caused by signal injection methods [30], [45].

Sliding mode observers (SMO) have been found to be used in the literature, e.g. in [26] [46]. These are observers having a discontinuous feedback of an estimation error, using for example a sign function (which is done in e.g. [46]). According to [26] [46], sliding mode control is not sensitive to parameter variations. As was also stated in [26], due to practical limitations (sampling time), the convergence may become troublesome. In [46], a sliding mode observer was used to estimate the rotor position and speed. It was found that the system behaved good for speeds above 300 rpm [46].

In [47], the basics of MRAS (Model Reference Adaptive System) is presented as it is used to estimate the rotor speed for a PMSM during high and low speeds. According to [47], an MRAS system is built up with a reference model and an adjustable model. Both are fed with the same input and the outputs are compared to get an estimation error. The error is then used to update the adjustable model so that the error is minimized. The machine model is used as the adaptive model whereas the real machine is used as the reference, and the estimated current is compared with the measured current to provide an error signal in order to estimate the speed and position [47]. Although the method was not tested for different loads, it showed good performance in low speed control [47].

3.4 Magnetic Pole Identification Methods

In [33], the d-axis (rotor) position is first identified as was earlier discussed in Section 3.2.3. When the position of the d-axis is determined, voltage pulses are injected in

the direction of the d-axis. The flux will be affected by this and the current response is investigated in order to determine where the north pole is. When a positive pulse is injected in the positive direction of the d-axis, no torque is produced and the flux linkage increases. This may lead to saturation which lowers the inductance in the d-direction. This in turn increases the current. On the other hand, if a pulse is injected in the negative direction of the d-axis, the flux gets lower and the current amplitude is thus lower. Hence, by injecting pulses on the d-axis and comparing the current amplitudes, the north and south pole may be identified.

The authors of [48] describe a similar method but they first identify the rotor position and then they identify the phase windings which are closest to the rotor. Voltage pulses are then injected in these phases only. In [32], the phase closest to the d-axis is first identified by applying voltage pulses and observing the current amplitudes. When the phase near the d-axis is determined, larger pulses are applied to that phase in order to determine if it is aligned with the north or south pole. The same magnetic pole determination procedure is also used in [29].

In [28], the magnetic pole determination is done by injecting a high frequency signal in the direction of the rotor position. By observing the sign of the average current response in the d-axis, the polarity is found. It is stressed that the polarity investigation is done during standstill otherwise it will fail [28]. In e.g. [49], the magnet polarity is said to be obtainable from certain harmonic components of the current response due to signal injection.

These magnetic pole identification methods found during the literature review depend on the ability to cause saturation in order to affect the current response due to different voltage injection schemes. It is also mentioned in e.g. [5] [48], that using saturation to indicate the polarity of the magnetic field is commonly used.

3.5 Choice of Rotor Position Estimation Methods

At least two methods should be implemented and tested in a simulation environment in order to evaluate which of these is the most suitable position estimation strategy for the project. The methods should be able to start with as high torque as possible and in the correct direction. Considering the environmental aspects, the methods chosen should have as little losses as possible compared to other suitable methods. The chosen strategies have to be stable and must not be the cause of harm to equipment or people, taking ethical considerations into account as well.

In Table 3.1, there are five categories for which the different position estimation methods presented in this chapter have been compared with each other. These categories are: no extra losses, no extra sensors, dependence on dq-inductance difference, and if it works at standstill. The idea behind the table is to give a better overview of some of the different methods and to provide with a better understanding of the choices made later in this section. The "+" means generally that the current parameter (or statement) is true for the chosen method while a "−" means that the parameter (or statement) is not true. Further, if the results of the survey is ambiguous, a "/" is used. Also, the observer-based methods are not included since they were omitted due to difficult control theory and that (at least some, if not all) do not work from standstill, see e.g. [43].

Table 3.1: Comparison between different position estimation strategies.

Parameter\Method	Back-emf	HF inj	PWM-based	INFORM	LF inj
No extra losses	+	−	+	/	−
No extra sensors	+	+	/	+	+
Does not depend on dq-axis ind. diff.	+	/	/	/	+
Works at standstill	−	+	+	+	+

The "No extra losses" criterion measures whether or not the use of the selected method leads to an increase of losses. From an environmental point of view, increased losses is a waste of energy. From a technical point of view, increased losses may lead to increased temperature which can damage the permanent magnets [34]. A "+" in Table 3.1 in this row would mean that no extra losses are induced with the chosen method while the opposite is true for a "−". In Table 3.1, it can be seen that the high frequency signal injection methods ("HF inj", these are the rotating, pulsating and square-wave injection methods) suffer from extra induced losses since extra signals are injected which may induce losses [34]. Since the low frequency signal injection methods ("LF inj") are also based on injecting extra signals, it is assumed that these also induce extra losses although no actual research on this specific subject has been found. When it comes to the INFORM method, an article has been found where it says that INFORM usually depend on extra signal injection but it also describes an option without having to inject extra signals [41]. No further research has been found on losses related to INFORM during the literature survey. Therefore, it is given a "/". Since the back-emf estimation based methods, such as the SCVM implemented in [7], rely on measured signals, no extra signals are injected and thus it is assumed that no extra losses are induced. No research papers have been found on this subject either. As stated earlier, the inverter-based methods ("PWM-based"), except (most) INFORM as described before, do not rely on extra signal injection and, hence, do not induce extra losses.

The "No extra sensors" criterion tells if the chosen method needs extra sensors in order to work, such as current derivative sensors as was mentioned for some inverter-based methods earlier. The need for extra sensors is not good, since then a position sensor could likewise be used. Also, the extra sensors could increase the cost and take extra space. For this criterion, a "+" in Table 3.1 in this row would mean that the chosen method does not need extra sensors while a "−" would mean the opposite. The back-emf estimation based methods, the high and low frequency injection based methods found in the literature review do not need extra sensors since they basically need only current sensors, see e.g. the implementations in [7] [24] [30]. The inverter-based methods ("PWM-based") have been found to be implemented with extra current derivative sensors [35] but there are also some implementations that do not need extra sensors, e.g. [38]. Thus, a "/" is put in Table 3.1 for the PWM-based methods. The INFORM method seems to be possible to implement without current derivative sensors since the injected voltage vectors are applied in different PWM cycles and, hence, the current change is calculated using samples from two cycles [40]. Further, another INFORM approach using no

current derivative sensors was realized in [41].

The next criterion regarding dependence on inductance difference between the dq-axes connects to the aspect of saliency. This is important since the machine looked at is a nonsalient SPMSM. Hence, it is important that the chosen method works for nonsalient machines. A "+" would mean that the method works for nonsalient machines and do not depend on the dq inductance difference while a "−" means the opposite. The back-emf estimation methods do not depend on the dq inductance difference, see e.g. [4] for a derivation of the SCVM which is a back-emf based estimation method. The inverter-based methods (PWM-based) depend on the rotor position dependence of the three-phase inductance [35] [38] so they should be affected by this parameter. However, in e.g. [37] and [38], PWM-based methods were shown to work with SPMSMs. In [40], it can be seen that the INFORM method depends on the dq-inductance difference. However, in [39], the INFORM is developed for several machine types, including SPMSM. Hence, for both inverter-based method, "/" is used Table 3.1 to describe the ambiguous results regarding this topic, although it should be noted that PWM-based methods have been shown to work with SPMSMs and an article has been found describing INFORM for SPMSMs. The low frequency signal injection method found in this literature survey rely upon torque and speed ripple to cause measurable back-emf [30] and does not depend on the inductance difference [30]. Most of the high frequency signal injection methods found in this survey rely on some inductance difference, e.g. [19] [24] [26], but there is also an article describing an option, a high frequency signal injection method relying on the dq resistance difference [27]. Hence, it is given a "/" in Table 3.1.

The last criterion is "Works at standstill". In order to start properly, the rotor angle at standstill should be estimated well enough. A "+" would mean that the method works from standstill and a "−" means the opposite. The high frequency signal injection methods work from standstill, see e.g. [24]. The low frequency signal injection method found needs vibrations or rotor oscillations at standstill to work since it depends on the back-emf estimation [30]. Hence, it is not complete standstill but according to [30] the method can be tuned so that no larger rotor movements are present. The INFORM works from standstill according to [39]. The other inverter-based methods found to be working for standstill as well [35]. Lastly, the back-emf based estimation methods need to be able to register back-emf which is not possible at zero speed [7].

In the end, the choice was made after taking all the aspects visualized in Table 3.1 into consideration and choosing the methods that were the easiest to test. This is of course a subjective choice.

The inverter-based methods (PWM-based and INFORM) were omitted due to the ambiguous results in the survey (see Table 3.1) and that they were thought to be difficult to implement in a simulation. It should be noted, however, that they would have been interesting to test since they have some appealing features such as they work from standstill and may be implemented without inducing extra losses during usage.

This left the signal injection methods and the back-emf based estimation schemes. From these, it is obvious looking at Table 3.1, that the back-emf based methods and the low frequency signal injection methods would be more suitable than the high

frequency injection ones since they both scored one more "+" (if the resistance-difference high frequency method is not considered). Hence, the SCVM and a low frequency injection method [30] was chosen. Due to difficulties in making the low frequency injection method work properly (the back-emf observer was not working as it should) and due to time limitations, a simple high frequency signal injection method [24] was chosen instead to be compared with the SCVM. It is, however, important to add that methods such as the low-frequency injection method in [30] are probably more suitable for SPMSMs than [24] since it is not dependent on inductance differences which could become small for SPMSMs.

Further, magnet polarity detection should be done in a real drive system before starting. In this project, this aspect has not been fully tested due to time limitations. However, a simple polarity identification method was implemented based on voltage pulse injection in the estimated d-axis as described in e.g. [48]. No further comparison between the polarity identification methods was done.

4

Characterization and Simulation of the SPMSM

4.1 Identification of Model Parameters

In order to validate the performance of the position estimation methods, a proper machine model has to be used. As was stated in Section 2.2.2, a machine model can be derived which takes saturation and cross-coupling effects into considerations. However, to be able to use such a model, the machine model parameters has to be identified, namely the stator resistance, the incremental inductance as well as the absolute inductance.

4.1.1 Resistance Measurements

The resistance measurement procedure is described in this section although it should be straightforward. It is a basic DC measurement. The motor was fed with DC voltage from a DC supply over two phases where the input current was set in the DC supply. The voltage was then measured with a multimeter and the current was read from the DC supply monitor.

The measurements were done between two phases, then one phase was switched. Thus, only the resistance in the equivalent circuit of the phases e.g. AB and BC was measured. This was done only to see if the resistance was approximately the same in the different phases. The two phases become connected in series, since Y-connected stator, as seen in Figure 4.1.

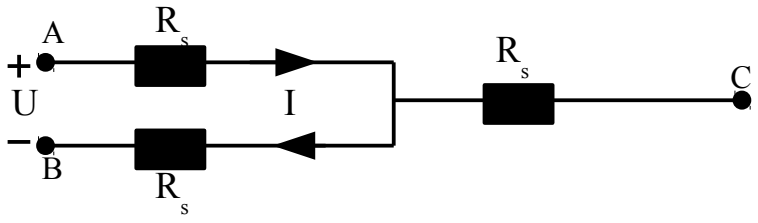

Figure 4.1: A simplified sketch showing the two measured phases and how the current flows, thus making the equivalent resistance equal twice the stator resistance, i.e. $2R_s$.

The test was done quickly in order to mitigate the temperature effect on the stator resistances. It was noticed in a preliminary test that the voltage drifted when a set

current was applied. This was thought to be the result of the growing resistance due to a higher temperature.

The resistance was measured on two equal motors. The results for the first motor are presented in Table 4.1 where only the results for one phase combination is shown. The measurements showed that the phase resistance was independent of the phase combination as is reasonable.

A second measurement on an identical motor was done which confirmed the results and the results are found in Table 4.2. This was done since the rotor flux measurements, see below, could only be done on this second motor due to practical reasons while all the other flux measurements were done on the first motor. Therefore, it is assumed that the motors are identical and that the flux is the same for both of them, making it possible to use the rotor flux magnitude measured from one motor and the inductance values measured from another motor in the machine model later on.

Table 4.1: Stator resistance measurement (machine 1).

Voltage [V]	Current [A]	Phase resistance [Ω]
2.1	1	1.05
4.3	2	1.075
6.5	3	1.083

Table 4.2: Stator resistance measurement (machine 2).

Voltage [V]	Current [A]	Phase resistance [Ω]
2.17	1	1.085
4.33	2	1.083

Since the resistance, see Table 4.1, drifted for higher current, most probably due to temperature effects, only two current set points were used for measuring on the second machine, as is seen in Table 4.2. The second machine was, prior to the resistance measurement, included in a rotor flux measurement and this might have heated the machine a bit. This is thought to be the reason why the resistance is slightly higher for low currents for machine 2 than for machine 1. Hence, the resistance is thus determined to be 1.05Ω.

The resistance of the cable, which normally supplies the motor, was not included nor measured and therefore is not included in the results. It is important to stress that the cable was not connected during the measurements above. This is reasonable since the stator resistance of the machine was sought for.

4.1.2 Flux Measurements

In order to complete the machine model, the inductances need to be determined. To get more realistic results, the chosen machine model takes saturation into account. Therefore, the inductances need to be mapped for different current levels. The inductances are then determined from the flux. The following subsections will

describe the methods used for identifying the flux for a test machine and will discuss the implications of the choice of measurement methods and simplifications made.

The machine flux has been measured using two separate strategies. This was done in order to compare the measurements so that the machine model parameters dependent on the flux (the incremental and the absolute inductances) can be determined accurately enough. Firstly, a description on how the rotor flux magnitude was obtained is given. Secondly, a standstill flux measurement is discussed and the results are given. Thirdly, a constant speed flux measurement is discussed. Lastly, a comparison between the results and methods is provided.

4.1.2.1 Rotor Flux Measurements

In order to determine the rotor flux magnitude needed for the machine model (2.13), an open-circuit measurement was done according to Figure 4.2. In Figure 4.2, two drill machines using the same motor type were mechanically connected to each other (M_1 and M_2 in the figure) through the shaft. The motors were attached to a stand so that they would be still. One of the motors (M_2) were driven by a controller and was set to operate at a constant speed of 4368 rpm (mechanical). The reason why the number is a bit specific is due to the gears, the mechanical speed on the shaft was set to 245 rpm. The other motor (M_1) had its stator windings open so that no current would flow through the conductors. The open-circuit stator voltage of this motor was measured line-to-line since the neutral point in the machine was not accessible. Two line-to-line voltage combinations were measured on separate channels with an oscilloscope. This measurement procedure was also done with a different speed (6419 rpm) to validate the results.

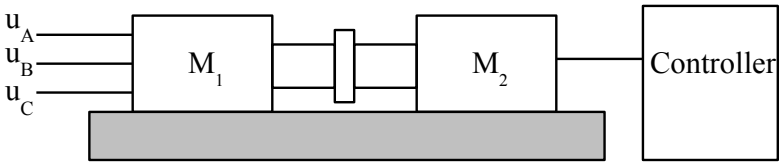

Figure 4.2: The measurement setup for rotor flux magnitude identification. M_1 is the measured machine, M_2 is the controlled machine driving M_1. The controller ensures a constant speed.

Since the machine circuit is open no current flows through the windings which results in no resistive voltage drops. Also, no stator flux will be induced from the stator windings, only the rotor flux make up the total flux of (2.5). The rotor flux can be described as stated in (2.6) and the machine equation become

$$\underline{u}_s^{abc} = \frac{d\underline{\lambda}_{PM}^{abc}}{dt} = \sum_{n=1,3,5,7,\ldots} -n\omega_r \lambda_{PM,(n)} \begin{bmatrix} sin(n\theta_r) \\ sin\Big(n(\theta_r - \frac{2\pi}{3})\Big) \\ sin\Big(n(\theta_r - \frac{4\pi}{3})\Big) \end{bmatrix} \tag{4.1}$$

where n denotes the harmonic order. When measuring the line-to-line voltage, the

resulting voltage amplitude become $\sqrt{3}$ times larger than the phase voltage. Hence, considering only the fundamental components, the following hold

$$\lambda_{PM,(1)} = \frac{u_{ij,(1)}^{peak}}{\sqrt{3}\omega_r} \text{ for } i,j = \{a,b,c\}, i \neq j \tag{4.2}$$

where u_{ij}^{peak} is the line-to-line voltage amplitude. Using the relation given in (4.2), the fundamental rotor flux magnitude can be obtained from the measured line-to-line voltages.

In Figure 4.3, the line-to-line voltage is seen from a measurement when the rotor was running at 4368 rpm. As described, the rotor flux is proportional to the line-to-line voltage and from Figure 4.3, it is obvious that the rotor flux contains harmonics that are dependent on the rotor position. Hence, in order to determine $\lambda_{PM,(1)}$, an FFT had to be made in order to find the fundamental component of the line-to-line voltages. As an example, the resulting FFT for the first channel (4368 rpm) is seen in Figure 4.4. The most significant harmonics are the fifth and seventh harmonics which are visible in Figure 4.4.

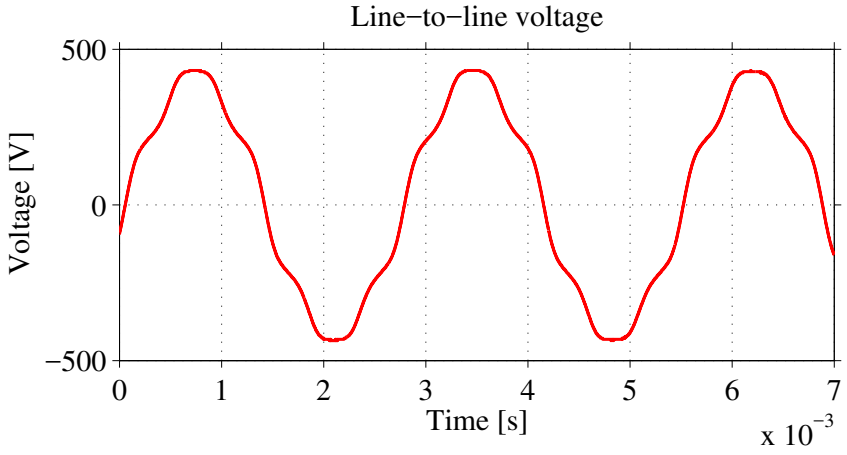

Figure 4.3: Line-to-line voltage measured for channel one during the first measurement (4368 rpm).

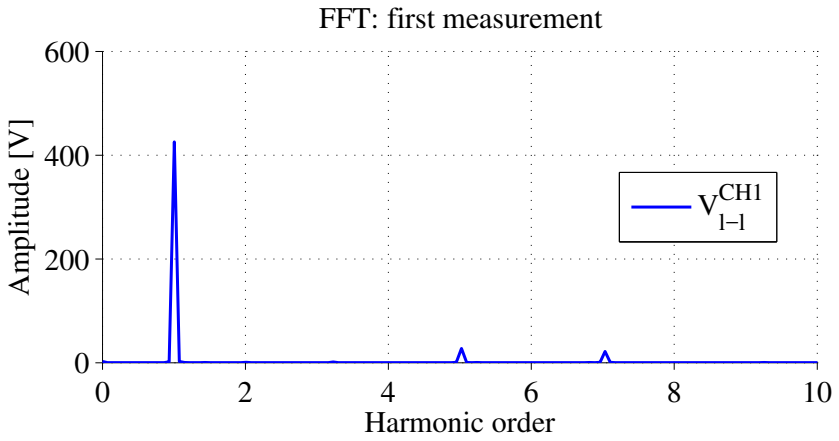

Figure 4.4: Frequency spectrum for the line-to-line voltage on channel one during the first measurement (4368 rpm).

Since the machine model only concerns fundamental components, the fundamental voltage component was determined from the results of the FFT and the rotor flux magnitude was calculated knowing the constant speed. The results from both channels for each measurement are found in Table 4.3. It is seen that the rotor flux magnitude are almost the same for the two channels in each measurement. However, there is a difference between the results of the two measurements. The rotor flux magnitude is seen to be higher for 6419 rpm than for 4368 rpm. This is believed to be the result of temperature effects as the rotor flux linkage decreases with increasing temperature [13]. Due to difficulties to incorporate a water cooling procedure during the measurement, this was omitted and the drill became warm during the measurements. The second measurement (6419 rpm) was made quicker than the first. It is believed that the machine was cooler during the second measurement since the measurement was done faster. The rotor flux is lower in the first measurement, probably because it likely achieved a higher temperature. Hence, the rotor flux is considered to be about 0.11 Wb.

Table 4.3: Fundamental rotor flux comparison for the two different measurements.

	4368 rpm	**6419 rpm**
"Theoretical"	0.1154 Wb	0.1154 Wb
CH1	0.1074 Wb	0.1102 Wb
CH2	0.1078 Wb	0.1097 Wb

4.1.2.2 Standstill Flux Measurement

The machine flux could also be determined using a standstill flux measurement, e.g. similar to what is discussed in [13]. During such a procedure, the rotor is mechanically locked into a known position. The position can be set by applying a constant voltage vector in the $\alpha\beta$-frame, the rotor will then try to align itself to this position. Due to friction, the rotor might not be able to align exactly into this position. Hence, when the rotor has aligned itself towards the vector, the rotor can

be shifted a little bit to the right and to the left around the point where it stopped moving. This way, the actual set position might be manually found. When this is done, the rotor is mechanically fixed and combinations of dq-current references are applied with the current controller. The voltage is either measured or estimated and the resulting flux is calculated during the transient using

$$\underline{\lambda}_s^{dq} = \int_{t_0}^{t_1} (\underline{u}_s^{dq} - R \cdot \underline{i}_s^{dq}) dt + \underline{\lambda}_0^{dq} \tag{4.3}$$

where t_0 and t_1 is the start time and end time of the transient period. During the steady-state, the applied stator voltage and the resistive voltage drop are the same and the time derivative of the flux is zero. This method determines only the current induced stator flux since the time derivative of the rotor flux in the dq-frame is zero. Thus, the total flux is the sum of the flux from (4.3) and the rotor flux component determined in Table 4.3. As was seen for the rotor flux case, there were position-dependent harmonics. Therefore, the result of this measurement depends on which rotor position the rotor is locked. However, the model used in this report does not take these harmonic effects into account and this introduces some errors in the parameter identification. $\underline{\lambda}_0^{dq}$ is the flux which could be existant before a change in current or voltage is done.

Combinations of dq-current references is automatically set to the current controller, each combination lasting for two seconds. The currents resulting from these combinations can be seen in Figure 4.5. When the current reference is set, the current controller outputs a voltage. This voltage reference is applied to the machine and the current starts changing. As the current increases, the voltage reference decreases towards a new steady-state. During this transient period, the flux changes and affects the voltage needed to achieve the current controller objective. Therefore, the voltage reference in dq is used as $\underline{u}_s^{dq}$. This comes with some errors due to inverter non-linearities and voltage drops in between the controller and the machine. These aspects are to be discussed further later. The dq-current is measured.

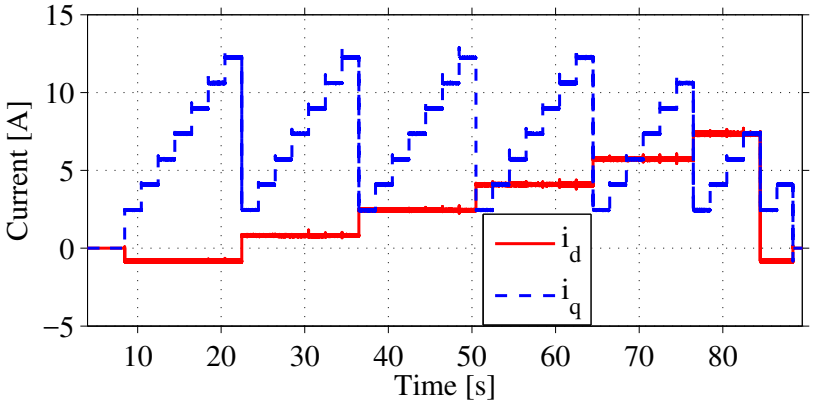

Figure 4.5: i_d and i_q sampled, locked rotor. The current components are controlled to certain references, these combinations seen during the steady-state portions of the graphs above.

The midpoint of each transient, T_{mid}, was identified and then, from these midpoints, each transient's start time (t_0) was set as the midpoint minus 2 milliseconds. The transient's endpoint (t_1) was the result of the addition of the midpoint value and 35 milliseconds. The length of the transients are therefore the same for all calculations and the subtracted as well as the added value were chosen from inspecting the worst case transients approximately so that the procedure would capture all transients well enough. The steady-state portions were assumed to be the parts in between the transients, stretching 0.7 seconds from the startpoint and endpoint of each transients. These steady-state portions were used in order to calculate the resistance which was used in (4.3). It was observed that the resistances fluctuated a bit and were not always the same before and after a transient. Hence, the difference between the midpoint and the startpoint of the transients was minimized, and the resistance for the steady-state part after each transient was used in (4.3). This was done in order to reduce the calculation error due to the difference in resistance.

In Figure 4.6, the transient of the d-voltage against the resistive voltage drop can be seen as an example for the measurement procedure. The difference is integrated over the transient time period, according to (4.3), and λ_{d0} is the d-flux calculated from the transient before, assuming it is zero from the beginning. The output voltage of the controller is sampled and the current drawn by the machine is also sampled. The change in voltage reference give rise to a change in current as can be seen in Figure 4.6.

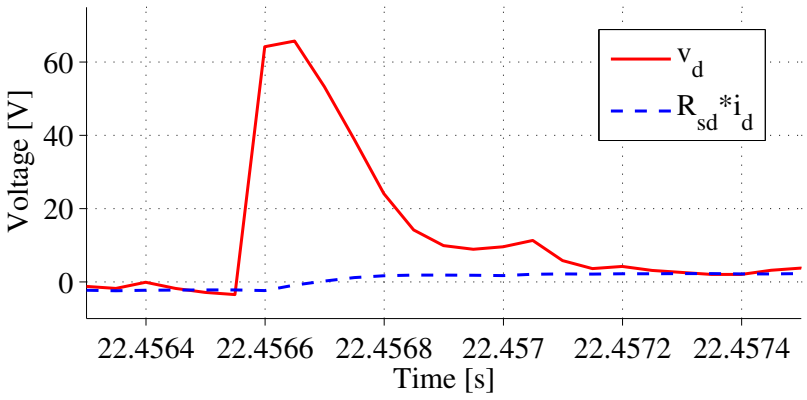

Figure 4.6: v_d compared with the resistive voltage drop during a transient.

There is a time delay which affects the measurement results. The output voltage is passed through a filter. This filter delays the current response to the output voltage from the current controller. Further, the sampled current is delayed half a sample period compared with the commanded voltage. Hence, the current's total delay time equals the sum of these. The sample frequency is 20 kHz, while the filter consists of an RL series connection. The time constant of a series RL circuit equals $\frac{L}{R}$. The inductance is said to vary between 30 μH and 40 μH depending on the current, and the resistance is the phase resistance of the machine ($\approx 1\ \Omega$). Summed up, the time delay is in the range $t_{delay} = 55, 65\ \mu s$. In order to simplify the analysis, a time delay of 60 μs was chosen. Hence, the current signal was shifted 60 μs towards origo.

However, since the time difference between each sample is $T_s = \frac{1}{20000Hz} = 50\ \mu s$, the shifting is made assuming it is possible to linearly interpolate between two samples. Using that assumption, it is possible to imagine $n = \frac{T_s}{\tau_{delay}}$ number of points linearly distributed between two samples. Having the slope between two samples $i(k)$ and $i(k+1)$ defined as $\delta = \frac{i(k+1)-i(k)}{T_s}$, the resulting time shifted signal is determined using $i_{shift,k} = i_k + \delta \cdot t_{delay} = i_k + \frac{i(k+1)-i(k)}{n}$. The approximation is verified comparing the real signal, the real signal where the time vector has t_{delay} subtracted from it and the shifted signal using the above derived formula. The result is seen in Figure 4.7 below. It is seen in Figure 4.7a that the shifted signal, red dots, follows the real signal whose time vector has been altered, green, which supports the claim. However, if zoomed in further it is seen that the values of the shifted signal is somewhat different at some places but the difference is assumed to be negligible for the purpose here, as seen in e.g. Figure 4.7b.

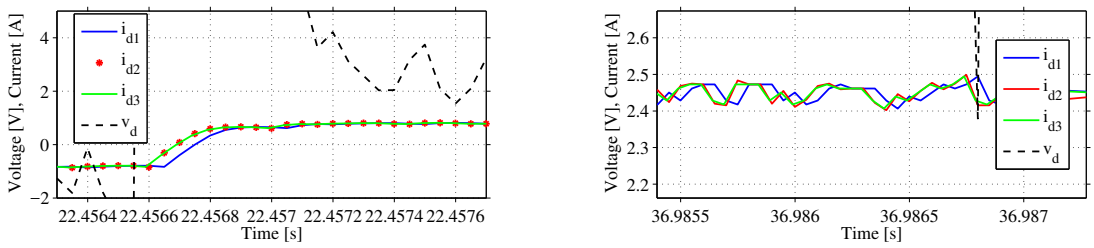

(a) **(b)**

Figure 4.7: A transient zoomed in. i_{d1} is the unshifted sampled d-current, i_{d2} is the d-current shifted using the technique described, i_{d3} is the d-current with altered time vector so that its time vector is shifted 60 µs. v_d is the d-voltage reference.

The resulting d- and q-component fluxes are seen in Figure 4.8. The d-component flux is seen to slightly saturate for higher d-currents. However, there is a sudden increase in the flux derivative for the last d-current which is believed to be the result of a measurement error. The q-flux looks like it saturates a bit as well for higher q-current. Further, it is seen that the q-flux decreases when the d-current increases. Also, the d-flux decreases with higher q-current. There are also two unexpected events in the flux figures. It is seen that for high d-current, the d-flux starts increasing again. This is probably due to some measurement error since if the flux saturates, there would be no such increase for high currents. Also, it is seen that for the q-flux, and low q-current and high d-current, the flux increase is negligible and the flux is negative. Suddenly, at about $i_q = 6$ A, the q-flux starts increasing again. Perhaps, the negative flux might be explained by the relatively high d-current, so that d-flux leaks into the q-axis and that when the q-current becomes big enough, the q-flux increase above zero and keep increasing with the q-current. However, the actual reason is not known to the author. The results from this measurement has to be compared to another measurement in order to be able to make better conclusions.

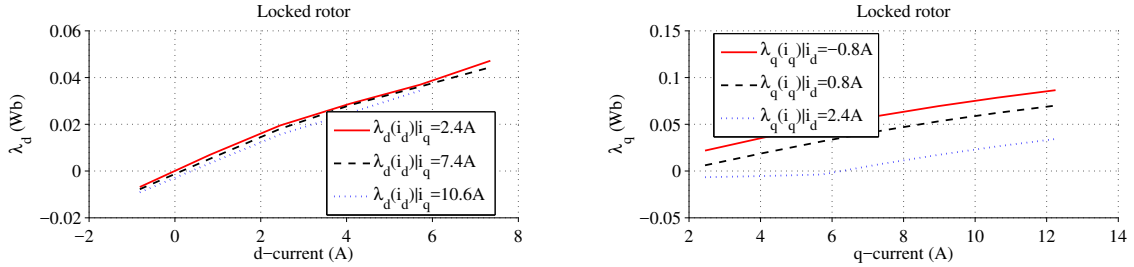

(a) $\lambda_d(i_d)$ **(b)** $\lambda_q(i_q)$

Figure 4.8: The resulting dq-flux from the standstill measurements (PM rotor flux not included).

4.1.2.3 Constant Speed Flux Measurement

With the current laboratory setup, the following method was deemed suitable. The flux in d- and q-axis was mapped for different combinations of d- and q-axis currents during rotation of the rotor, such as the method described in e.g. [13]. However, the machine itself produced the rotation via a speed controller. Using the motor model described by (2.13), the flux derivative can be assumed to be equal to zero during the steady-state. The fundamental components of the steady-state currents and voltages were used by performing a mean-value calculation on the waveforms in steady-state. Hence, the d- and q-flux components can easily be obtained for different current combinations (note, the PM rotor flux is going to be taken into account) as

$$\begin{aligned} \lambda_d &= \frac{u_{sq} - R_s i_{sq}}{\omega_r} \\ \lambda_q &= \frac{R_s i_{sd} - u_{sd}}{\omega_r}. \end{aligned} \tag{4.4}$$

The lab setup was based on the tested motor connected through the shaft of another machine which can only be controlled to brake. It was set to brake at a certain maximum speed, below that speed, the speed regulator controlled until a certain threshold. The tested motor was water cooled and thus the temperature effects on resistance were neglected. The current combinations were set to as references to the current controller and held for two seconds each, as for the locked rotor measurement described above. The sampling frequency was set to 20 kHz. Also, these current combinations had a limited magnitude such that the total current did not exceed the nominal current.

The set speed was chosen to be rather high (4000 rpm) since no position sensor was available. During high speeds, the angle estimator (which was already implemented) worked fine and was used to estimate the position and speed for the measurements. The high speed gives rise to a high back-emf. Hence, the lack of dead-time compensation is negligible. For the post-processing, the data was loaded into MATLAB and only the last second of each combination was used. This was since during the last second, steady-state was obtained.

Other effects that are neglected are the frequency dependency due to skin effect for the stator resistance (since speed fluctuations and a rather high speed (4000rpm) the real resistance is probably not equal to the measured DC resistance which was discussed above), the cable resistance was not either taken into account.

In Figure 4.9, the resulting d- and q-flux is visualized. Both flux components look smooth. The d-flux, seen in Figure 4.9a, is saturating for higher d-current and decreases with increasing q-current as for the locked rotor measurements. The d-flux from the constant speed measurement includes the rotor flux (0.11 Wb). Hence, in order to compare the d-flux in Figure 4.9a with the d-flux in Figure 4.8a, 0.11 Wb has to be subtracted from the d-flux in Figure 4.9a. The q-flux, seen in Figure 4.9b, does not show any saturation behaviour, as it did for the locked rotor case. It increases linearly with the q-current. Further, it increases with the d-current as well. This is completely the opposite for what happened in the locked rotor case. One difference between these two measurements is that when having the rotor running at a high speed, the frequency of the flux and the other signals is quite high while as when the rotor is locked, the frequency is low. This might be causing these effects. Also, since the methods are completely different, there are different measurement errors that has to be taken into account. The next section discusses this further.

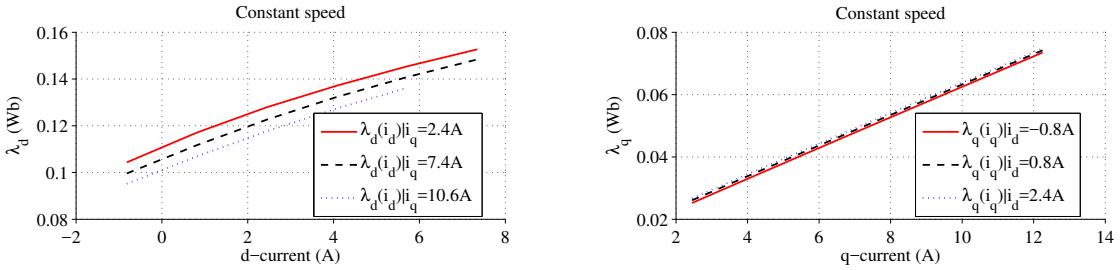

(a) $\lambda_d(i_d)$ **(b)** $\lambda_q(i_q)$

Figure 4.9: The resulting dq-flux from the constant speed measurements (PM rotor flux is included).

4.1.2.4 Flux Measurements Comparison

Comparing the d-flux in Figure 4.8a and the d-flux in Figure 4.9a (after the addition of the PM rotor flux 0.11 Wb to the d-flux in Figure 4.8a), it is seen that the d-flux is rather similar in both tests: having $i_q = 2.4$ A and $i_d = 7.4$ A, the d-flux from the locked rotor test is about 0.1572 Wb while it is 0.1527 Wb in the constant speed test. At $i_q = 10.6$ A and $i_d = -0.8$ A, the d-flux in the locked rotor test is around 0.1 Wb while it is 0.095 Wb in the constant speed test. Hence, the d-flux is rather similar in both test cases.

Looking at the q-fluxes in Figure 4.8b and in Figure 4.9b, there are some differences. At $i_d = 0.8$ A and $i_q = 12.3$ A, the q-fluxes are rather similar as it is about 0.074 Wb in the constant speed case while it is around 0.07 Wb in the locked rotor test. However, the shape and behaviour of the q-fluxes differ between the cases and at $i_d = 2.4$ A and $i_q = 2.4$ A, the constant speed measured q-flux is about 0.027 Wb while it is -0.007 Wb for the locked rotor test. Hence, as could also be seen in the

figures, the d-flux from the measurements are similar to each other while the q-flux differs.

There are different measurement errors for the different procedures and in order to make a better choice for which results to use, an error analysis is provided below. The following are the main errors found for the locked rotor measurement:

- The rotor was not completely still when changing current references, it transiently moved. This movement was mitigated by trying to fix the rotor using available items. However, a small movement was still seen for some current combinations (when changing current reference values the rotor moved a little).
- There were filters for the output voltage, an attempt to compensate for the delay was made. The time constant of the filter was used as a constant time delay. The filter inductance was said to be changing for different current levels. Hence, an inductance value in between the two extremes was used when calculating the time delay. The result is not exact and this is thus an error source.
- No dead-time compensation was made. This can have serious effects for low voltages. For locked rotors, no back-emf will be induced, and only a low voltage is needed to achieve the current references used. Therefore, dead-time voltage drops will have an effect on the results. These voltage drops are proportional to the DC-bus voltage. Hence, the DC-bus voltage was lowered (200 V) which should result in an approximately 2 V drop for the specific dead-time.
- The data acquisition system lost packages of sampled information every now and then. Therefore, some transients might have suffered from this which can result in bad flux measurement results.
- In reality, the flux may have harmonics which are rotor position dependent. Since the rotor was locked at a specific position, the flux at that position might have been at a minimum, maximum or something in between.

The following lists the errors found for the constant speed measurements:

- Constant speed was hard to achieve with the equipment used. However, the mean values were used for the specific intervals (as explained) which would reduce this error.
- Harmonics are always present (dependent on rotor position). However, this error was reduced by using the mean values over a relatively long interval (as explained).
- The same data acquisition system was used. Therefore, similar data loss problems might have been the case (not investigated). However, the constant speed measurements consider only the mean values during the steady-state which makes it less vulnerable to these kinds of trouble as compared with the locked rotor tests.
- When operating a machine in a certain speed, the frequency of the electric input signals would be higher than when the machine is operated at a lower speed (or standstill). Frequency affects e.g. the resistance (skin effect) and this was not taken into account which could affect the results from the measurements.

First of all, the constant speed measurements do not suffer as much from the dead-

time error effects. Since the back-emf is sufficiently high, the dead-time voltage drop can be neglected.

Furthermore, both measurement procedures were affected by the higher resistance from the line connecting the machine with the controllers. This was not taken into account and affects the calculated flux in the end. Also, other voltage drops were not taken into account either.

As explained, the constant speed measurements are less affected by data acquisition errors and dead-time effects. Also, the effect of harmonics are less pronounced in the constant speed measurements due to the fact that mean values are used. The mean values are evaluated over a relatively long period over the steady-state portions of the signals, as said before. However, it is difficult to maintain constant speed with the measurement equipment used but it is believed that taking the mean values, this effect is decreased.

When comparing the figures which shows the d- and q-fluxes calculated for the two tests (see Figure 4.8 and Figure 4.9), it is seen that the fluxes resulting from the constant speed measurement looks smoother.

4.1.3 Inductance Calculation

The incremental inductances and absolute inductances, see (2.14) and (2.15) respectively, can be determined using the results from the flux measurements [13]. The incremental inductance is calculated using an approximation of the derivative as

$$\begin{aligned} l_{dd,ij} &= \frac{\lambda_{ds,i+1,j} - \lambda_{ds,i-1,j}}{i_{ds,i+1} - i_{ds,i-1}} \\ l_{dq,ij} &= \frac{\lambda_{ds,i,j+1} - \lambda_{ds,i,j-1}}{i_{qs,j+1} - i_{qs,j-1}} \\ l_{qd,ij} &= \frac{\lambda_{qs,i+1,j} - \lambda_{qs,i-1,j}}{i_{ds,i+1} - i_{ds,i-1}} \\ l_{qq,ij} &= \frac{\lambda_{qs,i,j+1} - \lambda_{qs,i,j-1}}{i_{qs,j+1} - i_{qs,j-1}} \end{aligned} \tag{4.5}$$

where $l_{dd} = \frac{d\lambda_{ds}}{di_{ds}}$, $l_{dq} = \frac{d\lambda_{ds}}{di_{qs}}$, $l_{qd} = \frac{d\lambda_{qs}}{di_{ds}}$ and $l_{qq} = \frac{d\lambda_{qs}}{di_{qs}}$ denotes the elements in (2.14) for simplicity. The subscript i denotes a certain d-current while j denotes a certain q-current for which the flux was determined. The letters i and j can be regarded as indices in a table where the d-currents are in the leftmost column, the q-currents in the top row and the measured flux as table elements. This procedure was proposed in e.g. [13] or [50]. The inductances at the end of the measurement spectrum had to be determined by extending the flux to i,j=-1 (the first chosen currents have indices i,j=0) and i,j=N+1,M+1 respectively by assuming that the flux change was linear and constant between the points (i.e. linear extrapolation). N denotes the number of d-currents and M denotes the number of q-currents chosen.

A similar procedure was done for the absolute inductances using the flux relations, as was proposed also in [13]

$$L_{d,ij} = \frac{\lambda_{ds,ij} - \lambda_{PM}}{i_{ds,i}}$$
$$L_{q,ij} = \frac{\lambda_{qs,ij}}{i_{qs,j}}. \tag{4.6}$$

The resulting absolute inductances from the constant speed and locked rotor measurements can be seen in Figure 4.10 as blue dots while the surfaces are linearly interpolated between the dots.

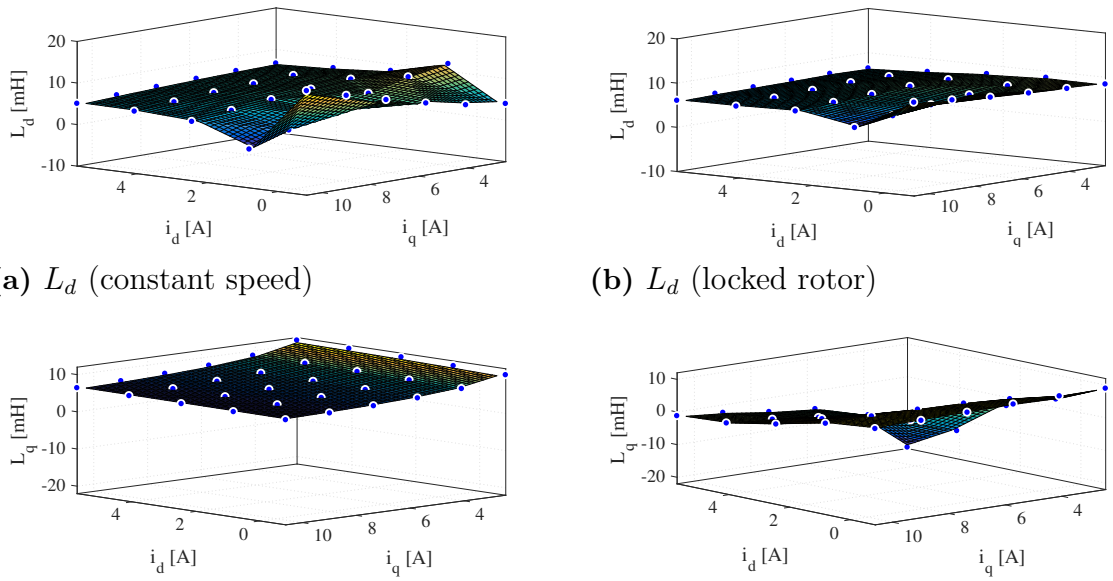

(a) L_d (constant speed)

(b) L_d (locked rotor)

(c) L_q (constant speed)

(d) L_q (locked rotor)

Figure 4.10: Constant speed and locked rotor absolute inductances.

Comparing L_d in Figure 4.10a and Figure 4.10b, a similar shape can be seen, i.e. it seems to decrease with increasing d-current. However, in both figures a local minimum can be seen for low positive d-current and high q-current. This seems strange since it would imply that the d-flux becomes saturated only to become less saturated again when the d-current continues to increase. Furthermore, the behaviour is seen in both measurements.

The L_q differs a lot between the two measurements, as seen when comparing Figure 4.10c and Figure 4.10d. The constant speed measurement shows that the L_q decreases with increasing q-current and does not seem to be largely affected by changes in the d-current (except for low q-current). In Figure 4.10d, it can be seen that L_q decreases with increasing d-current and becomes negative for high d-currents (especially for low q-currents). No larger changes were visible when increasing only the q-current (except for high d-currents). It should be remembered that the absolute inductances includes possible cross-coupling phenomena due to the calculation method (4.6).

The resulting incremental inductances from the constant speed measurement and the locked rotor measurement can be seen in Figure 4.11 and in Figure 4.12, also

as blue dots while the surfaces are interpolated between the data points. Generally, the inductances from the constant speed measurement looks smoother, compare e.g. Figures 4.11a and 4.11b. The differences could be due to measurement errors. Looking at the incremental self-inductance of the d-axis, a similar saturation behaviour is seen for both measurements for l_{dd}, i.e. for high d-currents the incremental self-inductance decreases which implies that the d-axis becomes saturated (see Figures 4.11a and 4.11b). This behaviour is also seen in the d-fluxes, visualized in Figure 4.8a and Figure 4.9a.

Comparing l_{qq} between the locked rotor case (Figure 4.11d) and the constant speed case (Figure 4.11c), it can be seen that the locked rotor l_{qq} features a strange decrease for a certain current range and then increases again which is not seen in the constant speed l_{qq}. This behaviour is strange since it would mean that there is a saturation effect active for only certain dq-current combinations, and then when the current increases, the saturation effect disappears. This is not seen in the constant speed l_{qq} which has a more logical appearance, the incremental self-inductance in the q-axis decreases with increasing q-current. This would imply that the q-axis becomes saturated for high q-currents which is logical. Further, the change in l_{qq} for the constant speed case is very small and in Figure 4.9b, it can be seen that the q-flux does not seem to change visibly for higher q-current. However, in the locked rotor measurement, the q-flux (see Figure 4.8b) is seen to saturate for higher q-currents. At least for low d-currents, it is seen in Figure 4.11d that l_{qq} decreases a bit with increasing q-current.

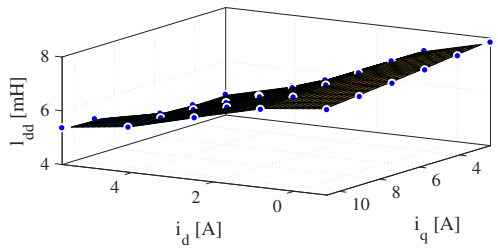

(a) l_{dd} (constant speed)

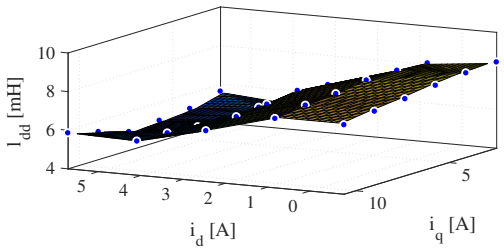

(b) l_{dd} (locked rotor)

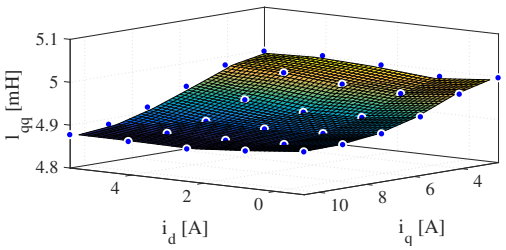

(c) l_{qq} (constant speed)

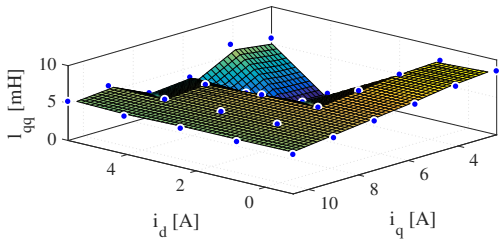

(d) l_{qq} (locked rotor)

Figure 4.11: Constant speed and locked rotor incremental inductances.

The cross-coupled inductances l_{dq} and l_{qd} respectively differs a lot between the two measurements. It is seen in Figure 4.12a that the l_{dq} for the constant speed case is negative for the tested current range while it is positive for low q-current and high d-current for the locked rotor case, see Figure 4.12b. The biggest differences seen

between the measurement cases for the incremental inductances are seen for the l_{qd}, where it becomes rather negative for the locked rotor case. The two measurements had different errors which affects the results, and this could be the reason behind the differing inductances, the rotor was e.g. not completely still for all cases when switching current combinations in the locked rotor test. See Section 4.1.2.4 for a comparison between the measurement errors for the two cases.

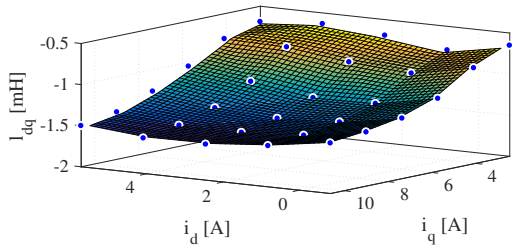

(a) l_{dq} (constant speed)

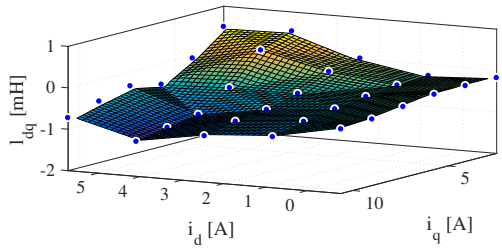

(b) l_{dq} (locked rotor)

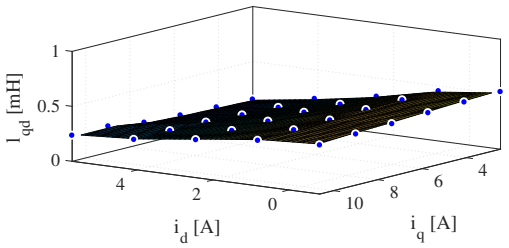

(c) l_{qd} (constant speed)

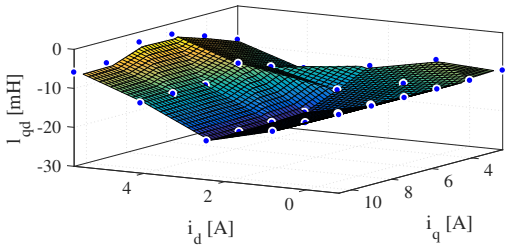

(d) l_{qd} (locked rotor)

Figure 4.12: Constant speed and locked rotor incremental inductances (continuation).

4.2 Simulation Environment and Motor Control

The simulations are made in MATLAB/Simulink and the S-function is used for the implementation of the machine model. It is suitable for implementing the state-space equations of the SPMSM in Simulink, which are derived in Appendix A.

The machine is controlled using a cascaded control system with a current controller in the inner loop, and a speed controller in the outer loop as seen in Figure 4.13. The machine in the continuous simulations is directly fed with the continuous three-phase reference voltage (although it cannot reach above $\frac{U_{dc}}{\sqrt{3}}$ since this is the maximum phase voltage) while for the discrete simulations, a pulse-width modulated three-phase inverter was modelled as the voltage source. The position θ_r, found in Figure 4.13, is obtained through an estimation strategy (discussed in later chapters). The following sections briefly describe the control system used in the simulations and the model verifications made.

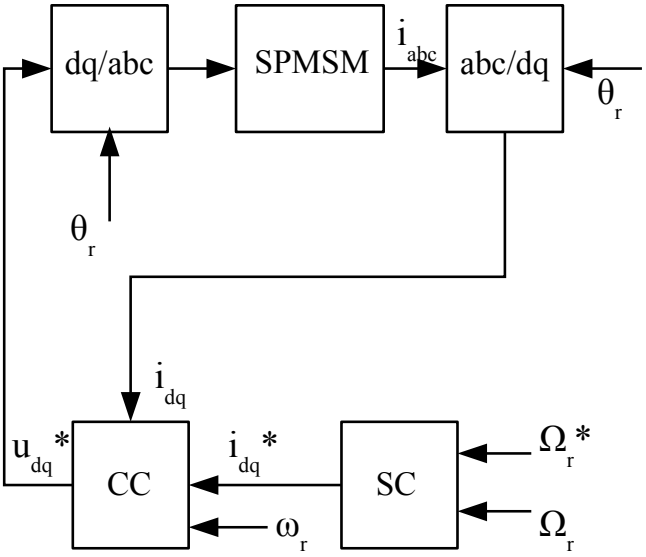

Figure 4.13: An overview of the continuous control scheme showing the machine being controlled by a cascaded current and speed controller. The position estimation is kept general for now. CC and SC stands for current and speed controller respectively.

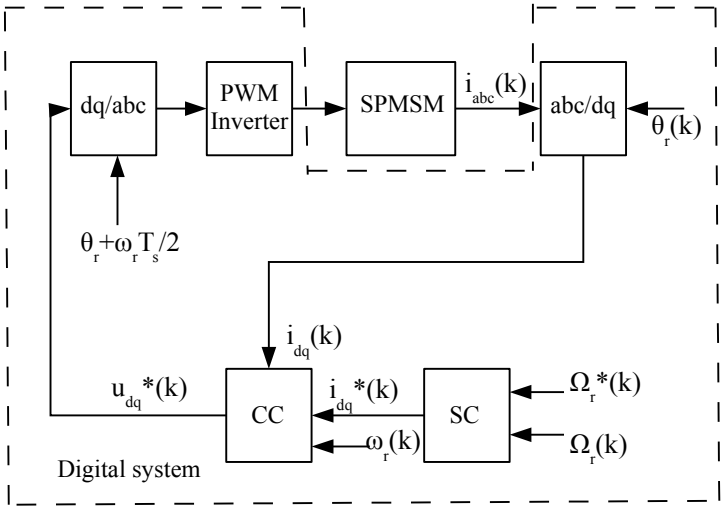

Figure 4.14: An overview of the discrete control scheme showing the machine being controlled by a cascaded current and speed controller.

The discrete setup is similar to the continuous setup in Figure 4.13. The differences are that the control system is discretized and the input signals to it are sampled. The sampling frequency is set to 20 kHz which gives a sampling time of 50 µs. Further, as will be discussed shortly, the voltage supply is a model of a three-phase pulse-width

modulated inverter having a DC-bus voltage of 750 V. Also, the injection angle has to be compensated due to the sampling delay and possible rotation of the machine, as visualized in Figure 4.14.

4.2.1 Cascade Current and Speed Control

The machine is controlled using a cascade speed and current controller structure as can be seen in e.g. Figure 4.13. The current controller is derived in the dq-frame and consists of two separate PI controllers, one for the d-axis and one for the q-axis. Further, the current controllers compensates for back-emf and utilize active damping to be more robust against disturbances [4]. By adding a fictitious resistance, R_{ad} for the d-axis or R_{aq} for the q-axis, to the machine model, used to derive the current controller, active damping is introduced. The current controllers are visualized in Figure 4.15 and Figure 4.16 where the back-emf compensation and active damping can be seen. Further, output voltage limitation and anti-windup [4] are implemented as well in order to keep the machine from overmodulation. Also in Table 4.4, the controller parameters are shown. The current controller was derived using a simplified dq-model of the machine, neglecting saturation and cross-coupled inductances (i.e. $l_{dq} = l_{qd} = 0$, and static l_{dd} and l_{qq})

$$\begin{aligned} u_d &= R_s \cdot i_d + l_{dd}\frac{di_d}{dt} - \omega_r \cdot L_q \cdot i_q \\ u_q &= R_s \cdot i_q + l_{qq}\frac{di_q}{dt} + \omega_r \cdot (L_d \cdot i_d + \lambda_{PM}). \end{aligned} \tag{4.7}$$

The current controller was derived using IMC as in [4] and the active damping terms were chosen so that the controlled system would have the same bandwidth as the closed-loop system [4].

Table 4.4: Current controller parameters (α_{cc} is the controller bandwidth)

	d-axis	q-axis
Active damping	$R_{ad} = \alpha_{cc} \cdot \widehat{l}_{dd} - \widehat{R}_s$	$R_{aq} = \alpha_{cc} \cdot \widehat{l}_{qq} - \widehat{R}_s$
Proportional gain	$K_{pcd} = \alpha_{cc} \cdot \widehat{l}_{dd}$	$K_{pcq} = \alpha_{cc} \cdot \widehat{l}_{qq}$
Integral gain	$K_{icd} = \alpha_{cc} \cdot (\widehat{R}_s + R_{ad})$	$K_{icq} = \alpha_{cc} \cdot (\widehat{R}_s + R_{aq})$

The speed controller was derived assuming that the current controller is much faster than the speed controller. The mechanical model (2.16), was used in the derivation of the speed controller. It was further assumed that the load torque was constant. Using IMC, the speed controller was derived and is seen in Figure 4.17, the parameters are described in Table 4.5 where $\widehat{J}$ is the estimated inertia. Active damping, B_a, is implemented to make the closed-loop system more robust and anti-windup is also implemented due to limitations in torque. The limitations in torque are affected by the current limit, the current must not become higher than the nominal current in order to protect the machine.

The output of the current controller is the reference voltage in the estimated dq-frame while the output of the speed controller is the reference torque. The

conversion between reference torque and reference current (as input to the current controllers) is simple for a surface mounted permanent magnet machine. The d-current reference component (as long as the machine is not to be driven in high speeds) could be set to zero while the q-current reference is easily calculated from the torque reference. However, in order to set the d-current component automatically, a field-weakening system has been used [4]. Since the speeds in this project are low, this is an unnecessary feature, but it was put there to make the control system dynamic and automatic. The q-current component is calculated using the usual torque-current relation but it is limited such that the total reference current is less than or equal to the rated current as a protective measure. With the limited q-current, the limited torque reference, seen in Figure 4.17, is determined and used in an anti-windup structure in the speed controller.

Table 4.5: Speed controller parameters (α_{sc} is the controller bandwidth)

Parameter	Equation
Active damping	$B_a = \alpha_{sc} \cdot \widehat{J}$
Proportional gain	$K_{p\omega} = \alpha_{sc} \cdot \widehat{J}$
Integral gain	$K_{i\omega} = \alpha_{sc} \cdot B_a$

The discretized controller are modified versions of the continuous controllers, approximating the integrators using the Forward Euler approximation

$$\begin{aligned} \frac{dx}{dt} &\approx \frac{x_{k+1} - x_k}{T_{samp}} \\ I_k &= I_{k+1} - T_{samp} \cdot e_k \end{aligned} \tag{4.8}$$

where k stands for the current sample and T_{samp} is the sampling time used. I_k is the integrated error for sample k, I_{k+1} is the integrated error for sample $k+1$ and e_k stands for the error signal (which is integrated) at sample k. Using (4.8), the following discretized (and final) controller structures are shown in Figure 4.15, Figure 4.16 and Figure 4.17.

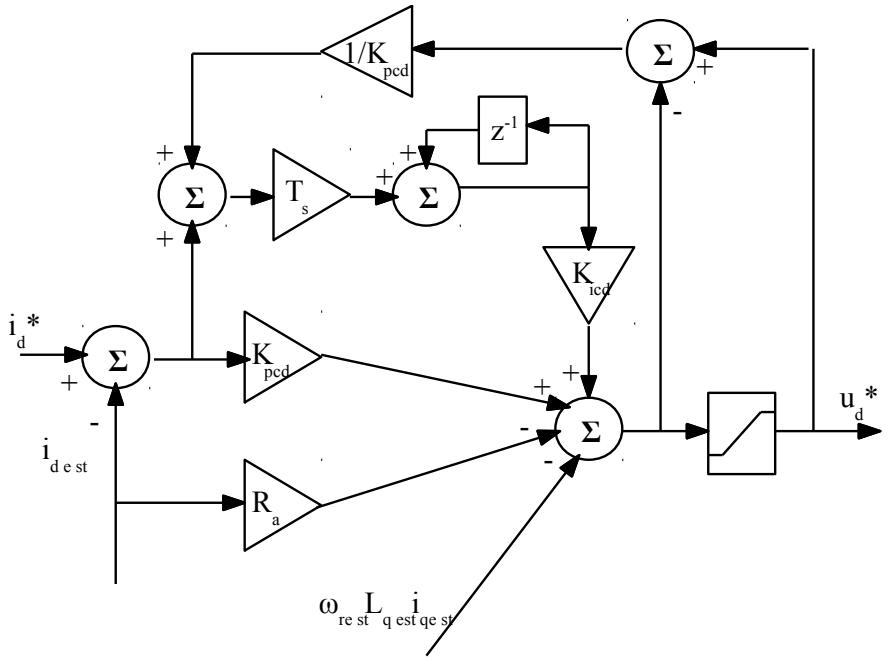

Figure 4.15: Current controller (d-component) in the estimated dq-frame.

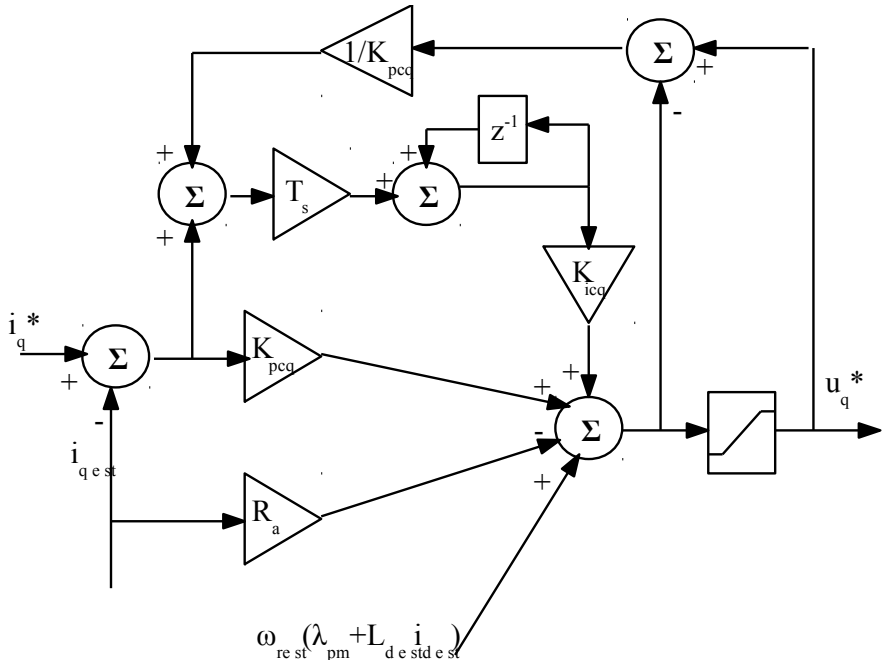

Figure 4.16: Current controller (q-component) in the estimated dq-frame.

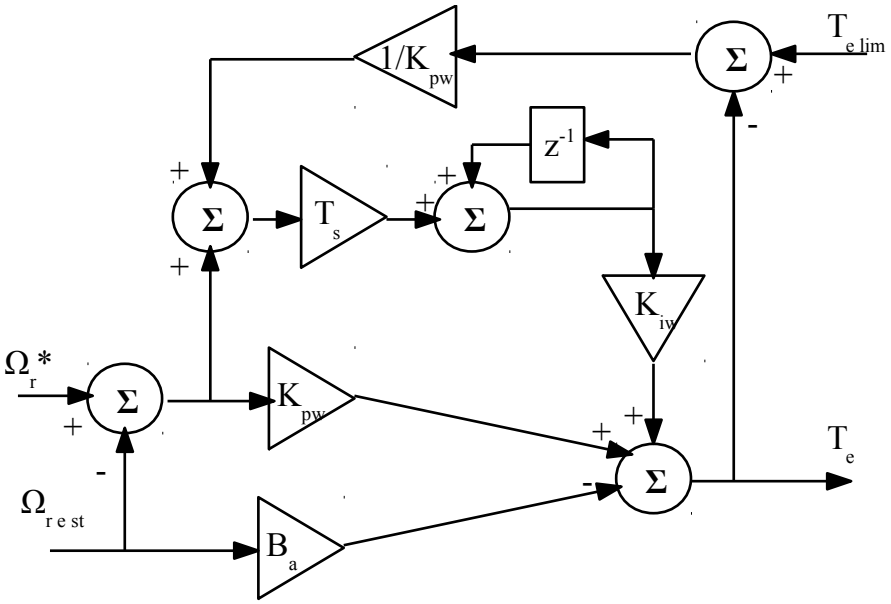

Figure 4.17: Speed controller.

4.2.2 Discrete Filters

For the chosen estimation techniques there is a need for different discrete filters. It is possible to convert the transfer function of an analog filter in the Laplace domain to a discrete filter transfer function in the Z-domain using bilinear transform. With bilinear transform, a continuous filter in the s-domain can be rewritten as a discrete filter in the z-domain by substituting s with $\frac{z-1}{z+1}$.

The cutoff frequency in the discrete filter is used to determine the continuous filter frequency. Then, the continuous filter is transformed using $s = \frac{z-1}{z+1}$. The continuous frequency relates to the desired discrete frequency as $\omega_c = tan(\frac{\omega_d}{2})$, where ω_c is the resulting continuous frequency and $\omega_d = 2\pi\frac{f}{f_s}$ is the discrete desired frequency, f, normalized against the sampling frequency.

In the upcoming methods bandpass filters and notch filters are going to be used. The bandpass filter is seen in Figure 4.18 and the coefficients A, B, C and D are written as

$$\begin{aligned} A =& \alpha(\omega_u - \omega_l) \\ B =& \alpha + \alpha\omega_u\omega_l + A \\ C =& 2\alpha\omega_u\omega_l - 2\alpha \\ D =& \alpha + \alpha\omega_u\omega_l - A. \end{aligned} \tag{4.9}$$

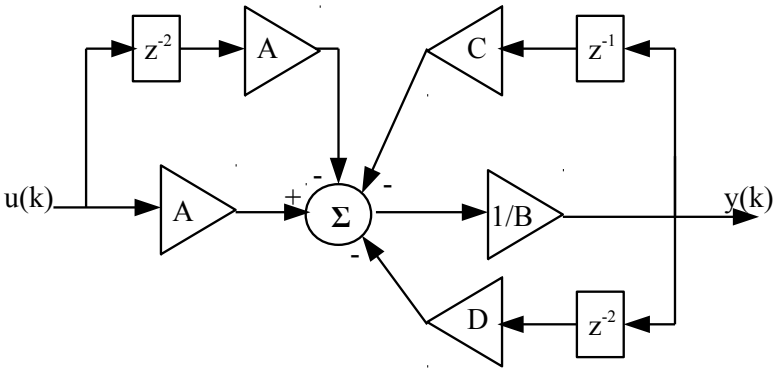

Figure 4.18: A discretized bandpass filter structure used in the thesis.

where α is the frequency which is desired to pass through the filter and ω_u and ω_l are the upper and lower frequencies, respectively, of the band. The notch filter structure used can be seen in Figure 4.19 where the coefficients are

$$\begin{aligned} A_2 =& 1 + \beta^2 \\ B_2 =& 2\beta^2 - 2 \\ C_2 =& 1 + 2\zeta\beta + \beta^2 \\ D_2 =& 1 - 2\zeta\beta + \beta^2. \end{aligned} \tag{4.10}$$

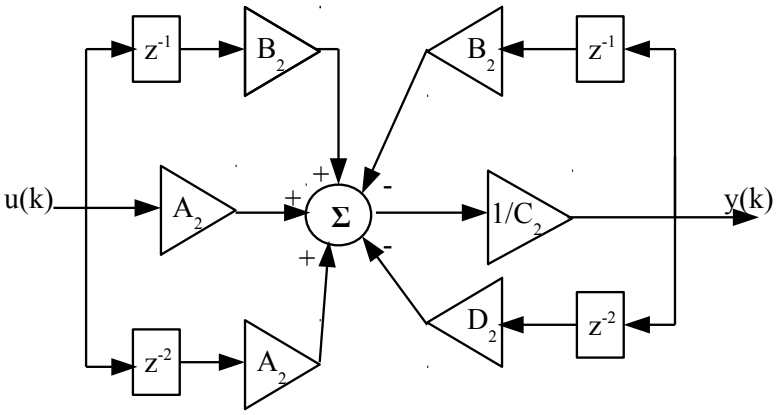

Figure 4.19: A discretized notch filter structure used in the thesis. See [51] for a continuous transfer function.

In (4.10), β represents the natural frequency of the filter, $\zeta = 1$ is the damping factor. The filters were analysed and tuned through analyses of the continuous filters in MATLAB and through simpler simulations in Simulink.

4.2.3 Implementation of Varying Inductances

The inductances were implemented using a surface-fit function in MATLAB called *fit*. It fits a surface for the specified measurement points using a specified interpola-

tion method. The result can be used as a function to calculate the value of the fitted surface, within the measurement span, for an arbitrary point. Using a command, *feval*, which takes the name of the surface object, the function can be reached within the S-function (the object name is passed to the S-function as a parameter) and can thus be evaluated at the specified point ($i_{d,s}$,$i_{q,s}$).

It would have been better to use a simple lookup table with linear interpolation for the implementation of the inductances but due to difficulties encountered in incorporating this for the S-function, the surface-fit procedure explained above had to be used. Linear interpolation was first used, as seen in Figures 4.10 to 4.12, but these also induced difficulties when trying to run the simulations. Therefore, the biharmonic interpolation option had to be used, see Figure 4.20 where the measurement data is seen as blue dots. This resulted in errors in the surface fit, as seen for the worst case (for constant speed-measured l_{qq}) in Figure 4.20b. The error is just above 0.1 mH in the corners which seems small but still gives some model errors which could affect the results in the end.

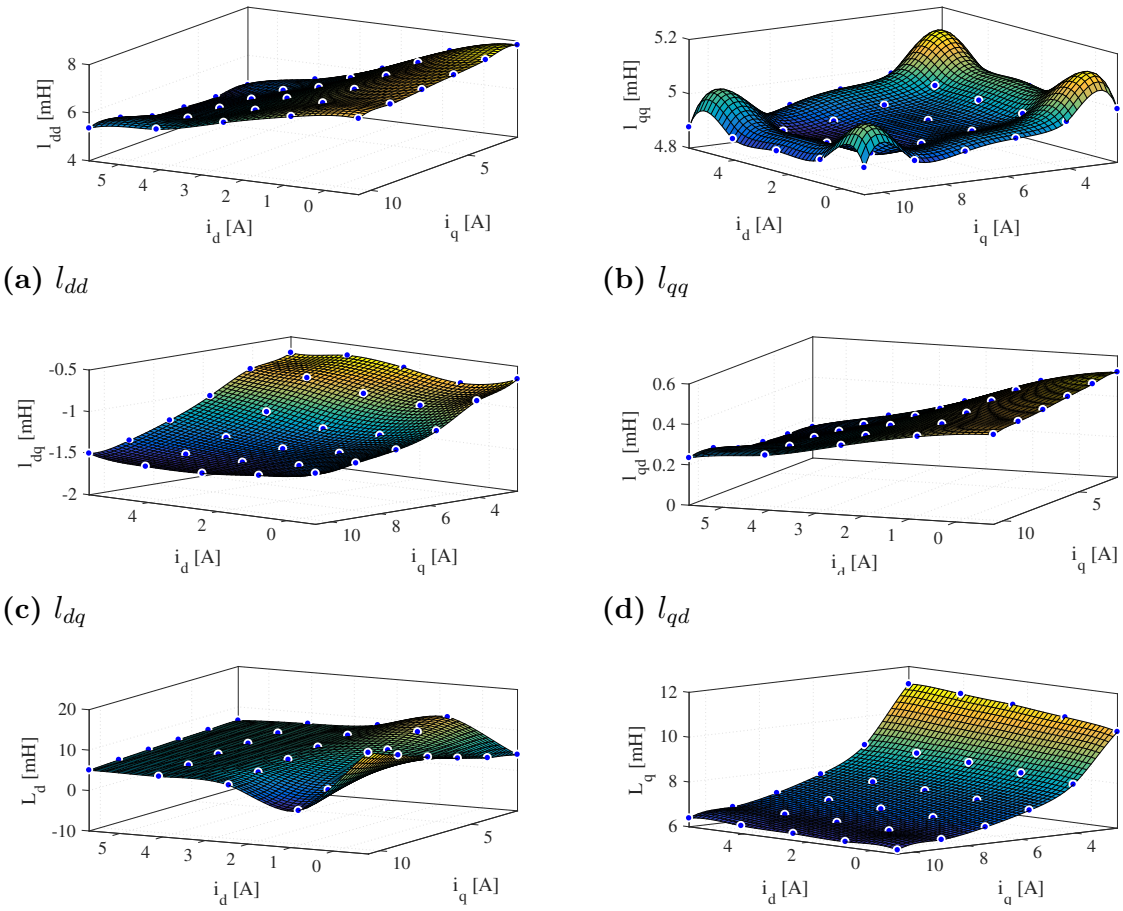

(a) l_{dd} **(b)** l_{qq}

(c) l_{dq} **(d)** l_{qd}

(e) L_d **(f)** L_q

Figure 4.20: Constant speed inductances fitted with biharmonic interpolation.

4.2.4 Model Verification

Using the nonlinear machine model in the dq-frame (2.13) derived in Section 2.2.2 and the inductances modelled in Section 4.2.3, the same procedure was implemented as was used in the real flux measurements, i.e. the current reference steps and the rotor conditions (locked or constant speed). Both the constant speed and locked rotor results are used here to further give a comparison between them. The simulations were slow, therefore, only the first step was simulated. The real measurements are seen together with the simulation results in Figure 4.21 and Figure 4.22 respectively.

The constant speed simulation was done in the following way. The load torque was altered to fit the simulation case, i.e. a viscous damping load torque dependent on speed was added ($B = 0.0014$ Nm/rad/s was given at the company) and the friction model, developed earlier, was removed

$$T_L = B\Omega_r + T_{L,extra}. \tag{4.11}$$

The machine was also set so that it could not accelerate or decelerate (i.e. having a constant speed). The speed controller was removed while current reference values were put to the current controller at different time points, as was done in the measurement. The inductances and resistance used in the current controller was set to 5 mH and 1 Ω, thus having a slight parameter error. This was the case in the real measurement as well. Further, the moment of inertia was set to $J = 0.0002$ kgm^2 and the initial speed was set to 4000 rpm. In both the measurement and the simulation the DC-bus voltage was set to 750 V.

The locked-rotor simulation case was done in a similar way, the only differences were a lower DC-bus voltage (200 V) to minimize the effects of having no dead-time compensation, and no initial speed. For both simulations, the real signals were used in the control system, i.e. the speed, the rotor angle and the dq-current were assumed to be perfectly known.

Due to the measurement, the first transient of the constant speed measurements is not good to compare with the simulations since it looked like the machine had not achieved the correct speed yet. In the measurement, the test procedure was automatic so that it restarted with the first current combination after the last combination was done. Therefore, as the measurement restarted after the last current combination, the first combination can be seen again in Figure 4.21a and Figure 4.21b. Hence, in the constant speed simulation, the currents were first stepped to $i_d = i_q = 7.4$ A, which is the last measurement combination. Then, at 0.1 s, the currents were stepped to $i_d = -0.81$ A and $i_q = 2.4$ A as was done in the real measurement. Comparing Figure 4.21a with Figure 4.21c, the transients differ, where v_d from the simulations reaches a minimum of -433 V while the actual v_d from the measurement reaches -467 V. However, the steady-state are quite similar as v_d in the simulation stays at -52 V and v_d from the measurement goes to -52.6 V. The current i_d goes towards -0.81 A in both the simulations and the measurement as it should. Further, comparing Figure 4.21b with Figure 4.21d, the transients differ here as well. In the measurement v_q reaches about 59 V and goes towards a mean of 215 V while in the simulations v_q reaches about 10.3 V and goes towards 226.8 V. Hence, there is a difference of almost 12 V during steady-state. There is some

voltage drop in the cable connecting the machine with the controllers in the real measurements that has not been taken into account for in the simulations. Also, the steady-state voltage is mainly dependent on the back-emf for such high speeds (4000 rpm). According to (2.13), the absolute inductance and the estimated rotor flux make up the speed-dependent parts of the machine model. The estimated rotor flux is quite close to the theoretical value so some of the difference could be due to the estimated absolute inductance. This might explain why there is a difference in the steady-state voltages for the q-axis but not as much for the d-axis. However, the q-currents in both the simulation and the measurement reaches 2.4 A at steady-state as it should. The differences during the transients might be due to the differences in the current controller settings.

In Figure 4.22a and Figure 4.22c, the d-axis voltage and current can be seen from the measurement and the simulation for the locked rotor case. The d-axis voltage reaches a minimum of -36.9 V in the simulation while it reaches -45.4 V in the measurement, almost 10 V difference. Further, the shape of the voltage during the transient suggests that there might be some difference in the control system between the measurements and the simulations. Together with inductance estimation errors, this could be the reason behind the differences during the transient. However, the steady-state d-axis voltage is -0.85 V in the simulations while it goes to -2.45 V in the measurement. The difference in steady-state for zero-speed is most likely due to resistance errors, e.g. the neglected cable resistance, yielding a need for more voltage to reach a certain current reference in reality. The current i_d in both the measurement and the simulation reaches its reference of about -0.8 A. Comparing the q-axis voltage and current in Figures 4.22b and 4.22d, the current reaches its steady-state reference of 2.4 A in both the simulation and the measurement. However, the voltage transients look different here as it also did for the d-axis voltage. In the simulation, the v_q reaches a steady-state of 2.52 V while in the measurement it needs 5.3 V. As stated before, this could be due to the cable resistance. It is seen that the simulations do not follow the real measurements closely. There are some overshoots in the simulations and, especially for v_q, the transient magnitude differs. This might be due to measurement errors or post processing errors, e.g. the inductance identification method or the surface-fit procedure. Further, other error sources might be acting as well, e.g. the neglected cable resistance and possible small rotor movements for certain current combination transients. Also, as was stated for the constant speed case, the settings of the current controllers are probably affecting the transients.

Comparing the results of the model verification of the locked rotor case and the constant speed case, the simulated constant speed case seemed to reach the measurement better than the locked rotor case. However, there might have been some differences in the control system that could have affected the results and the cable between the machine and the controllers in the real measurements was not taken into consideration when conducting the simulations. Hence, there is a voltage drop over this cable that has not been accounted for. Although the dip in L_d for the constant speed measurement, also taking into consideration what is said in Section 4.1.2.4 (constant speed measurement had less sources of measurement errors) and Section 4.1.3 (the strange behaviour of some locked rotor inductances, e.g. l_{qq}), and

the results from the model verification, the inductances derived from the constant speed measurements are to be used in the following simulations.

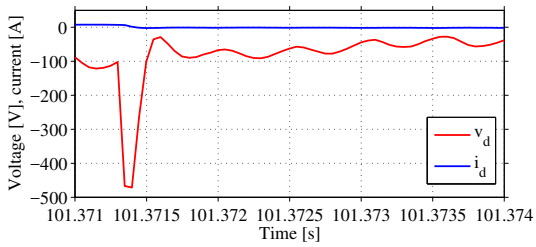

(a) $v_{d,s}$, $i_{d,s}$ (measurement)

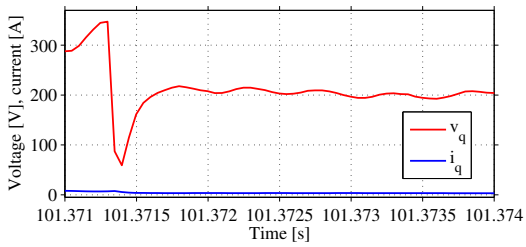

(b) $v_{q,s}$, $i_{q,s}$ (measurement)

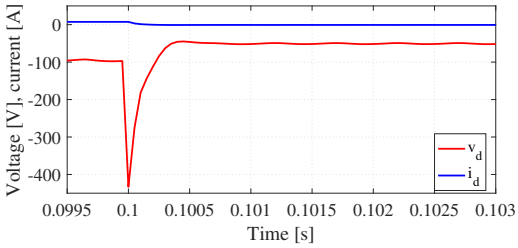

(c) $v_{d,s}$, $i_{d,s}$ (simulation)

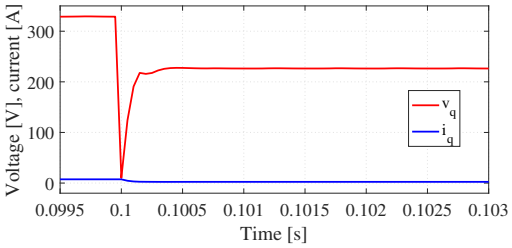

(d) $v_{q,s}$, $i_{q,s}$ (simulation)

Figure 4.21: Constant speed case, steady-state, combination $i_{d,s} = -0.81$ A, $i_{q,s} = 2.4$ A.

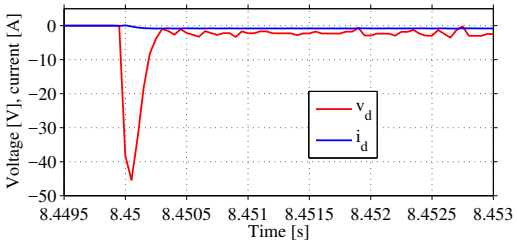

(a) $v_{d,s}$, $i_{d,s}$ (measurement)

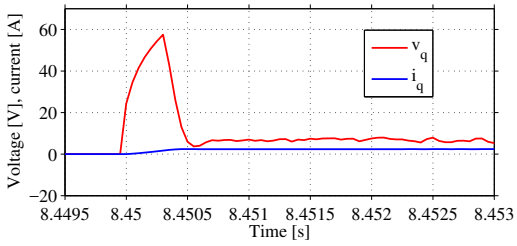

(b) $v_{q,s}$, $i_{q,s}$ (measurement)

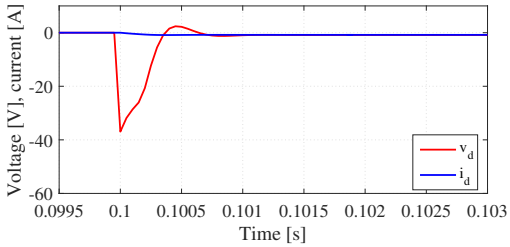

(c) $v_{d,s}$, $i_{d,s}$ (simulation)

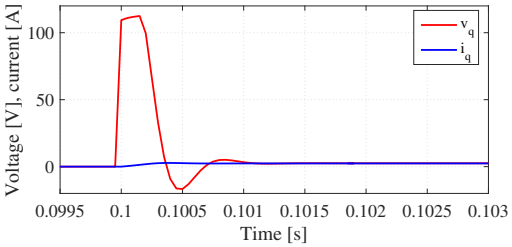

(d) $v_{q,s}$, $i_{q,s}$ (simulation)

Figure 4.22: Locked rotor case, transient, combination $i_{d,s} = -0.81$ A, $i_{q,s} = 2.4$ A.

5

Position Estimation during Standstill and Low Speeds

As has been discussed in Chapter 3, a high frequency pulsating voltage injection scheme is to be investigated based on [24]. For initial position estimation, a simpler method is also investigated based on injecting voltage square pulses in the stationary frame. This chapter contains the main ideas of the methods and should serve as a reference for the background theory of the methods in this project.

5.1 High Frequency Signal Injection

The method described in [24] is based on high frequency pulsating signal injection into the estimated dq-frame. The equations in [24] are simplified and does not take cross-coupled inductances into account. Hence, starting from the machine model in (2.12), and assuming that the rotational speed is low and that the resistive voltage drop both are small compared to the high frequency current derivative, the following simplified model can be used as a starting point

$$\underline{u}_s^{dq} \approx \begin{bmatrix} l_{dd} & l_{dq} \\ l_{qd} & l_{qq} \end{bmatrix} \frac{d\underline{i}_s^{dq}}{dt} = \underline{l} \frac{d\underline{i}_s^{dq}}{dt} \tag{5.1}$$

where $\underline{l}$ denotes a 2-by-2 matrix with the dynamic inductances as elements. The goal is to find out what the current response due to a high frequency voltage looks like for the chosen machine model. The pulsating voltage is injected in the estimated dq-frame. Hence, in order to find the current response, the voltage needs to be transformed into the real dq-frame, as seen above in (5.1). Writing the injected high frequency voltage in the estimated frame as

$$\underline{\widehat{u}}_s^{dq} = V_{HF} \begin{bmatrix} cos(w_{HF}t) \\ 0 \end{bmatrix} \tag{5.2}$$

where V_{HF} is the injected voltage amplitude and ω_{HF} is the injected signal angular frequency, and using the transformation matrix found in (2.4) with the angle difference between the real dq-frame and the estimated dq-frame as the transformation angle $\theta_e = (\theta_r - \widehat{\theta}_r)$, the dq-voltage is found as

$$\begin{aligned}\underline{u}_s^{dq} =& V_{HF}\begin{bmatrix} cos(\theta_e) & sin(\theta_e) \\ -sin(\theta_e) & cos(\theta_e) \end{bmatrix}\begin{bmatrix} cos(w_{HF}t) \\ 0 \end{bmatrix} = \\ =& V_{HF}cos(w_{HF}t)\begin{bmatrix} cos(\theta_e) \\ -sin(\theta_e) \end{bmatrix}\end{aligned} \tag{5.3}$$

If the voltage in (5.3) is injected into the machine model in (5.1), the current response is found by inverting $\underline{l}$ and integrating both sides, as

$$\begin{aligned}\underline{i}_s^{dq} =& \int \underline{l}^{-1}\underline{u}_s^{dq}dt = \\ =& \frac{V_{HF}}{l_{dd}l_{qq} - l_{dq}l_{qd}}\begin{bmatrix} l_{qq} & -l_{dq} \\ -l_{qd} & l_{dd} \end{bmatrix}\int cos(w_{HF}t)\begin{bmatrix} cos(\theta_e) \\ -sin(\theta_e) \end{bmatrix}dt.\end{aligned} \tag{5.4}$$

Furthermore, assume that the injected frequency ω_{HF} is much higher than the frequency difference between the real dq-frame and the estimated dq-frame. Then (5.4), can be developed further

$$\begin{aligned}\underline{i}_s^{dq} =& \frac{V_{HF}}{l_{dd}l_{qq} - l_{dq}l_{qd}}\begin{bmatrix} l_{qq} & -l_{dq} \\ -l_{qd} & l_{dd} \end{bmatrix}\begin{bmatrix} cos(\theta_e) \\ -sin(\theta_e) \end{bmatrix}\int cos(w_{HF}t)dt = \\ =& \frac{1}{\omega_{HF}}\frac{V_{HF}}{l_{dd}l_{qq} - l_{dq}l_{qd}}\begin{bmatrix} l_{qq} & -l_{dq} \\ -l_{qd} & l_{dd} \end{bmatrix}\begin{bmatrix} cos(\theta_e) \\ -sin(\theta_e) \end{bmatrix}sin(w_{HF}t) = \\ =& \frac{V_{HF}sin(\omega_{HF}t)}{\omega_{HF}(l_{dd}l_{qq} - l_{dq}l_{qd})}\begin{bmatrix} l_{qq}cos(\theta_e) + l_{dq}sin(\theta_e) \\ -l_{qd}cos(\theta_e) - l_{dd}sin(\theta_e) \end{bmatrix}.\end{aligned} \tag{5.5}$$

Eq. (5.5) shows the current response due to a voltage input into an estimated dq-frame. Depending on the estimation error angle and the cross-coupled inductances, the current response has a d- and a q-component. Usually, the cross-coupled inductances are neglected but this cannot be done for the chosen machine model. However, the real dq-current cannot be measured. The estimated dq-current is used in [24] to estimate the rotor position and speed. Therefore, (5.5) should be transformed into the estimated dq-frame, having the same transformation angle as before, using (2.3). This current can be measured since the three-phase current is easily transformed into the estimated dq-frame using the estimated rotor position. The current response in the estimated dq-frame is thus

$$\begin{aligned}\hat{\underline{i}}_s^{dq} =& A\begin{bmatrix} cos(\theta_e) & -sin(\theta_e) \\ sin(\theta_e) & cos(\theta_e) \end{bmatrix}\begin{bmatrix} l_{qq}cos(\theta_e) + l_{dq}sin(\theta_e) \\ -l_{qd}cos(\theta_e) - l_{dd}sin(\theta_e) \end{bmatrix} = \\ =& \frac{A}{2}\begin{bmatrix} (l_{qq} - l_{dd})cos(2\theta_e) + (l_{dq} + l_{qd})sin(2\theta_e) + (l_{qq} + l_{dd}) \\ -(l_{dq} + l_{qd})cos(2\theta_e) + (l_{qq} - l_{dd})sin(2\theta_e) - (l_{qd} - l_{dq}) \end{bmatrix}\end{aligned} \tag{5.6}$$

where $A = \frac{V_{HF} sin(\omega_{HF} t)}{\omega_{HF}(l_{dd} l_{qq} - l_{dq} l_{qd})}$. These equations are only valid using (2.12) as the machine model, the injected frequency has to be much higher than the difference between the frequencies of the real and estimated dq-frames and that the same transformation angle is used for all transformations between the real and estimated dq-frames.

5.1.1 Signal Processing - Obtaining an Error Signal

Following the same procedure as in [24] the estimated high frequency q-component of the current response is demodulated and low-pass filtered in order to obtain an error signal which can be used to estimate the rotor position and speed. This section reveals the details for the application of this procedure for the chosen machine model. A difference from [24] is that, because of the cross-coupled inductances, a compensation has to be made to the error signal in order to cancel a DC-offset which could affect the estimation process later on.

Continuing from (5.6) and assuming that the error angle is small, $cos(\theta_e) \approx 1$ and keeping $sin(\theta_e)$ as it is, (5.6) can be simplified as

$$\begin{aligned} \hat{\underline{i}}_s^{dq} =& \frac{A}{2} \begin{bmatrix} (l_{qq} - l_{dd})cos(2\theta_e) + (l_{dq} + l_{qd})sin(2\theta_e) + (l_{qq} + l_{dd}) \\ -(l_{dq} + l_{qd})cos(2\theta_e) + (l_{qq} - l_{dd})sin(2\theta_e) - (l_{qd} - l_{dq}) \end{bmatrix} \approx \\ \approx& \frac{A}{2} \begin{bmatrix} 2l_{qq} + (l_{dq} + l_{qd})sin(2\theta_e) \\ -2l_{qd} + (l_{qq} - l_{dd})sin(2\theta_e) \end{bmatrix} \end{aligned} \tag{5.7}$$

According to (5.7), both components of the estimated dq-current response could be used for estimating the rotor position. Usually, as been said before, the cross-coupled inductances are assumed to be equal and zero. Therefore, the q-component is often used, as e.g. in [24]. It is important to remember that (5.7) is only valid if the above mentioned assumptions can be made. Hence, the position estimation error needs to be kept small.

In [24], the estimated q-current component is passed through a band-pass filter to retrieve the high frequency component having the angular frequency ω_{HF}. The band-pass filter is in this project designed as

$$H(s)_{BPF} = \frac{(\omega_2 - \omega_1)s}{s^2 + (\omega_2 - \omega_1)s + \omega_{HF}^2} \tag{5.8}$$

where it was chosen that $\omega_1 = 0.9 \cdot \omega_{HF}$ and $\omega_2 = 1.1 \cdot \omega_{HF}$ which also determine the bandwidth of the frequency spectrum which is let through the filter. The resulting high frequency q-component current is going to be (5.7) if the filter works properly. Then, the current q-component is demodulated. In this case, the demodulation process consists of multiplying the q-current high frequency component with $-sin(\omega_{HF} t)$, resulting in the demodulated current

$$\begin{aligned} \hat{i}_{qs,demod} =& \frac{A}{2}(-2l_{qd} + (l_{qq} - l_{dd})sin(2\theta_e))(-sin(\omega_{HF} t)) = \\ =& \frac{V_{HF}(1 - cos(2\omega_{HF} t))}{4\omega_{HF}(l_{dd} l_{qq} - l_{dq} l_{qd})}(2l_{qd} + (l_{dd} - l_{qq})sin(2\theta_e)). \end{aligned} \tag{5.9}$$

As can be seen this results in a DC component and a higher frequency component, oscillating with the angular frequency $2\omega_{HF}$. In [24], this high frequency component is filtered out using a low-pass filter. In this project, the low-pass filter is replaced by a notch filter (see Figure 4.19 for a discrete implementation of one, also see [51] for a continuous transfer function). This filter stops the higher frequency component but lets through most of the rest of the signal. The reason why this filter was chosen instead of a lowpass filter is due to the high damping of the specific frequency which is stopped. For the first order lowpass filter, this damping is less. Also, since the bandpass filter will let through only the spectrum close to the injected frequency, a notch filter is safe to use since the only frequency components will be the one with twice the injected frequency and a DC component. The resulting filtered current signal is

$$\widehat{i}_{qs,err} = \frac{V_{HF}}{4\omega_{HF}(l_{dd}l_{qq} - l_{dq}l_{qd})}(2l_{qd} + (l_{dd} - l_{qq})sin(2\theta_e)). \tag{5.10}$$

As can be seen, there is an offset and a sinusoidal signal dependent on the angle error estimation. In order to estimate the rotor position, the sinusoidal part is to be sent to a PI controller, see next subsection, but if the entire signal in (5.10) is sent to a PI controller the integrator will always see a constant error due to the offset dependent on l_{qd}. Hence, this part has to be subtracted from the signal. In reality, an estimation has to be done, e.g. using a lookup table. In the simulation made here, however, the inductances are known which makes it easier to remove this offset. So, if subtracting an estimated offset $\frac{V_{HF}\widehat{l}_{qd}}{2\omega_{HF}(\widehat{l}_{dd}\widehat{l}_{qq} - \widehat{l}_{dq}\widehat{l}_{qd})}$ from (5.10), the resultant current signal, which should be treated as an error signal for the position estimation PI controller, becomes

$$\begin{aligned}\widehat{i}_{qs,err} =& \frac{V_{HF}l_{qd}}{2\omega_{HF}(l_{dd}l_{qq} - l_{dq}l_{qd})} + \frac{V_{HF}(l_{dd} - l_{qq})sin(2\theta_e)}{4\omega_{HF}(l_{dd}l_{qq} - l_{dq}l_{qd})} - ... \\ ...& - \frac{V_{HF}\widehat{l}_{qd}}{2\omega_{HF}(\widehat{l}_{dd}\widehat{l}_{qq} - \widehat{l}_{dq}\widehat{l}_{qd})} \approx \frac{V_{HF}(l_{dd} - l_{qq})sin(2\theta_e)}{4\omega_{HF}(l_{dd}l_{qq} - l_{dq}l_{qd})}.\end{aligned} \tag{5.11}$$

As a last conclusion, the measured current in the estimated dq-frame is also notch filtered before it is sent back to the current controllers. The reason is that the high frequency component of the machine current should not be fed back to the control system. In [24], this was done with a lowpass filter. The stopped frequency is the injected frequency.

5.1.2 Position and Speed Estimation

The approach for estimating the speed and the position in [24] is to use the result of (5.11) and control it to zero. Since the sine function goes to zero at either 0 degrees or 180 degrees, this means that there might be an error of 180 degrees when controlling the angle error to zero. This is to be taken care of later using a method that determines where the north pole is aligned. Meanwhile, in [24], it is assumed that the error angle is small, thus $sin(2\theta_e) \approx 2\theta_e$. This gives approximately

$$\hat{i}_{qs,err} \approx \frac{V_{HF}(l_{dd} - l_{qq})}{2\omega_{HF}(l_{dd}l_{qq} - l_{dq}l_{qd})}\theta_e = A_e\theta_e. \tag{5.12}$$

which is sent to a PI controller where it is regarded as a position error signal. Here it is seen that the error signal is dependent on the incremental inductances, especially the difference between l_{dd} and l_{qq}. This difference is visualized in Figure 5.1 considering the inductances from the constant speed measurement.

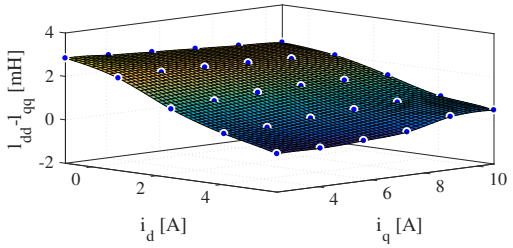

Figure 5.1: $l_{dd} - l_{qq}$ from the constant speed measurement.

For high d-currents and low q-currents there is a possibility that the difference changes sign as it becomes negative. This would introduce a negative error to the PI controller. Hence, even though the angle error might be positive, it is seen as negative, i.e. the actual angle seems to be less than the estimated angle. The PI controller will then try to lower the estimated angle even though it might be less than the actual angle already. For slightly less d-current the difference goes towards zero. However, since the PMSM is rarely driven with high d-currents these problems are seen as unlikely to happen, unless something else makes the control system to become unstable and the control of the currents is lost.

The PI controller is of the form $F(s) = K_p + \frac{1}{s}K_i$. The output of the PI controller is the estimated rotor speed and a simple integrator can be used to get the estimated rotor position [24]. From early simulations, it became apparent that the estimated rotor speed has less ripple if it is obtained from the integrator part of the PI controller instead of the output of the controller. It is believed that the ripple from the input signal propagates through the proportional part. However, the output of the PI controller is sent to an integrator which gives the estimated position. The closed loop transfer function in [24] can be determined as

$$\frac{\hat{\theta}_r}{\theta_r} = \frac{sK_pA_e + K_iA_e}{s^2 + sK_pA_e + K_iA_e} \tag{5.13}$$

assuming that the approximation in (5.12) holds. This transfer function is used to calculate the gain parameters K_p and K_i of the PI controller in order to achieve a certain bandwidth (α_{PI}) and stability.

In order to ensure a stable closed-loop system, Routh's algorithm can be applied to see how the control parameters should relate to each other. The resulting conditions for a stable system using Routh's algorithm is determined to be $A_eK_p > 0$ and $A_eK_i > 0$. Hence, the amplitude of the error signal, A_e is important to take

into account. For complex conjugated poles at $-\frac{\alpha_{PI}}{\sqrt{2}} \pm j\frac{\alpha_{PI}}{\sqrt{2}}$ distance from origo in the complex plane, the control parameters are chosen as $K_p = \frac{\sqrt{2}\alpha_{PI}}{A_e}$ and $K_i = \frac{\alpha_{PI}^2}{A_e}$.

5.1.3 Bandwidth and Voltage Selection

In order to be able to use the PI controller to accurately estimate the rotor position and speed, the system giving the error signal needs to be faster than the PI controller such that the error signal always is accurate. The speed controller needs the correct speed input in order to function correctly. Therefore, the PI controller has to be much faster than the speed controller. Also, the input voltage changes with the estimated rotor position. Therefore, the PI controller is made slower than the electrical system in order to let the current response change correctly before making new estimations.

Also, it is important to remember the upper limits on the frequencies in the system due to the sampling constraint. The injected signal should have a frequency which is much lower than the sampling frequency in order to be sampled correctly. According to [4], the current controller bandwidth should be selected as less than (or equal to) a tenth of the sampling angular frequency. Further, in order to reduce the impact of the injected frequency in the control of the fundamental currents, the current controller bandwidth is selected as one tenth of the injected frequency. However, the estimated dq-current put to the current controller is to be notch filtered to remove this frequency component but to maintain some safety margin, the controller bandwidth is selected as $\alpha_{cc} = \frac{\omega_{HF}}{10}$. The speed controller bandwidth should be much less than the current controller bandwidth in order to make use of the control design (first order system approximation).

In order to achieve a stable estimation system, the following bandwidths were found from initial simulations

$$\begin{aligned} \alpha_{cc} &= \frac{\omega_{HF}}{10} \\ \alpha_{PI} &= \frac{\omega_{HF}}{40}. \\ \alpha_{sc} &= \frac{\alpha_{PI}}{7} \end{aligned} \tag{5.14}$$

where ω_{HF} is the angular frequency of the injected signal, α_{cc} is the current controller bandwidth, α_{PI} is the PI controller bandwidth and α_{sc} is the speed controller bandwidth.

5.1.4 Complete Estimation Setup

The setup of the estimation procedure described in the previous subsections is visualized in Figure 5.2. The current is processed using discrete filters and demodulation, as described previously, in order to obtain an error signal for the PI controller which estimates the rotor position and speed.

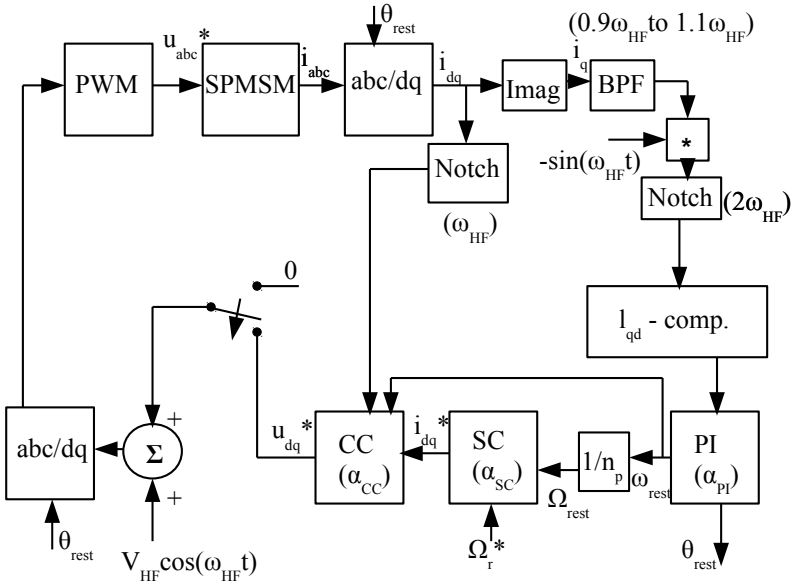

Figure 5.2: An overview of the estimation setup for the method described in [24] and above. n_p denotes the number of pole pairs.

As can be noticed in Figure 5.2, the machine (SPMSM) gets the input voltage from the inverter/PWM. The reference voltage is set in the current controller (CC) which gets its current reference from the speed controller/current reference calculation (SC). The injected voltage signal in (5.2) is added to the voltage reference in the estimated dq-frame after the CC if the machine is going to be started. The reference voltage from CC can also be chosen to be switched off (as visualized with a switch) in case initial position estimation is active. When running initial position estimation, the controllers are not used, only the high frequency signal is injected into the machine. That way, the machine remains at standstill during the initial position detection. The measured current is transformed into the estimated dq-frame and a notch filter removes the injected frequency component before the current is fed into the current controller. Further, the q-component of the current is also bandpass filtered (BPF) before it is processed as in (5.9) and a notch filter removes the frequency component with twice the injected frequency. The resulting signal is fed into the PI controller and the estimated position and speed is calculated before being used in the rest of the control system. The compensation of the l_{qd}-dependent term found in (5.11) is visualized as the l_{qd}-comp block in Figure 5.2 and it is made between the notch filter and the PI controller.

5.2 SCVM

For comparison purposes, the statically compensated voltage model (SCVM) is to be used in the simulations. The version of it used in this project is based on article [7]. However, instead of a speed dependent bandwidth of the lowpass filter, a constant bandwidth equal to the current controller bandwidth is used as was also done in [4]. Furthermore, another adjustment had to be made in order to be able to use it up

to 6000 rpm with relatively ordinary bandwidths, this is discussed below.

The estimator is based on the following equations (using the Forward Euler approximation of the derivative)

$$\begin{aligned}\widehat{\omega}_{r,k+1} =& \alpha \cdot T_{samp}\left(\frac{\widehat{e}_{q,k} - \lambda sign(\widehat{\omega}_{r,k})\widehat{e}_{d,k}}{\widehat{\lambda}_{PM}} - \widehat{\omega}_{r,k}\right) + \widehat{\omega}_{r,k} \\ \widehat{\theta}_{r,k+1} =& T_{samp}\widehat{\omega}_{r,k} + \widehat{\theta}_{r,k}.\end{aligned} \tag{5.15}$$

where k denotes the current sample, α is the bandwidth of a lowpass filter used to break an algebraic loop and is set equal to the bandwidth of the current controller [4], T_{samp} is the sampling time, λ is a part of an added "leakage term" [4], $\widehat{e}_d$ is the estimated d-axis back-emf and $\widehat{e}_q$ is the estimated q-axis back-emf. The term $\lambda sign(\widehat{\omega}_{r,k})$ actually equals $\frac{\lambda|\widehat{\omega}_{r,k}|}{\widehat{\omega}_{r,k}}$. Actually, $\lambda|\widehat{\omega}_{r,k}|$ is part of the leakage term mentioned. This leakage term is introduced in the estimation of the rotor flux. Instead of having a pure integrator, the leakage term is used to create a lowpass filter [4]. In this thesis, the estimated rotor flux magnitude is not integrated, but is assumed to be known and constant. But $\lambda|\widehat{\omega}_{r,k}|$, which would be the rotor flux lowpass filter bandwidth, is still in the equations. In order to use this estimator in the simulations, this term had to be changed somewhat for speeds higher than a certain threshold, as was mentioned briefly above. From initial simulations, the system did not work well for high enough speeds having this term unchanged. Hence, for speeds lower than the threshold, the term is unchanged, i.e. equals to $\lambda sign(\widehat{\omega}_{r,k})$. For speeds higher than the threshold, the term is set to $\frac{\lambda\omega_{lim}}{\widehat{\omega}_{r,k}}$ which decreases with higher speed, where ω_{lim} denotes the electrical speed threshold.

The back-emf in the estimated dq-frame is calculated as

$$\begin{aligned}\widehat{e}_d &= \widehat{u}_{sd} - \widehat{R}_s\widehat{i}_{sd} + \widehat{\omega}_r\widehat{L}_q\widehat{i}_{sq} \\ \widehat{e}_q &= \widehat{u}_{sq} - \widehat{R}_s\widehat{i}_{sq} - \widehat{\omega}_r\widehat{L}_d\widehat{i}_{sd}.\end{aligned} \tag{5.16}$$

In (5.16), it has been assumed that the current controller is fast enough so that the current derivative is negligible. Also, the inductances used to estimate the back-emf, $\widehat{L}_d$ and $\widehat{L}_q$, are absolute inductances. In this implementation, the absolute inductances have been estimated from Figure 4.20 for low currents. The dq-current used in (5.16) is the estimated dq-frame current reference from the controllers and the dq-voltage used is the reference voltage from the current controller.

5.3 Magnetic Pole Identification

The magnetic pole identification tried is based on the injection of voltage pulses, one positive and one negative, in the $\alpha\beta$-frame along the estimated d-axis. The basic principles are found in e.g. [48] and [33]. However, the injected voltage is defined in the $\alpha\beta$-frame, and the current is investigated also in the $\alpha\beta$-frame since it is directly measurable and the magnitude of the $\alpha\beta$-current should be the same as the dq-current due to amplitude invariant transformation.

The application of the test voltages should be done after an initial estimation of the rotor position and before starting the machine. Therefore, the basic setup that has been used for the simulations has been altered to fit the scenario. Since the main objective is to see if there are any current magnitude differences due to positive and negative voltage injection along the estimated d-axis, the controllers are disconnected and the injected voltage references are directly used as input to the PWM-controlled inverter model. No closed-loop control is used for these simulations.

The injected voltage is defined as two vectors applied at two different time instants. The voltage vectors are applied along the estimated d-axis, one having the same angle as the estimated rotor angle and the other having the estimated rotor angle shifted 180 degrees. The voltage vectors have magnitude V and are applied equally long time and are each applied during Δ seconds. In order to let the current response due to the first voltage vector die out before applying the second voltage vector, there is a certain amount of time, δt seconds, before the second voltage vector is applied. This time δt is determined as ten times the electrical time constant of the machine's equivalent RL-circuit in order to provide safety margin.

6

Simulation Results

This chapter will provide the results of the simulations of the proposed methods from earlier chapters. The simulation environment was developed in Section 4.2 and the basic parameters used for all simulations are found in Table 6.1.

Table 6.1: Parameters and settings used for all the simulations.

Parameter	**Value**	**Description**
$f_{sampling}$	20 kHz	Sampling frequency
U_{DC}	750 V	DC voltage
I_N	10 A_{rms}	Rated current
n_N	6000 rpm	Rated speed
m	17 kg	Mass of concrete drill
k	17.8	Gear ratio (high speed versus low speed)
r	0.051 m	Drill bit radius
g	9.81 m/s^2	Gravitational constant
n_p	5	Number of pole pairs
$J = \widehat{J}$	0.00086 kgm^2	Moment of inertia
μ_s	0.6	Static friction coefficient
μ_k	0.5	Kinetic friction coefficient
$\lambda_{PM} = \widehat{\lambda}_{PM}$	0.11 Wb	Actual and estimated PM flux
$R_s = \widehat{R}_s$	1.05 Ω	Actual and estimated resistance
$\widehat{l}_{dd}$	7.5 mH	d-inductance for current controller
$\widehat{l}_{qq}$	5 mH	q-inductance for current controller
$\widehat{L}_d$	11 mH	d-inductance for SCVM
$\widehat{L}_q$	10 mH	q-inductance for SCVM

The resistance, rotor flux magnitude and inductances have been measured as described in Section 4.1. Further, the value of the drill mass and also the radius of the drill bit were measured. The estimated total moment of inertia is probably lower than the real moment of inertia since the gear box inertia was omitted in the estimation. However, a higher moment of inertia in reality could perhaps yield a positive effect since it might dampen oscillations that might occur in the simulations, especially for the signal injection simulations. The sampling frequency, the DC voltage, the rated current, the rated speed, and the number of pole pairs were given from a real setup the simulations are trying to mimic.

6.1 Control System Verification

Before starting to implement rotor angle estimators, the current and speed controllers has to be verified to work properly. This was done having the parameters shown Table 6.1 and having the bandwidth of the current and speed controller selected as $\alpha_{cc} = 500$ rad/s and $\alpha_{sc} = 20$. Further, for both of the tests, it was assumed that the rotor position and speed were known precisely instead of using an estimator.

The current controller tests were made without the speed controller. Hence, for this simulation to work, the rotor was fixed and could not move during the simulation. This is since when applying a q-current and having no speed dependent load, there is nothing that would stop the machine from rotating and accelerating. If the machine would have accelerated, there would have been a risk of having a high back-emf which would have made the current control difficult. Therefore, in order to test the current controllers' function, the rotor had to be fixed. The d-current reference was stepped at 0.01 seconds to 1 A while the q-current reference was stepped at 0.03 seconds to 1 A as well. The results are seen in Figure 6.1. The measured rise time of both current are 4.3 ms while the theoretical rise time is calculated to be 4.4 ms which is rather close. As can also be seen, both currents follow the shape of a first-order step response, just as what the controllers are designed to do. However, it is seen that the cross-coupling is not completely compensated for since for both current steps, the other current component is affected by the step. This could be due to the cross-coupling incremental inductances in the machine model, where a change of voltage or current in one axis would yield a change on the other axis.

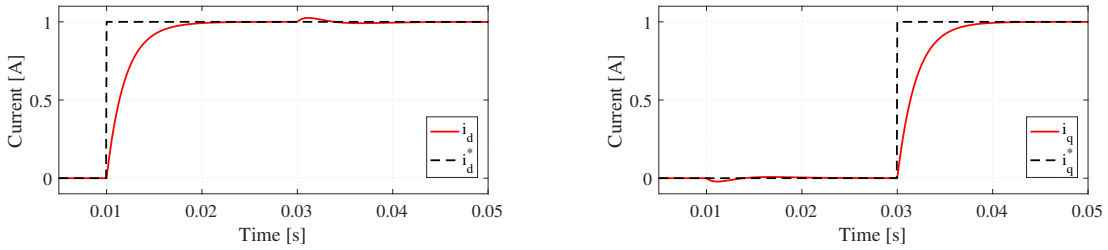

(a) d-current versus its reference **(b)** q-current versus its reference

Figure 6.1: Current controller verification.

The speed controller test was made with the current controllers for two low reference speed steps (50 rpm at 1 ms and 70 rpm at 0.5 s) in order to avoid reaching the current limit. If the current limit would have been reached, the electrical torque would have been constant and the speed would have been ramped linearly. To see whether or not the speed controller works as it should, the speed step response should look similar to a first-order step response with the rise time 0.1099 seconds. In Figure 6.2 the rotor speed is visualized against the reference value. It is seen that the speed becomes nonzero at 0.1 seconds, which is actually some time after the speed reference is stepped. This is because the machine has to overcome the static friction torque before it can start rotating. The measured rise time for the first speed

step of 50 rpm is 0.1537 seconds which is a bit higher than the expected rise time. This could be due to the static friction load torque and the mechanical machine model having a discontinuity when the rotor starts to turn. In that moment, the load torque is stepped to a lower value. Inspecting Figure 6.2b, this step can be seen at about 0.1 seconds. After the step, the speed controller has to control the torque reference so that the correct speed is attained. Perhaps the regulation becomes slow due to the integrator in the speed controller. Later on at 0.5 s, the speed is stepped once again to 70 rpm. This time, the measured rise time is 0.1064 s which is closer to the actual rise time.

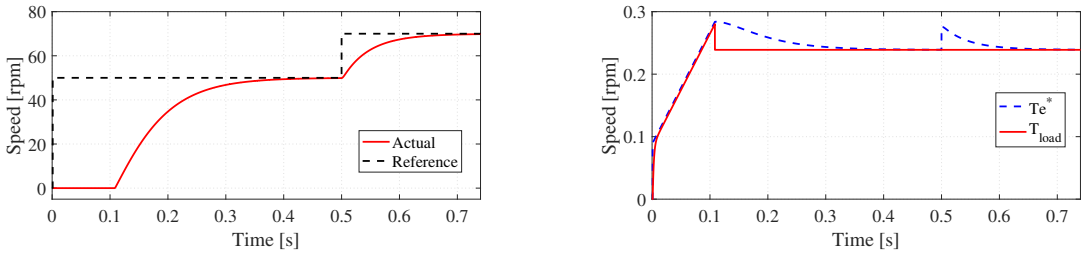

(a) Rotor speed in rpm

(b) Torque reference and load torque

Figure 6.2: Speed controller verification.

6.2 High Frequency Signal Injection

In this section the high frequency pulsating voltage injection scheme presented in the previous chapter is going to be tested and evaluated. Firstly, the choice of voltage magnitude is to be tested. Secondly, the choice of frequency of the injected signal is to be investigated. Thirdly, having decided an optimal voltage magnitude and frequency, several tests are done in order to investigate the performance of this method when having parameter errors, and when trying to start the machine during various loads. The speed limit is also investigated. In Table 6.2, filter parameters and other specific parameters used for all these simulations are found.

Table 6.2: Filter settings used for all the simulations.

Parameter	Value	Description
$\alpha_{notch,1}$	$2\omega_{HF}$	Filter frequency for notch filter to PI controller
$\alpha_{notch,2}$	ω_{HF}	Filter frequency for notch filter on $\widehat{i}_{dq}$ to current controller
α_{bpf}	ω_{HF}	Passed frequency for bandpass filter
α_u	$1.1 \cdot \omega_{HF}$	Upper frequency for bandpass filter
α_l	$0.9 \cdot \omega_{HF}$	Lower frequency for bandpass filter

In order to have a good input to the PI controller, the compensation in (5.11) has to be performed appropriately. Therefore, before each test, the compensation of the cross-coupling inductance effect was determined by injecting only the high frequency signal to the machine and after the simulation, calculate the compensation term.

In the simulation, the compensation becomes perfect in the sense that the machine parameters, such as the inductances, are known exactly. The compensation term is calculated as a mean since for changing current (e.g. due to inverter switching), the inductances changes and the actual compensation term alternates as well.

When testing different voltage magnitudes and frequencies, the current controllers and the speed controller were active in the control system in order to test the stability of the whole system. Continuing with parameter errors, the whole system was also used. After these simulations, the starting procedure was tested and this comprises tests of (in this order): the initial position estimation, the magnetic pole identification, and lastly, the startup. For the initial position estimation and the magnetic pole identification, the current controllers and the speed controller were not used (refer to the switch in Figure 5.2). During the startup tests, the whole control system was used again, i.e. the current and speed controllers were active.

6.2.1 Testing Different Voltage Magnitudes

As a first test, different injected voltage magnitudes were tested in order to see how this parameter affects the outcome of the estimation. The voltages tested are 10 V, 20 V, and 5 V. The bandwidths of the control system and the parameters used in the signal injection estimation procedure are found in Table 6.3. For all tests, the initial rotor angle was put to 10 degrees and the initial speed was put to zero. The injected signal frequency used is 600 Hz for all tests as well.

In Figure 6.3 the estimated speed and position is visualized against the real speed and position of the machine. The injected voltage magnitude is 10 V.

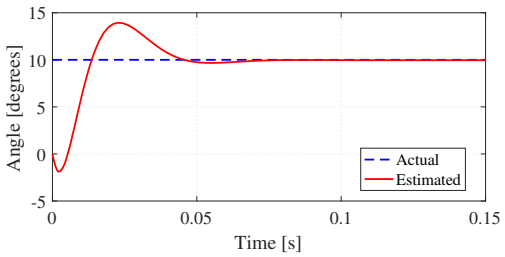

(a) θ_r est. (electrical degrees).

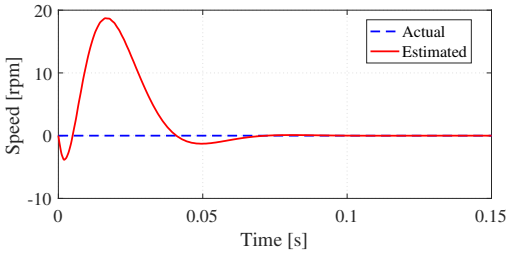

(b) n est. ($n = \frac{60\omega_r}{2\pi n_p}$, speed).

Figure 6.3: Angle and speed estimation. $V_{HF} = 10$ V and $f_{HF} = 600$ Hz. Initial rotor position is set to 10 electrical degrees.

There is a steady-state estimation error in Figure 6.3a. It is found to be about 0.04 electrical degrees which is rather small. The overshoot peaks at around 13.94 electrical degrees which is 3.94 degrees above the actual rotor position. Further, the time to reach steady-state is just below 0.15 seconds. The reason why the estimates overshoot is because of the complex-conjugated pole pair of the PI-controller used to estimate the speed and position. Also, no actual rotor movement is seen in Figure 6.3 which is desirable.

Table 6.3: Parameters and settings used for the simulations with different V_{HF}. $\omega_{HF} = 2\pi 600$ rad/s. l_{qd} compensation is based on (5.11) while A_e is calculated from (5.12).

Parameter	$V_{HF} = 5$ V	$V_{HF} = 10$ V	$V_{HF} = 20$ V
α_{cc}	$\frac{\omega_{HF}}{10} = 2\pi 60$	$\frac{\omega_{HF}}{10} = 2\pi 60$	$\frac{\omega_{HF}}{10} = 2\pi 60$
α_{PI}	$\frac{\omega_{HF}}{40} = 2\pi 15$	$\frac{\omega_{HF}}{40} = 2\pi 15$	$\frac{\omega_{HF}}{40} = 2\pi 15$
α_{sc}	$\frac{\alpha_{PI}}{7} = 2\pi 2.143$	$\frac{\alpha_{PI}}{7} = 2\pi 2.143$	$\frac{\alpha_{PI}}{7} = 2\pi 2.143$
l_{qd} compensation	0.0085	0.0170	0.0340
A_e	0.0444	0.0887	0.1771

In Figure 6.4a, the error signal feeding the PI controller in Figure 5.2 is found for the case above having $V_{HF} = 10$ V. It can be seen that it follows the theory nicely and decreases with time. This is consistent also with Figure 6.3a, where the estimated angle approaches the real angle. The theoretical line has been drawn using (5.11) with the actual angle error in the simulation and the machine's inductances. Also, the reason why the theoretical error signal has a square-shaped ripple in the transient, having the same frequency as the injected signal, is because of the implemented inductances. Because of the injected signal, the inductances pulses, see e.g. l_{dd} in Figure 6.4b.

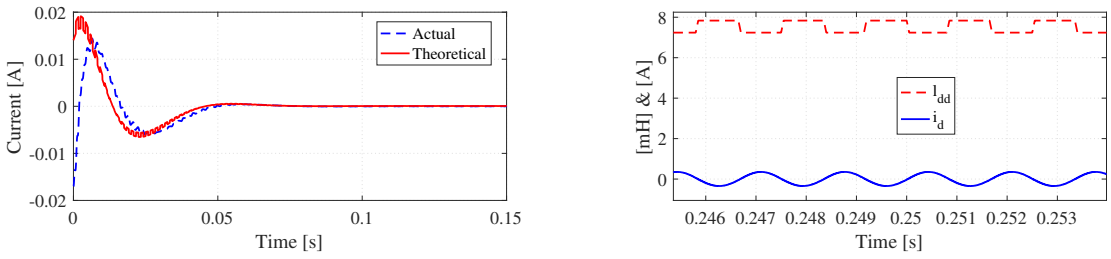

(a) Error signal to the PI controller. **(b)** Actual l_{dd} versus actual i_d.

Figure 6.4: The error signal to the PI controller is dependent on the inductances of the machine which changes due to the injected signal.

When changing the injected voltage magnitude to 20 V instead of 10 V, having the same frequency, the following results in Figure 6.5 were obtained.

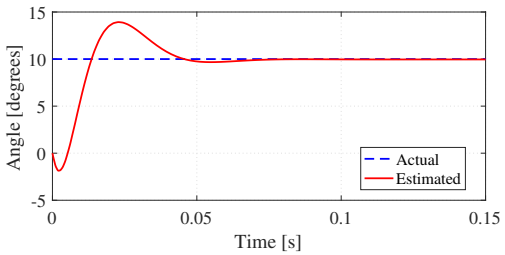

(a) θ_r est. (electrical degrees).

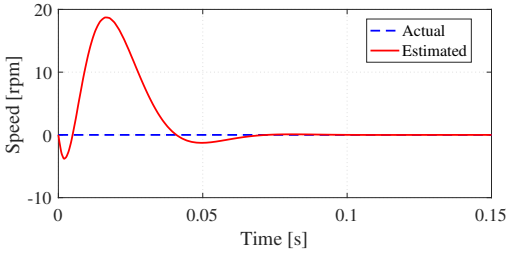

(b) n est. ($n = \frac{60\omega_r}{2\pi n_p}$, speed).

Figure 6.5: Angle and speed estimation. $V_{HF} = 20$ V and $f_{HF} = 600$ Hz. Initial rotor position is set to 10 electrical degrees.

In Figure 6.5, it is seen that the rotor keeps still during the transient. This results in a steady-state error of 0.04 degrees, which is what was achieved with 10 V. Also, the overshoot was found to be 13.93 electrical degrees, as seen in Figure 6.5, which is almost the same as for the case having $V_{HF} = 10$ V. Further, the angle estimation reaches steady-state at less than 0.15 seconds which is the same time needed for 10 V. The error signal to the PI controller is seen to follow the theory nicely for this case as well, see Figure 6.6, and the same kind of ripple is seen as was visible in Figure 6.4a. Further, since the voltage is doubled compared to the 10 V case, the error signal reaches about twice the peak value of the 10 V case, compare Figures 6.4a and 6.6. This is since the error signal is directly proportional to the injected voltage, see (5.12).

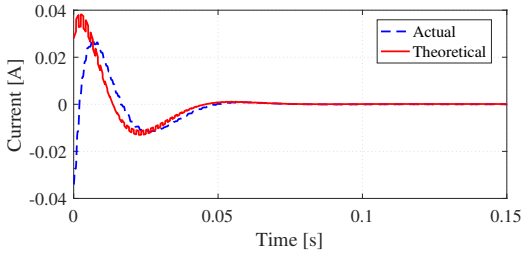

Figure 6.6: Error signal to the PI controller having $V_{HF} = 20$ V and $f_{HF} = 600$ Hz.

In Figure 6.7 the estimated position and speed are seen for having 5 V injected voltage with the same frequency as before. It is found that the rotor keeps still and the steady-state angle estimation error is about 0.039 degrees, which is basically the same as for 10 V and 20 V. Further, the overshoot is a bit higher than for the other two cases, peaking at about 13.98 electrical degrees and the estimation reaches steady-state at approximately the same time as before (a bit less than 0.15 seconds) which is not a surprise since the bandwidths are the same for all three cases. In Figure 6.8, the error signal is seen, once again, to follow the theory nicely and reaches about half the peak value compared to the 10 V case (see Figure 6.4a) which is expected.

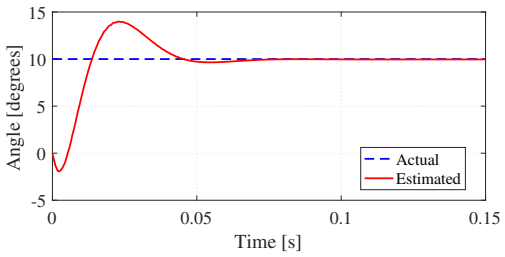

(a) θ_r est. (electrical degrees).

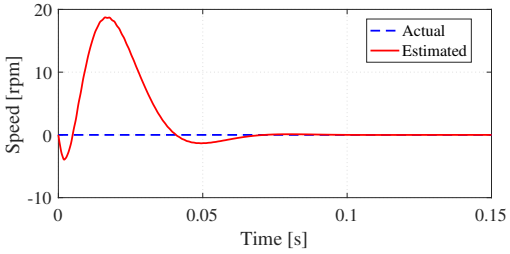

(b) n est. ($n = \frac{60\omega_r}{2\pi n_p}$, speed).

Figure 6.7: Angle and speed estimation. $V_{HF} = 5$ V and $f_{HF} = 600$ Hz. Initial rotor position is set to 10 electrical degrees.

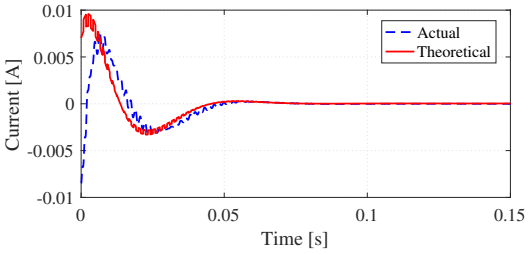

Figure 6.8: Error signal to the PI controller having $V_{HF} = 5$ V and $f_{HF} = 600$ Hz. Initial rotor position is set to 10 electrical degrees.

From this short survey, it is important to notice that the peak error signal seems to increase with the injected voltage magnitude as seen in Figure 6.8, 6.4, and 6.6. The error signal should be detectable and it should be possible to retrieve it from the measured currents. Hence, this would favor the case having 20 V since it reached a higher peak error signal. However, a higher injected voltage would increase overall losses compared to when injecting a signal having a lower voltage magnitude. Further, no rotor movement was visible for any of the three test cases. Also, the estimation overshoot and the steady-state error for the three cases seem to be rather constant or at least within a close range of each other. In the coming subsections, 10 V is used as the injected signal magnitude since it would induce lower losses than the 20 V signal and would have a higher error signal magnitude than the 5 V signal which would be easier to measure.

6.2.2 Testing Different Injection Frequencies

Using the bandwidth selection as in (5.14), the injected voltage magnitude was kept constant at 10 V but the frequency of the signal was changed in order to see the dependence of the injected frequency on the performance of the system. This means that the bandwidths are dependent on the injected signal frequency. So, the effects of the injected frequency on the system performance is at least twofold: firstly, the frequency affects the injected signal, and secondly, the injected frequency determines the controller bandwidths as of now. The important test parameters are found in Table 6.4. The initial rotor position is set to 10 electrical degrees as before.

Table 6.4: Parameters and settings used for the simulations with different ω_{HF}. $V_{HF} = 10$ V. l_{qd} compensation is based on (5.11) while A_e is calculated from (5.12).

Parameter	$\omega_{HF} = 2\pi 600$	$\omega_{HF} = 2\pi 800$	$\omega_{HF} = 2\pi 300$
α_{cc}	$\frac{\omega_{HF}}{10} = 2\pi 60$	$\frac{\omega_{HF}}{10} = 2\pi 80$	$\frac{\omega_{HF}}{10} = 2\pi 30$
α_{sc}	$\frac{\omega_{HF}}{200} = 2\pi 3$	$\frac{\omega_{HF}}{200} = 2\pi 4$	$\frac{\omega_{HF}}{200} = 2\pi 1.5$
α_{PI}	$\frac{\omega_{HF}}{60} = 2\pi 10$	$\frac{\omega_{HF}}{60} = 2\pi 13.33$	$\frac{\omega_{HF}}{60} = 2\pi 5$
l_{qd} compensation	0.017	0.0127	0.0339
A_e	0.0887	0.0664	0.1761

The first test frequency was set to 800 Hz while the second was set to 300 Hz. The results from these tests are then compared to the case above having 10 V and 600 Hz, the results of which are seen in e.g. Figure 6.3. The estimation results from the 800 Hz case are found in Figure 6.9 and it is seen that the time to reach steady-state is about 0.1 seconds which is a bit less than the case having 600 Hz. However, the angle estimate peaks at 13.93 degrees and reaches a steady-state error of 0.021 degrees. The peak value is about the same as for the 600 Hz case while the steady-state error is less. Also, the estimated speed peaks at about 25 rpm which is higher than in Figure 6.3b.

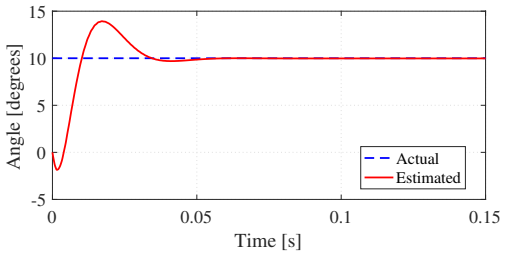

(a) θ_r est. (electrical degrees).

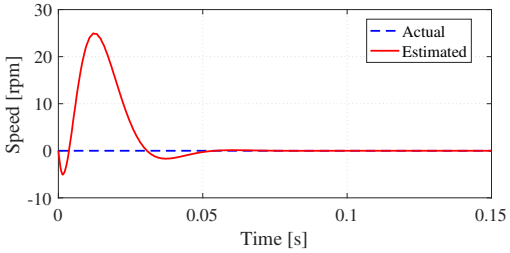

(b) n est. ($n = \frac{60\omega_r}{2\pi n_p}$, speed).

Figure 6.9: Angle and speed estimation. $V_{HF} = 10$ V and $f_{HF} = 800$ Hz. Initial rotor position is set to 10 degrees. 800 Hz bandwidths.

In Figure 6.10, the error signal to the PI controller is visualized and it is seen, compared to having a 600 Hz signal as in Figure 6.4a, that it reaches a slightly lower peak value. This is since the error signal is inversely proportional to the injection frequency, see (5.12).

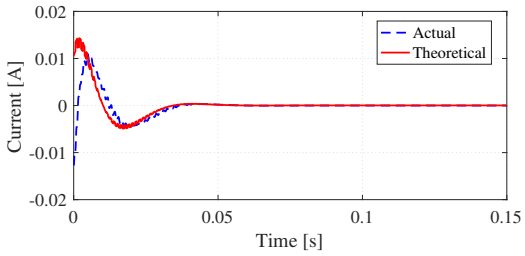

Figure 6.10: Error signal to the PI controller having $V_{HF} = 10$ V and $f_{HF} = 800$ Hz.

When changing the frequency to 300 Hz the results in Figure 6.11 were obtained. The estimation is stable and no rotor movement is seen during the estimation process. Further, the steady-state error is about 0.117 electrical degrees and the estimated angle peaks at 13.95 degrees which is comparable to the case having 600 Hz frequency and 10 V magnitude. Further, the overshoot in the speed estimation is higher for 600 Hz than for 300 Hz, this is seen when comparing Figure 6.11b with Figure 6.3b. The bandwidths are selected using the same formulas as in (5.14). This means that the bandwidths are the lowest for 300 Hz while they are the highest for 800 Hz for these three tests. This means that the dynamics of the speed control for the case having 300 Hz should be slower than for the other cases. Further, the estimation process is a bit slower. It is found that the time to reach steady-state is just above 0.2 seconds.

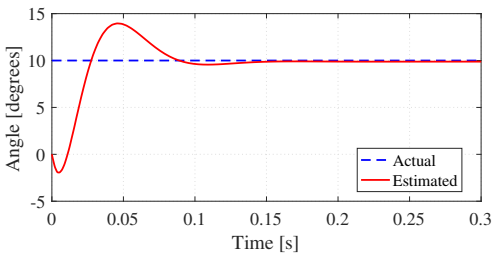

(a) θ_r est. (electrical degrees).

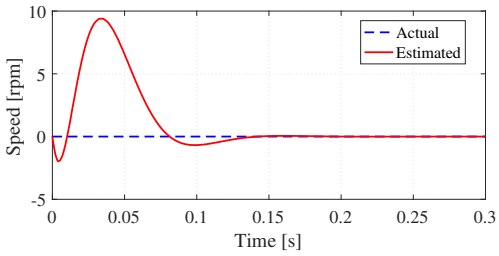

(b) n est. ($n = \frac{60\omega_r}{2\pi n_p}$, speed).

Figure 6.11: Angle and speed estimation. $V_{HF} = 10$ V and $f_{HF} = 300$ Hz. Initial rotor position is set to 10 degrees. 300 Hz bandwidths.

The error signal to the PI controller is seen for the 300 Hz case in Figure 6.12. Compared to the case with 800 Hz as the injected frequency, the error signal peak is now higher (compare with e.g. Figure 6.10). As stated earlier, this is because of that the error signal is inversely proportional to the injected frequency.

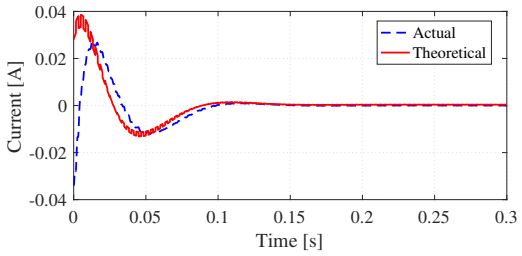

Figure 6.12: Error signal to the PI controller having $V_{HF} = 10$ V and $f_{HF} = 300$ Hz.

Hence, with the current bandwidth selection, the time to reach steady-state increases with decreasing frequency, the steady-state error decreases with increasing frequency, the peak estimate of the speed increases with frequency, and the peak angle estimate seems to remain constant.

Another test was made abandoning the bandwidth selection above, in order to see what happens if the bandwidths are selected as constants (using the bandwidths of the 600 Hz case) but changing the injected frequencies to e.g. 800 Hz (i.e. having bandwidths independent of the injected frequency). The results for the case having 800 Hz are shown in Figure 6.13.

No rotor movement is seen for the case having 800 Hz as the signal frequency and the steady-state error (0.021 electrical degrees) is less than the case having 600 Hz and 10 V. The overshoot is now less than for the other cases (peaking at around 13.19 electrical degrees) but the time to reach steady-state is (not surprisingly) about the same as for the case having the 600 Hz, 10 V signal.

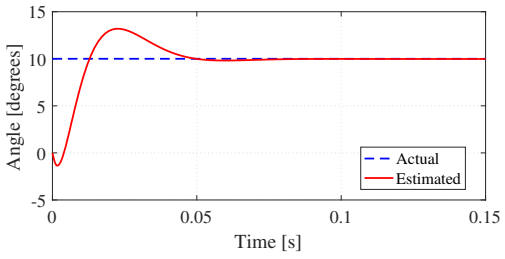

(a) θ_r est. (electrical degrees).

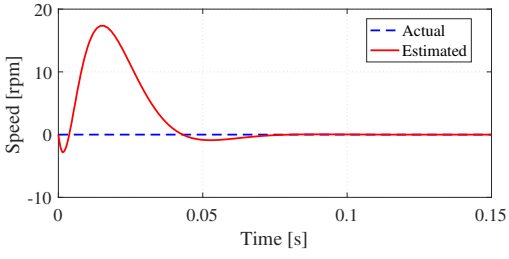

(b) n est. ($n = \frac{60\omega_r}{2\pi n_p}$, speed).

Figure 6.13: Angle and speed estimation, having $V_{HF} = 10$ V and $f_{HF} = 800$ Hz. Initial rotor position is set to 10 degrees. 600 Hz bandwidths.

As a conclusion of these tests, the smallest steady-state error was obtained with the 800 Hz signal while the 300 Hz signal gave the highest steady-state error. The complex-conjugated pole pair of the PI-controller resulted in overshoot in the estimation of the speed and position. Taking losses into account, a 600 Hz signal will induce less losses (e.g. in the iron core and the stator [34]) than an 800 Hz signal. Hence, from now on, 600 Hz is to be used in this project.

6.2.3 Estimation with Parameter Errors

Before trying the starting procedure with signal injection position estimation, the effects of parameter errors was tested using the same test setup as in Section 6.2.1 and 6.2.2. The tested parameters were A_e and the l_{qd} compensation term since these affect the estimation process directly through the PI control parameters and the error signal to the PI controller respectively. Hence, a wrongly estimated A_e should affect the estimation dynamics since it affects the poles of the error signal control while the l_{qd} compensation term should affect the estimated rotor angle.

In Figure 6.14, A_e is underestimated and is 90 percent of the value found in Table 6.4 for an injected signal of 600 Hz and 10 V. The steady-state error is about 0.04 electrical degrees while the peak estimate is about 13.98 degrees which both are comparable to perfect estimation of A_e, see Figure 6.3a. It can also be seen when comparing Figure 6.3a with Figure 6.14a that the estimation is a bit faster now, reaching steady-state at about 0.1 seconds. This is since the PI control parameters are inversely proportional to A_e.

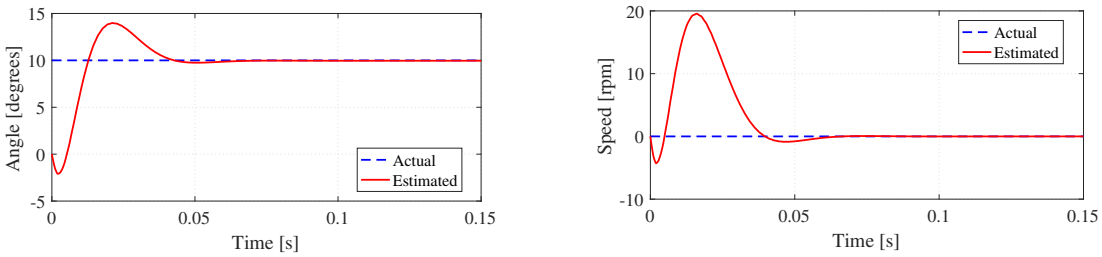

(a) θ_r est. (electrical degrees). **(b)** n est. ($n = \frac{60\omega_r}{2\pi n_p}$, speed).

Figure 6.14: Angle and speed estimation ($\widehat{A}_e = 0.9A_e$). $V_{HF} = 10$ V and $f_{HF} = 600$ Hz. $\alpha_{PI} = \omega_{HF}/40$, $\alpha_{sc} = \alpha_{PI}/7$. Initial rotor position is set to 10 degrees.

In Fig. 6.15, A_e is overestimated with 10 percent. The steady-state error is about 0.04 electrical degrees while the peak estimate is about 13.93 degrees which is lower than when underestimating A_e. Further, since A_e is higher now, the time to reach steady state is a bit higher as well, about 0.15 seconds. The steady-state error seems to be unaffected by the estimation of A_e while the peak estimate seems to be affected by the choice of A_e a bit.

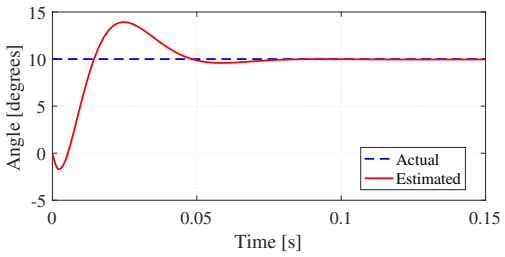

(a) θ_r est. (electrical degrees).

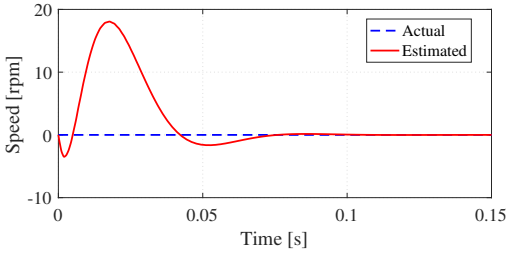

(b) n est. ($n = \frac{60\omega_r}{2\pi n_p}$, speed).

Figure 6.15: Angle and speed estimation ($\widehat{A}_e = 1.1A_e$). $V_{HF} = 10$ V and $f_{HF} = 600$ Hz. $\alpha_{PI} = \omega_{HF}/40$, $\alpha_{sc} = \alpha_{PI}/7$. Initial rotor position is set to 10 degrees.

In Figure 6.16, the l_{qd} compensation (see Table 6.4 for the 600 Hz and 10 V signal) is underestimated with 10 percent. It is seen that the absolute steady-state error is about 1.06 electrical degrees while the peak estimate is 15.42 degrees which is higher than when having perfect compensation, see Figure 6.3. Further, in Figure 6.16 it is also seen that the peak estimate of the speed is a bit higher as well. In Figure 6.17 it is seen that the PI controller is able to control the error towards zero but the theoretical signal is a bit negative due to the steady-state angle estimation error. The estimates are higher than when having perfect compensation, as in e.g. Figure 6.3a. This is due to the fact that the l_{qd} compensation term is less than it should be and this results in a positive DC offset affecting the error signal. This DC offset is controlled to zero together with the rest of the error signal in the PI controller which gives a higher estimated angle and speed.

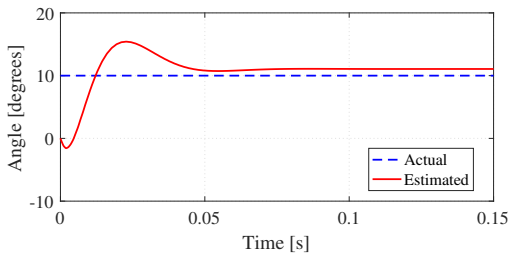

(a) θ_r est. (electrical degrees).

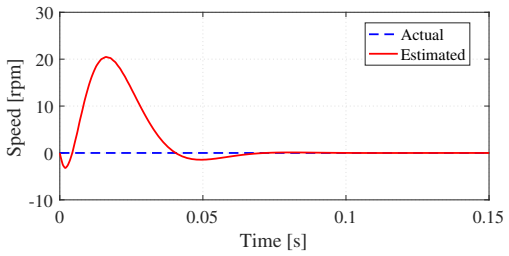

(b) n est. ($n = \frac{60\omega_r}{2\pi n_p}$, speed).

Figure 6.16: Angle and speed estimation ($\widehat{l}_{qd} = 0.9l_{qd}$). $V_{HF} = 10$ V and $f_{HF} = 600$ Hz. $\alpha_{PI} = \omega_{HF}/40$, $\alpha_{sc} = \alpha_{PI}/7$. Initial rotor position is set to 10 degrees.

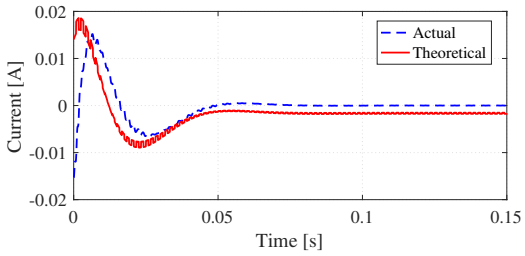

Figure 6.17: The actual error signal versus the theoretical one.

In Figure 6.18, the l_{qd} compensation is instead overestimated with 10 percent. There is a steady-state error of about 1.138 electrical degrees, while the peak estimate is about 12.47 degrees which is smaller than when underestimating the l_{qd} compensation term. It seems that the opposite happens when overestimating compared to the underestimation case of the compensation term. This could be since the PI controller would get an error signal with a negative DC offset instead of a positive DC offset when overestimating the compensation term.

It is interesting to notice the difference between Figure 6.17 and Figure 6.19, where the theoretical error signal has different signs. This is due to the difference between the actual angle and the estimated one. Further, in Figure 6.18 it is also seen that the peak estimate of the speed is lower than in Figure 6.16b.

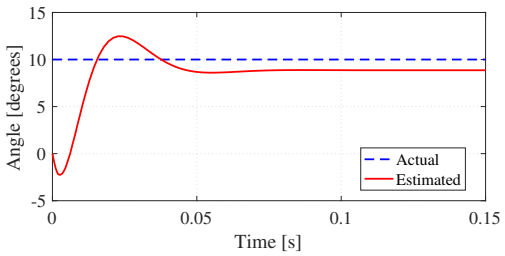

(a) θ_r est. (electrical degrees).

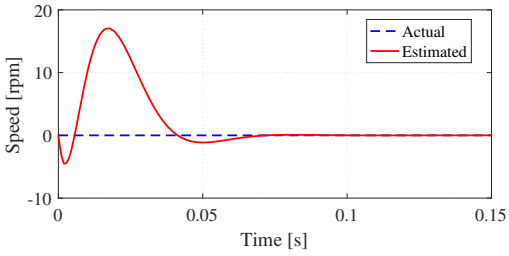

(b) n est. ($n = \frac{60\omega_r}{2\pi n_p}$, speed).

Figure 6.18: Angle and speed estimation ($\widehat{l}_{qd} = 1.1 l_{qd}$). $V_{HF} = 10$ V and $f_{HF} = 600$ Hz. $\alpha_{PI} = \omega_{HF}/40$, $\alpha_{sc} = \alpha_{PI}/7$. Initial rotor position is set to 10 degrees.

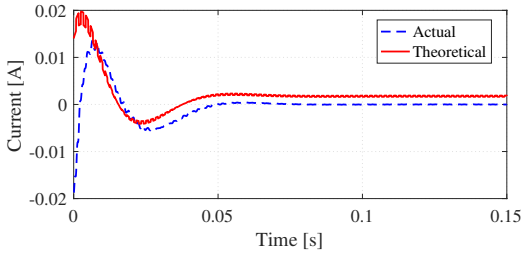

Figure 6.19: The actual error signal versus the theoretical one.

Although the system maintains stability with these parameter errors, it is found that the most critical parameter for a good angle estimation ability seems to be the l_{qd}

compensation term. Since both A_e and the l_{qd} compensation term both depend on the dynamic inductances, these might be wrongly estimated in a real drive system. Therefore, it is interesting to see the effects above.

6.2.4 Estimating Different Initial Positions

In this section, an evaluation of the signal injection scheme's performance in finding the initial rotor angle is tested. The first simulation was done having the same bandwidths as in Table 6.3 for the chosen signal (10 V, 600 Hz). The only change from the simulations in Section 6.2.1, except the lack of current and speed controllers, is the static friction load torque value, it had to be changed from about 0.29 Nm to 0.5 Nm. The reasoning behind this choice is explained next.

From initial simulations, it was found that having $C = \mu_s mgr/k \approx 0.29$ Nm resulted in oscillating results since no speed controller was used to fix the rotor to standstill. Therefore, there were two obvious options, either decrease the injected voltage to decrease the induced torque or increase the static torque just above the induced torque ripple. Reducing the injected voltage was considered a worse choice due to the lower magnitude of the error signal, i.e. in reality it might not be possible to measure it properly, see Figure 6.8. Further, the torque ripple magnitude was seen to go to about 0.4 Nm, which is less than twice $\mu_s mgr/k$. Also, the static friction used may not be similar to the real static friction since the coefficient was from a case having steel on concrete, not diamond (used on the drill bit teeth) on concrete. Other effects that has not been taken into consideration which might affect the friction is side friction effects due to accumulation of iron and concrete splinters, and dust. Also, no real load data has been available to compare with. Due to these uncertainties, increasing the static friction torque to 0.5 Nm would make the rotor keep still during the simulations and would perhaps be a reasonable value in reality.

In Figures 6.20 and 6.21, all the results from the initial position estimation simulations are shown. In Figures 6.20b, 6.21b, 6.21c, and 6.21d, it can be seen that the steady-state error is about $\pm$ 180 degrees. However, in Figures 6.20a, 6.20c, 6.20d, and 6.21a, the steady-state error is 0.04 degrees (similar to the results of Section 6.2.1). The $\pm$ 180 degrees steady-state error for some initial rotor angles is due to that the PI controller error signal is dependent on twice the estimated position error, see (5.12). Hence, it is shown from these initial position estimation simulations that magnet pole identification is necessary for before startup in order to have an accurately estimated starting angle.

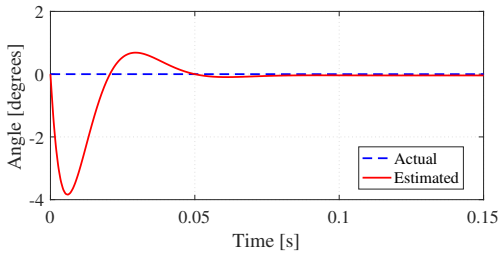

(a) $\theta_{r,init} = 0$ degrees

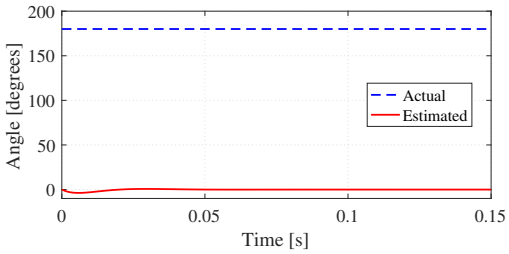

(b) $\theta_{r,init} = 180$ degrees

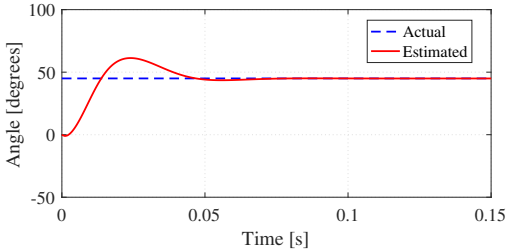

(c) $\theta_{r,init} = 45$ degrees

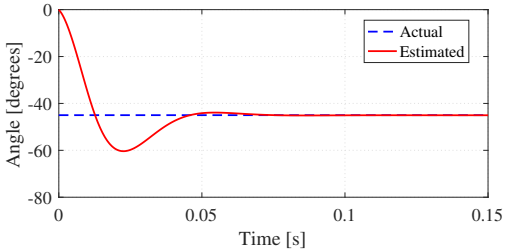

(d) $\theta_{r,init} = -45$ degrees

Figure 6.20: Initial rotor position detection using a 10 V and 600 Hz signal.

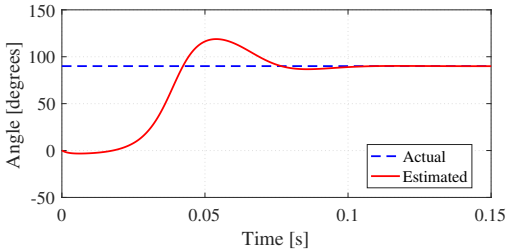

(a) $\theta_{r,init} = 90$ degrees

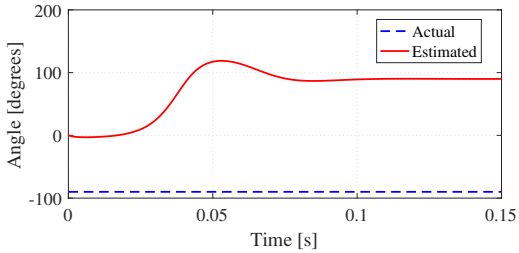

(b) $\theta_{r,init} = -90$ degrees

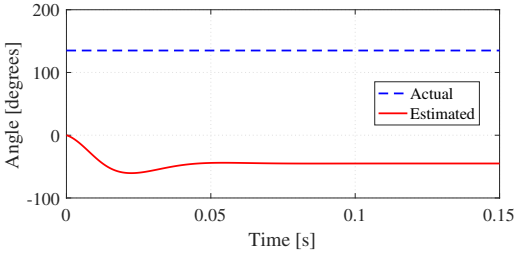

(c) $\theta_{r,init} = 135$ degrees

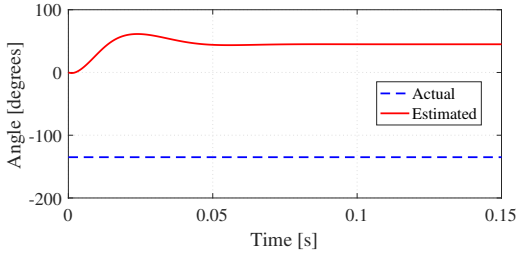

(d) $\theta_{r,init} = -135$ degrees

Figure 6.21: Initial rotor position detection using a 10 V and 600 Hz signal (cont.).

6.2.5 Magnetic Pole Identification

In Section 6.2.4, it was seen that it is necessary to check whether or not the estimated initial position is pointing out the actual north pole. The magnetic pole identification method (see Section 5.3) was only tested for one simulation case, the case having an initial angle of 180 degrees, seen in Figure 6.20b. This since the results of the angle

estimation showed an error angle of 180 degrees. The magnetic pole identification is supposed to correct the angle estimate if it has an error of 180 degrees. Therefore, this simulation case is suitable to test. The scenario is that the initial angle has already been estimated and is therefore known. Now, the polarity of the magnetic field is to be identified by injecting a positive and a negative voltage pulse at the already estimated rotor angle. The static friction torque was set to $C = 0.5$ Nm in order to be consistent with the previous initial position estimation simulations. However, since the injection in this simulation is done purely along the d-axis, there will, for an ideal non-salient machine, not be any torque induced. Due to cross-coupling terms in the machine model (2.13), the q-current might get affected by injecting voltage purely on the d-axis and this has to be taken into account when choosing the test voltage magnitude such that the induced machine torque does not overcome the static load torque.

Having injected two voltage vectors with 40 V magnitude, see Figure 6.22a, each applied during $\Delta = 0.001$ seconds and separated $\delta t = 10\frac{\widehat{l}_{dd}}{\widehat{R}_s} = 0.0714$ seconds, the $\alpha\beta$-current amplitudes in Figure 6.22b were obtained. A difference of $6.192 - 4.987A = 1.205A$ is between the second current response and the first current response, see Figure 6.22b. Hence, the second voltage vector applied seems to achieve some saturation which means that it has been applied along the real positive d-axis. The angle of the second voltage vector was 180 degrees which should also correspond to the actual rotor position. Further, Figures 6.23a and 6.23b shows the speed and position of the rotor during the magnetic pole identification method. It is seen that the rotor keeps still during this test. Thus, the magnetic pole identification was successful.

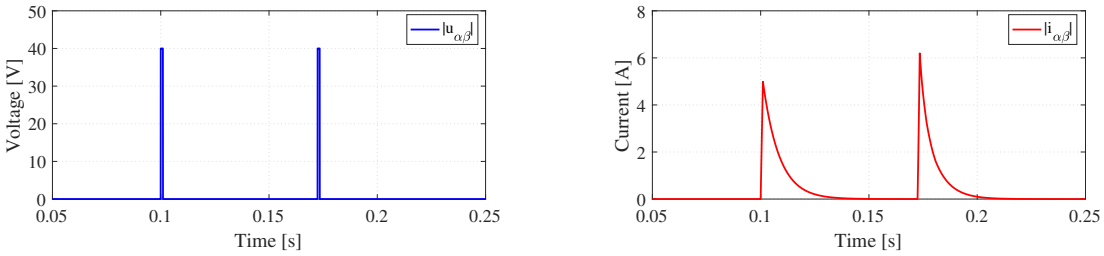

(a) Injected voltage. **(b)** Resulting current.

Figure 6.22: Injection of two voltage vectors along the d-axis. Initial rotor angle of 180 degrees.

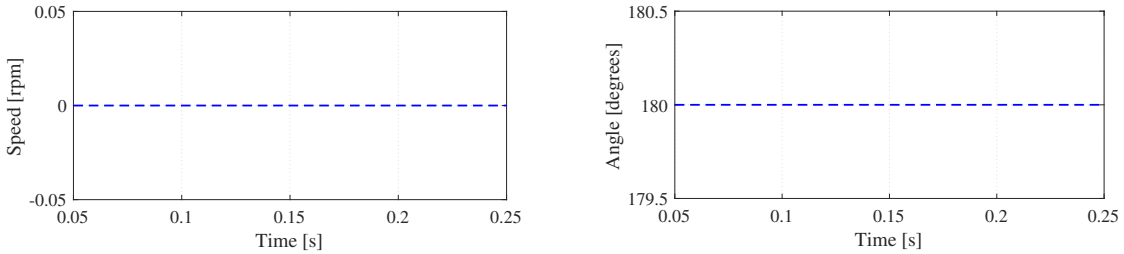

(a) Rotor speed in rpm. **(b)** Rotor position.

Figure 6.23: Rotor position and speed during the magnetic pole identification.

6.2.6 Startup Tests

In this section, the signal injection method is tested for different kinds of speed references and loads. Furthermore, the initial rotor angle is set to zero degrees. As was done earlier, the static friction load and the kinetic friction load was set equal to each other. This since the simulations had trouble converging with the load discontinuity having such a low moment of inertia. The low inertia also makes it easier for the rotor to start accelerating quicker and when the static friction is overcome, the load decreases as a step suddenly and the rotor might start to accelerate quickly. This was believed to be the cause of the difficulties in finishing the simulations. However, the results of stepping the speed reference to 1000 rpm having 0.5 Nm as static friction load and the usual $\mu_k mgr/k$ as kinetic friction load, such as the load in Section 6.2.4, are presented in Figures 6.24, 6.25, 6.26, and 6.27.

As can be seen in Figure 6.24, the speed is ramped until almost 0.4 seconds where the control collapses and the angle error is almost ramped. In Figure 6.25a, the angle error is zoomed in during the time before the collapse and it is seen that the estimation is working poorly during the speed step. This is probably why the machine can not be properly controlled. After 0.3 seconds, the angle error has a local peak at just below 100 degrees which is a lot. After this peak, the speed collapses and the estimation of the speed and angle ramps.

In Figure 6.25b, the machine torque is seen together with the limited torque reference and the load torque. A lot of oscillations are seen. As the load torque changes from static to kinetic, and thus decreases as a negative step change, the machine torque starts to oscillate. The controllers try to keep a steady torque reference but are affected by the estimation of the rotor angle and speed. It is believed that the sudden increase of the rotor angle estimation error, causing the control failure, is due to the low moment of inertia and the instant load torque change. Since the inertia is low, a sudden load change would affect the acceleration. The PI controller does not seem to be fast enough to keep track of the actual rotor position, resulting in a high angle estimation error.

In Figure 6.26, the torque during the speed ramp and after the collapse is seen. In Figure 6.26a, two components are visible, one having the same frequency as the injected signal and one seems to be related to the switched voltage, see Figure 6.27. The reason why there is a frequency component with the same frequency as the injected signal might be due to angle estimation errors causing some of the injected

voltage to be projected on the q-axis. The other component has a higher frequency and is related to the current response of the switched phase voltage. In Figure 6.27, the machine torque waveform is seen to be directly related to the switching of the inverter, as the switch is on, the voltage increases and the current ramps. This affects the torque which also increases. When the switch is turned off, the current and the torque decreases.

Figure 6.26b shows the torque after the speed has collapsed. Now, the machine torque is seen to be shifted against the load torque. The load torque is oscillating due to the sign-dependence of the speed. As the machine torque decreases below the load torque, the sign of the acceleration changes sign and the rotor starts eventually to turn in the opposite direction resulting in negative speed. This would cause the kinetic friction load torque to change sign.

The wrongly estimated rotor angle might be the reason why the controllers can not control the machine torque towards its reference, seen in Figure 6.26b. The speed controller sees only the estimated speed and believes that the rotor is increasing its speed towards the speed reference and the erroneous rotor angle makes it difficult to output the correct dq-voltage. The system seems to be unstable.

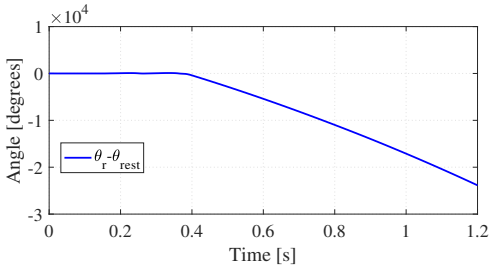

(a) Angle error.

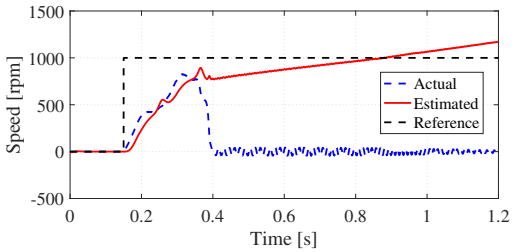

(b) n est. ($n = \frac{60\omega_r}{2\pi n_p}$, speed).

Figure 6.24: Angle and speed estimation for a step of 1000 rpm, having $V_{HF} = 10$ V and $f_{HF} = 600$ Hz. $\alpha_{PI} = \omega_{HF}/40$, $\alpha_{sc} = \alpha_{PI}/7$ as usual. Unequal static and kinetic load.

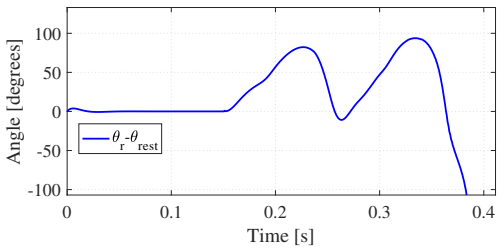

(a) Angle error (zoomed).

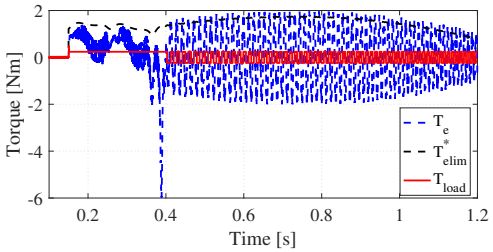

(b) Torque

Figure 6.25: Zoomed in angle error and torque development.

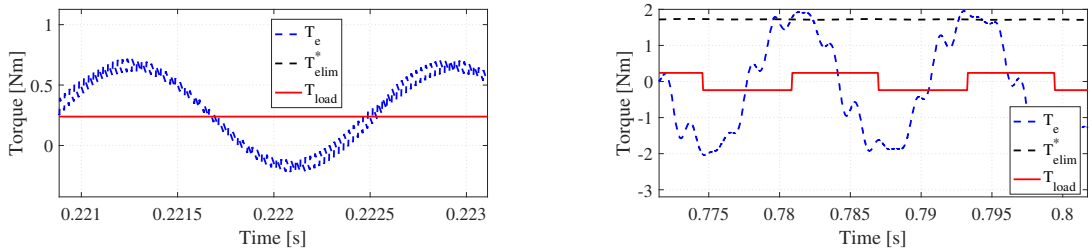

(a) During speed ramp **(b)** After collapse

Figure 6.26: Zoomed in torque development.

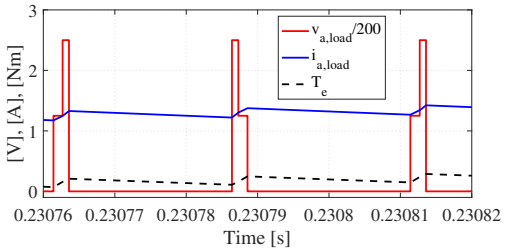

Figure 6.27: Switching effects on current and torque.

With this in mind, the load model was changed so that the static and kinetic friction load was put equal as stated previously. The load was chosen to be 0.5 Nm and the signal injection method was tested with a 500 rpm speed step, the results are seen in Figure 6.28. The angle error has a final steady-state value of about 0.25 degrees, and peaks at 13 degrees as the rotor turns. The rotor speed reaches its reference eventually and the system appears to be stable. The developed torque is seen to follow its reference, although with ripple, see Figure 6.29. The ripple is due to the angle error and the switching as discussed previously. Before the rotor turns, the load torque is set to equal the machine torque in the load model. This is also why the load torque is seen to oscillate at first. The torque reference increases during the speed step and peaks. After the peak, there is a slow decrease of the torque. This is believed to be due to the integrator in the speed controller, which controls the estimated speed towards the reference, since it is done slowly. This is also why the speed is seen to change its acceleration at about 0.3 seconds. As a conclusion of the basic startup tests with no additional load torque, the signal injection implementation seems to have some problems with varying load torque. When the load torque is kept constant it seems to work fine.

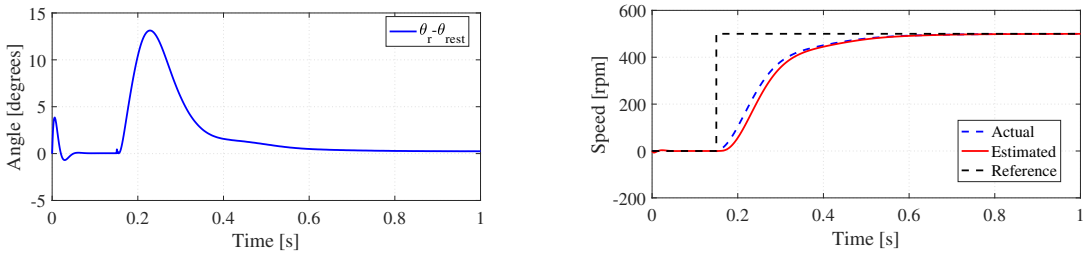

(a) Angle error

(b) n est. ($n = \frac{60\omega_r}{2\pi n_p}$, speed).

Figure 6.28: Angle and speed estimation during a 500 rpm step with equal static and kinetic loads (0.5 Nm). $V_{HF} = 10$ V and $f_{HF} = 600$ Hz. $\alpha_{PI} = \omega_{HF}/40$, $\alpha_{sc} = \alpha_{PI}/7$.

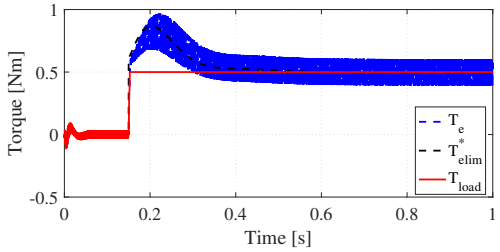

Figure 6.29: Developed machine torque, its reference and the load torque.

From the results so far it became obvious that sudden load changes seems to make the signal injection implementation unstable. Now, the speed is stepped to 1000 rpm at 0.15 seconds and the load torque is ramped with three different slopes at the time instant 1 second keeping the static and kinetic friction loads equal at 0.5 Nm as before. The results when the extra load torque slope was put to 5 Nm/s is seen in Figure 6.30 and Figure 6.31. The simulation was terminated before the time had reached the set stop time due to issues when trying to solve the problem. However, some of the load torque ramp was recorded and can be seen as the speed decreases after 1 second. The system behaves more stable than having a load step change as in Figure 6.24, and the PI controller seems to handle the changes. In Figure 6.31, the load torque is seen to start ramping at 1 second and the machine torque and its reference is seen to follow in order to keep the speed at its reference value. When the simulation stopped, the load torque had reached almost 1.3 Nm which is a bit more than a tenth of the nominal torque. As a quick comparison, it is interesting to notice the differences between having a 500 rpm step and a 1000 rpm step, see Figures 6.28 and 6.30. The angle error, for the 1000 rpm case, peaks at more than twice the peak value of the 500 rpm case.

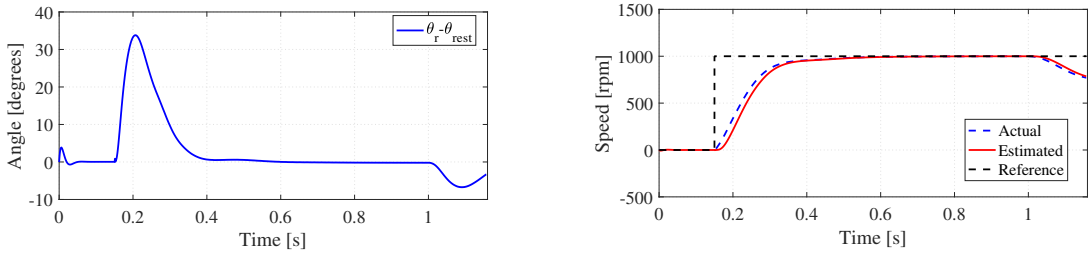

(a) Angle error **(b)** n est. ($n = \frac{60\omega_r}{2\pi n_p}$, speed).

Figure 6.30: Angle and speed estimation during a 1000 rpm step and a ramped load torque (5 Nm/s). $V_{HF} = 10$ V and $f_{HF} = 600$ Hz. $\alpha_{PI} = \omega_{HF}/40$, $\alpha_{sc} = \alpha_{PI}/7$.

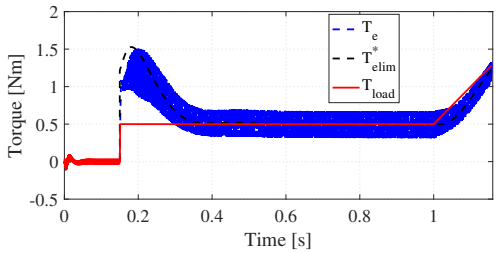

Figure 6.31: Developed torque, its reference and the load torque.

The slope was increased twofold, having 10 Nm/s from the time instant of 1 second and the results are given in Figures 6.32 and 6.33. The same issue was encountered here, the simulation was stopped a bit too early by the software due to solver issues. However, the recorded results are still interesting as it is seen that the method seems to keep stable even for a slope of 10 Nm/s. It should be noted that the load torque only reaches 1.5 Nm, see Figure 6.33, which is relatively low. Also, the angle error in Figure 6.32a, during the load ramp, seems to be a bit higher in magnitude than in Figure 6.30a. Further, the developed torque and its reference are seen to lag the load torque a bit but tries to keep up with it. As before, the ripple in the torque is due to the switching and the signal injection but it does not seem to affect the rotor speed.

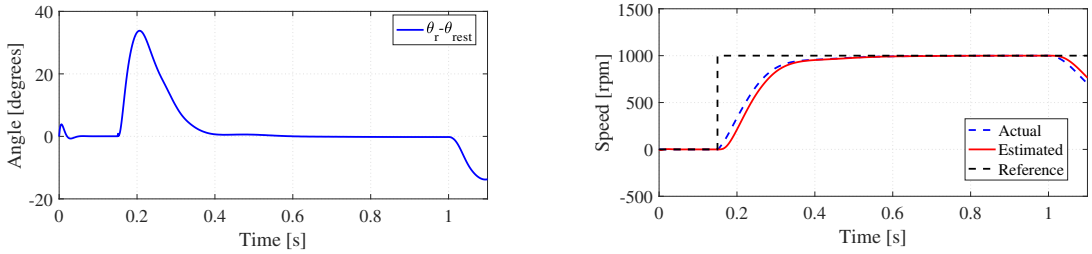

(a) Angle error **(b)** n est. ($n = \frac{60\omega_r}{2\pi n_p}$, speed).

Figure 6.32: Angle and speed estimation during a 1000 rpm step and a ramped load torque (10 Nm/s). $V_{HF} = 10$ V and $f_{HF} = 600$ Hz. $\alpha_{PI} = \omega_{HF}/40$, $\alpha_{sc} = \alpha_{PI}/7$.

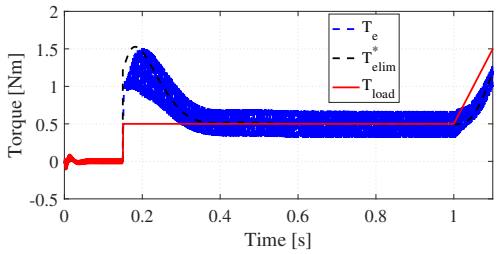

Figure 6.33: Developed torque, its reference and the load torque.

As a last test, the load torque slope was increased to 25 Nm/s and the results are seen in Figures 6.34, 6.35, 6.36, and 6.37. The system becomes unstable but the torque and its reference are still seen to follow the load torque ramp. The amplitude of the machine torque ripple is seen to increase, probably due to the increasing angle error magnitude. The reason why there is a step change in the load torque at approximately 1.1 seconds is because of the sign-dependence of the speed in the load model. The load torque reaches 7 Nm at the end, see Figure 6.36, which is higher than the other two ramped load torque cases. The unstable behaviour seems to start quite early in the ramp (perhaps even right after 1 second), see Figure 6.35, and the sudden change of the load torque, due to the sign change of the speed, causes even more ripple. However, the fast change in speed is due to the low moment of inertia. With a faster changing load torque, the acceleration changes faster and the system might become unstable. The angle estimator is probably too slow compared with the mechanical system. A conclusion of these tests is that the implemented signal injection estimation based control system might not handle sudden load changes well due to the low inertia of the system. However, there are indications that it might handle slower load changes and keep stable. It should also be noted that another test was done, having 10 Nm/s at 0.7 seconds instead, to see if the load torque ramp would finish at a higher value but the simulation was interrupted before the set time stop due to solver issues.

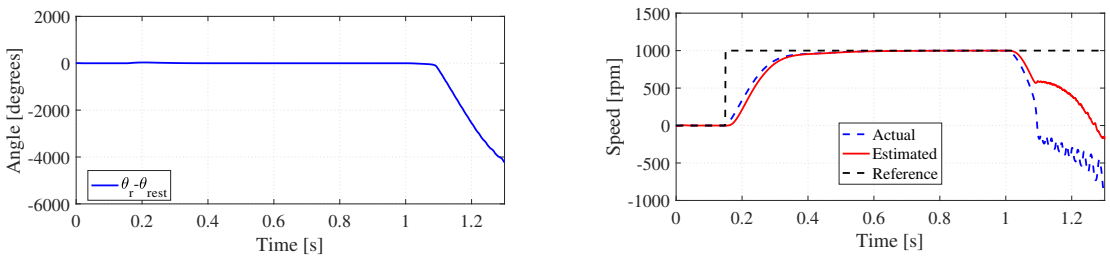

(a) Angle error

(b) n est. ($n = \frac{60\omega_r}{2\pi n_p}$, speed).

Figure 6.34: Angle and speed estimation during a 1000 rpm step and a ramped load torque (25 Nm/s). $V_{HF} = 10$ V and $f_{HF} = 600$ Hz. $\alpha_{PI} = \omega_{HF}/40$, $\alpha_{sc} = \alpha_{PI}/7$.

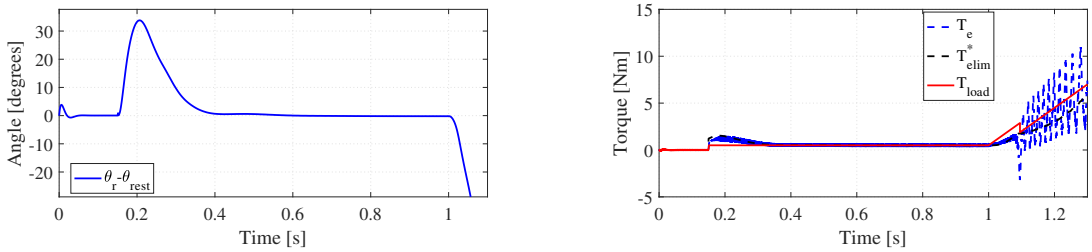

(a) Angle error (zoomed) **(b)** Torque

Figure 6.35: Zoomed angle error and torque.

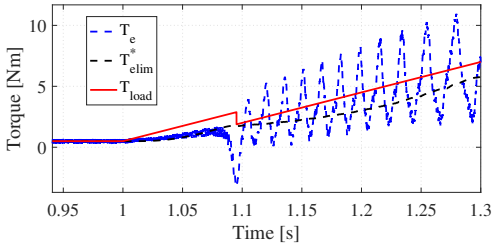

Figure 6.36: Developed torque, its reference and the load torque (zoomed).

In Figure 6.37, the actual dq-current in the machine and the incremental inductance difference found in (5.12) are plotted. It is seen that both exhibit an oscillatory behaviour as the actual motor speed. The speed determines the current derivative and the current determines the torque which in turn makes the rotor spin, so the oscillations are affected by both the current and the speed. The oscillations in the incremental inductances are due to the oscillations in the currents since the inductances are modelled as current-dependent. The loss of control of the currents make it build up and the inductance difference become negative during the short time interval at around 1.25 seconds and 1.27 seconds. Due to the short time intervals, no dramatic change is seen in the angle error in Figure 6.34a except possibly small oscillations.

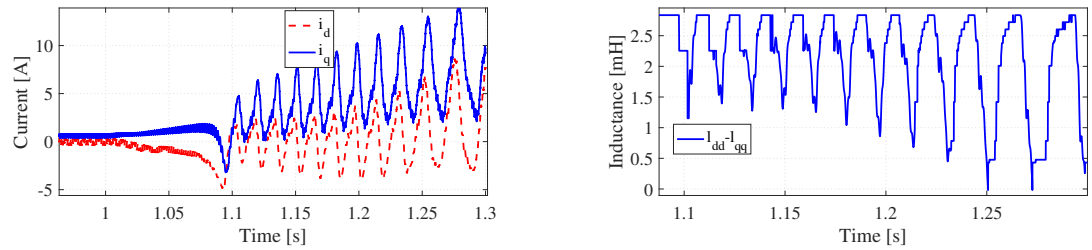

(a) Machine current **(b)** $l_{dd} - l_{qq}$

Figure 6.37: Current and incremental inductance difference that determines the amplitude of the error signal.

6.2.7 Speed Limit Tests

From the results of Section 6.2.6 it is obvious that the system handles at least 1000 rpm. In this section, the speed limit of the signal injection based control system is to be found. Hence, as a first simulation, a step of 1500 rpm was applied having the static and kinetic loads equal. The initial rotor angle was also put to zero. The results are seen in Figures 6.38 and 6.39. The system is seen to become unstable and the rotor angle estimation error ramps seemingly uncontrollably with a negative slope, see Figure 6.38a. In Figure 6.38b the actual speed is seen to oscillate while it increases towards the reference and in Figure 6.39a, the angle error is seen to oscillate and peak at around 100 degrees which is high. At about 0.25 seconds, the inductance difference, see Figure 6.39b, is seen to become negative and the angle error is still positive. This makes the error signal to the PI controller negative which makes the controller to act as if the angle error in fact is negative, i.e. it thinks that the estimated angle is larger than the actual angle. That would make the PI controller to control the error towards zero, thus decreasing the estimated angle. That is why the angle error increases again. Hence, the oscillations in the angle error is due to the negative inductance difference. Also, the large angle error would make the actual currents different from what they are controlled to be. In Figure 6.40, the actual dq-currents in the machine are seen. The current controllers can not control the currents properly since the angle error is large. The beginning of this unstable behaviour might be due to the higher current needed to reach the higher speed reference. This would give more torque and a higher acceleration than for lower speed references. The PI-controller could be too slow to follow the change in speed which gives an increasing angle error. The angle error then gives rise to a higher d-current which would affect the inductance difference. The negative inductance difference then makes the estimation unstable.

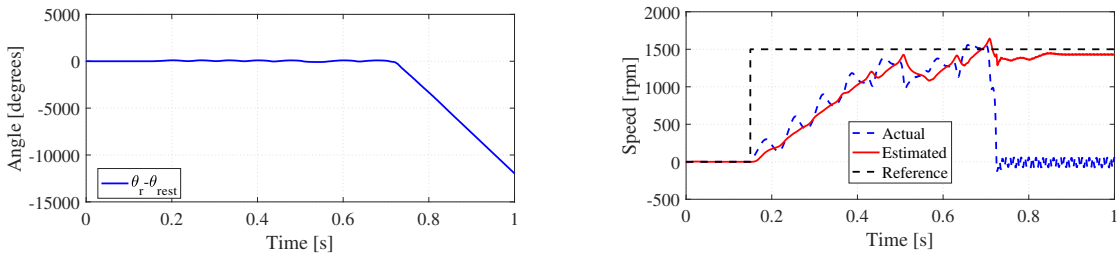

(a) Angle error.

(b) n est. ($n = \frac{60\omega_r}{2\pi n_p}$, speed).

Figure 6.38: Angle and speed estimation during a 1500 rpm step. $V_{HF} = 10$ V and $f_{HF} = 600$ Hz. $\alpha_{PI} = \omega_{HF}/40$, $\alpha_{sc} = \alpha_{PI}/7$.

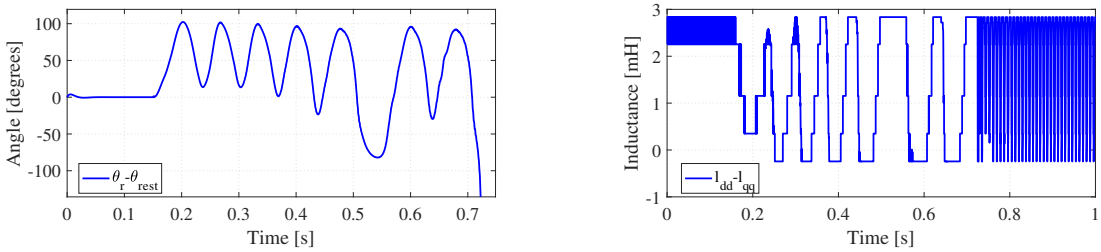

(a) Angle error (zoomed) **(b)** $l_{dd} - l_{qq}$

Figure 6.39: Zoomed angle error and the dynamic inductance difference that is included in the error signal.

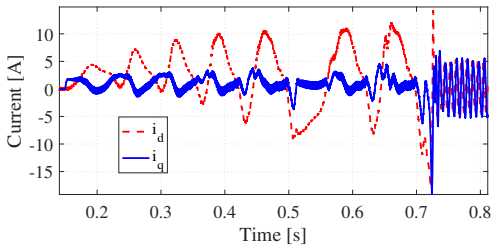

Figure 6.40: Actual dq-currents in the machine.

The 1500 rpm step was seen to fail while the system seems to cope well with a 1000 rpm step as in e.g. Figure 6.30. In the next simulation, the speed was stepped to 1000 rpm and then ramped with 2000 rpm/s at the time instant of 1 second. The simulation did not finish the set time due to solver issues but it is interesting to see that the actual motor speed almost reached 1500 rpm and kept stable before the simulation shut down, see Figure 6.41.

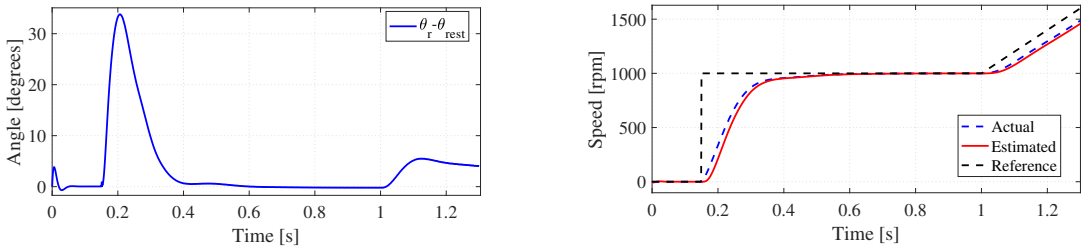

(a) Angle error. **(b)** n est. ($n = \frac{60\omega_r}{2\pi n_p}$, speed).

Figure 6.41: Angle and speed estimation during a 1000 rpm step and a ramp of 2000 rpm/s. $V_{HF} = 10$ V and $f_{HF} = 600$ Hz. $\alpha_{PI} = \omega_{HF}/40$, $\alpha_{sc} = \alpha_{PI}/7$.

A last speed limit test was done having a 1000 rpm step at 0.15 seconds and a 5000 rpm/s slope at 1 second. The results are seen in Figure 6.42 and they are indicating that the system keeps stable when ramping the speed. The actual rotor speed ended up at just around 2070 rpm. The angle error is seen to start to oscillate as the speed

becomes high which could be the beginning of unstable behaviour but since the simulation stopped it is difficult to tell. A thorough analysis regarding for which ramp magnitudes the system keeps stable has not been conducted but it seems that the system can handle speed up to 2000 rpm with a ramp. Above 2000 rpm it seems that the angle error starts to oscillate. One explanation behind this speed limit could be that in the derivation of this method it was assumed that the injected frequency is so high that other frequency dependent signals is seen as constant, see (5.5). However, for an electrical speed corresponding to 2000 rpm, the ratio between the injected frequency and the rotor speed is 3.6 (i.e. the injected frequency is only 3.6 times larger than the rotor speed). According to [52], the high frequency signal injection methods have a relatively low speed range, and no numbers are given for this range. However, in this test, it was seen that the signal injection method seems to be able to estimate the position up to about a third of the nominal speed (6000 rpm) when ramping the speed reference. As a conclusion, the system does not seem to tolerate high enough speed steps but can at least manage a 1000 rpm step and the speed limit seems to be reached at 2000 rpm.

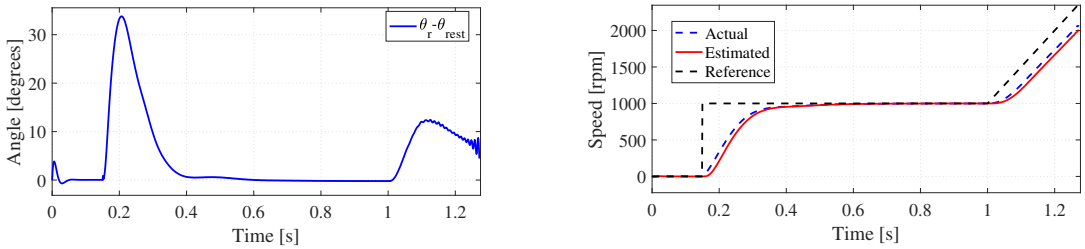

(a) Angle error.

(b) n est. ($n = \frac{60\omega_r}{2\pi n_p}$, speed).

Figure 6.42: Angle and speed estimation during a 1000 rpm step and a ramp of 5000 rpm/s. $V_{HF} = 10$ V and $f_{HF} = 600$ Hz. $\alpha_{PI} = \omega_{HF}/40$, $\alpha_{sc} = \alpha_{PI}/7$.

6.2.8 Testing Different Static Loads

The high frequency signal injection method was further tested by increasing the static friction load C (emulating high static friction loads due to e.g. loose iron or concrete pieces, blocking the rotor inside the drilled hole) and trying to step the speed reference. The kinetic friction load was set to equal the static friction here as well.

The static load (and thus the kinetic load) was first set to 13 Nm which is enough to have a static load torque higher than the nominal torque. This forces the machine to standstill while trying to control the speed to 1000 rpm. The speed reference step was applied at 0.15 seconds. The position estimation error is shown in Figure 6.43a and when steady-state is reached after the speed step, the steady-state estimation error is about 0.774 electrical degrees. Before the step, the steady-state error is about 0.04 degrees. The step is seen to cause, briefly, higher estimation errors. In Figure 6.43b, it is seen that the actual speed keeps at zero all the time. However, at 0.15 seconds, the estimated speed has some transient due to the speed reference step before the speed is accurately determined rather quickly. Also, the

machine is seen to try to develop enough torque to overcome the static load torque of 13 Nm but is not able to do that. This is why the torque ramps and become high, shown in Figure 6.44a where the actual machine torque is plotted against the limited torque reference. In Figure 6.44 it can be seen that the inductance-dependent reluctance torque is causing the shape of the machine torque at steady-state seen in Figure 6.45a. Further, the developed machine torque has a ripple caused by the inverter switching, seen in Figure 6.45b. The current to the machine increases as the switches turns on and decreases as the switches turns off, and this affects the developed torque in the machine. This is what is seen also in Section 6.2.6.

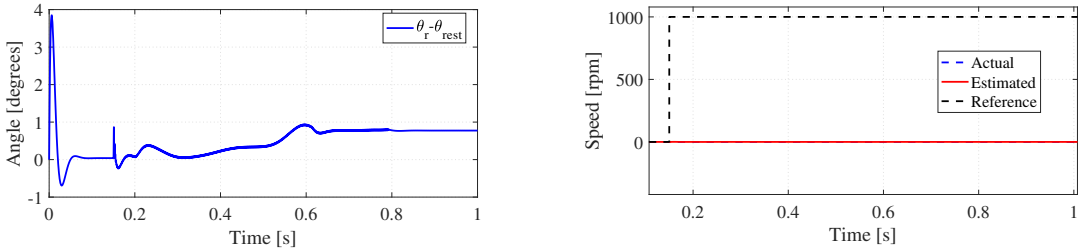

(a) Angle error. **(b)** n est. ($n = \frac{60\omega_r}{2\pi n_p}$, speed).

Figure 6.43: Angle and speed estimation during 13 Nm static load, having $V_{HF} = 10$ V and $f_{HF} = 600$ Hz. $\alpha_{PI} = \omega_{HF}/40$, $\alpha_{sc} = \alpha_{PI}/7$.

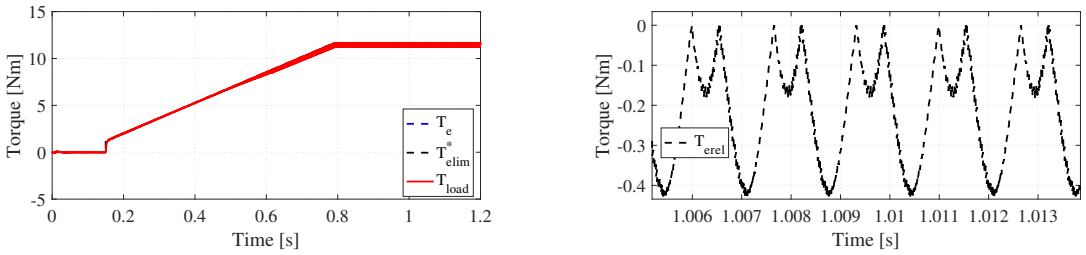

(a) Machine torque and reference **(b)** Reluctance torque

Figure 6.44: Developed torque during 13 Nm static load.

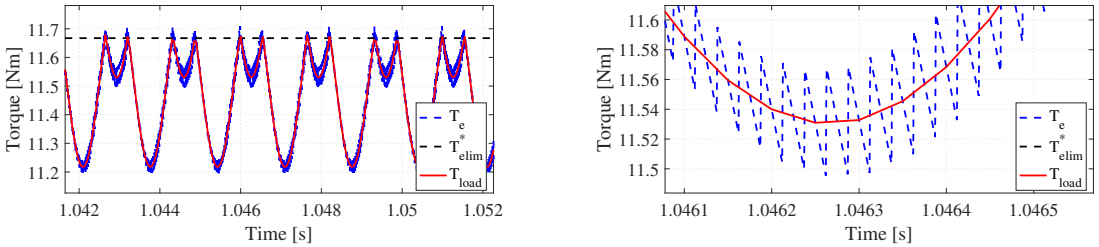

(a) Zoomed **(b)** More zoomed

Figure 6.45: Electrical torque versus its reference (zoomed).

Having tried to increase the static friction so that the rotor can not move, the next tests investigates how well the system works when the static load is high but lower than the nominal torque, making it possible for the machine to accelerate in theory. The speed reference is set to 1000 rpm while the static load is changed to 2 Nm and 5 Nm respectively. The dynamic load is set equal to the static load as before.

In Figures 6.46 and 6.47, the static load was put to 2 Nm and it is seen that the machine is able to produce enough torque to overcome the static friction and start to accelerate. The estimation process is successful and there is a steady-state angle estimation error of approximately 1.25 degrees, see Figure 6.46a. The friction load changes from static to kinetic as the electric torque surpasses the static friction torque and the rotor starts rotating, see Figure 6.46a and Figure 6.47b. However, both the static and kinetic load torque are equal. As soon as the machine is able to rotate, the load torque changes sign due to the sign-dependence of the speed. Therefore, there are some minor speed oscillations around zero as the machine starts to spin. The ripple in the machine torque, see Figure 6.47, is due to the angle error and the inverter switching as for earlier simulations, see e.g. the results of Section 6.2.6.

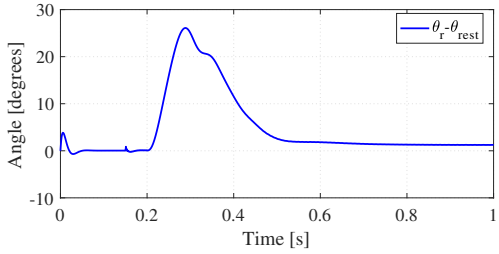

(a) θ_r est. (electrical degrees).

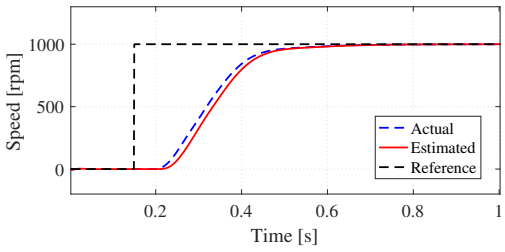

(b) n est. ($n = \frac{60\omega_r}{2\pi n_p}$, speed).

Figure 6.46: Angle and speed estimation during 2 Nm static load.

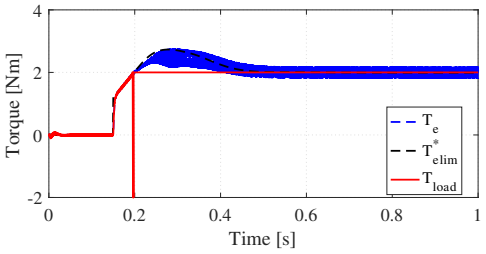

(a) Electrical torque versus load torque.

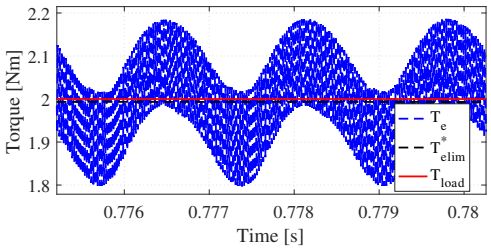

(b) Electrical torque versus load torque (zoomed).

Figure 6.47: Torque development during 2 Nm static load.

In Figures 6.48 and 6.49, the static load was set to 5 Nm and it is seen that also for this case the machine is able to produce enough torque to overcome the static friction and start to accelerate. The steady-state error is about 0.23 degrees when the machine has reached 1000 rpm, see Figure 6.48a. Although the load is quite

high, the system manages to remain stable and the rotor is able to move. However, there is an overshoot of the speed which is related to the reference torque from the speed controller. It is seen that the torque developed, see Figure 6.49, in the machine needs some time to settle as it has overcome the static load. It is believed that since the machine has not moved before, the speed controller tries to output a higher torque to try to accelerate the rotor. As it does so, the rotor starts spinning eventually and the relatively slow speed controller lowers the torque reference. The speed is seen to overshoot. One should remember that the angle error, which peaks at above 20 degrees but keeps high during a little longer time than for the 2 Nm case, is part of the behaviours seen since the controller can not control the currents perfectly anymore. As for the 2 Nm static load case, see Figure 6.47, there are two components in the torque, one due to inverter switching and one due to the signal injection in conjunction with the angle estimation error.

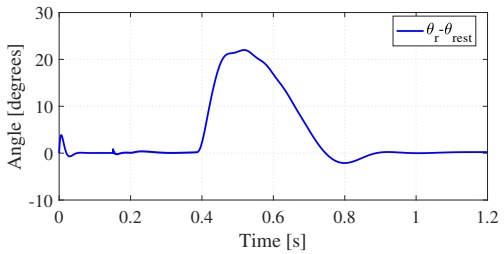

(a) Angle error.

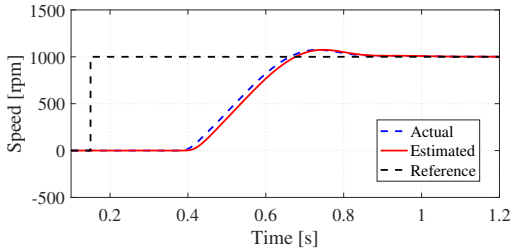

(b) n est. ($n = \frac{60\omega_r}{2\pi n_p}$, speed).

Figure 6.48: Angle and speed estimation (5 Nm static load).

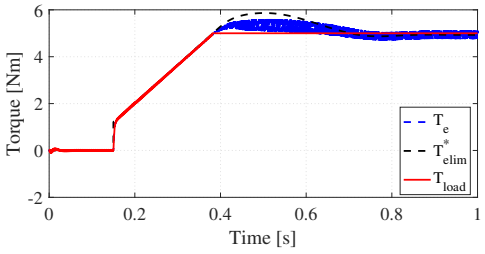

(a) Electrical torque versus load torque.

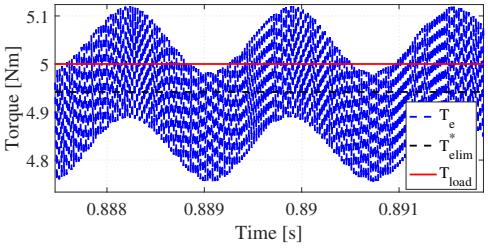

(b) Electrical torque versus load torque (zoomed).

Figure 6.49: Torque development with 5 Nm static load.

6.2.9 Comparison with SCVM

A comparison between the signal injection method above and the SCVM, earlier mentioned in Section 5.2, is presented here. The results of the SCVM are first presented and are then compared with the corresponding case for the signal injection scheme. The settings for the controllers are a bit different from the signal injection simulations above in order to have a functioning SCVM, with $\alpha_{cc} = 3000$ rad/s and

$\alpha_{sc} = 10$ rad/s. Also, $\lambda = 2$ and the initial rotor angle was set to zero for all SCVM tests. These values were chosen after initial testing.

First, the SCVM is verified to work up to rated speed (6000 rpm) with the static load torque selected as 0.5 Nm and having the kinetic torque set as $\mu_d mgr/k$ when the rotor turns. The speed limit for the lowpass filter in the SCVM, ω_{lim} (rad/s), was set to 400 rpm after initial tests indicated that this would work. The results are seen in Figure 6.50. This was done to verify that the SCVM can handle the discontinuity in the load model. The steady-state angle error is about -1.14 degrees. The machine is seen to reach the speed reference nicely.

Further, in Figure 6.51 the SCVM is also seen to handle a constant load torque of 0.5 Nm, i.e. having the static and kinetic torque equal each other. The steady-state angle estimation error is about -1.28 degrees and the machine goes towards the speed reference. For both tests, the speed reference was set at 1 ms.

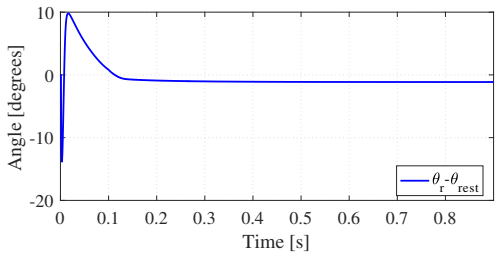

(a) Angle error

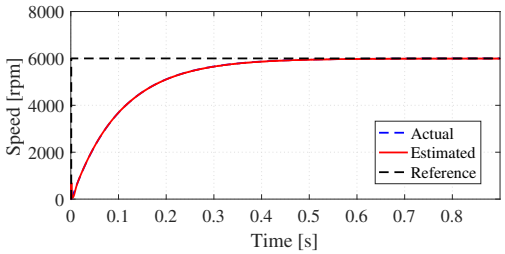

(b) n est. ($n = \frac{60\omega_r}{2\pi n_p}$, speed).

Figure 6.50: Estimation of speed using SCVM having 6000 rpm reference speed, $\omega_{lim} = \frac{2\pi 400 n_p}{60}$ rad/s. Static and kinetic load unequal.

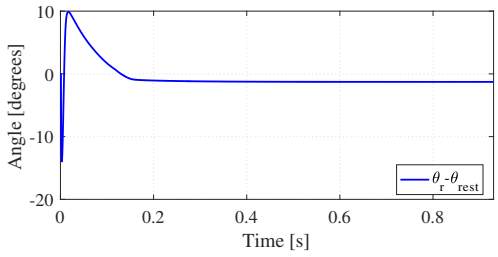

(a) Angle error

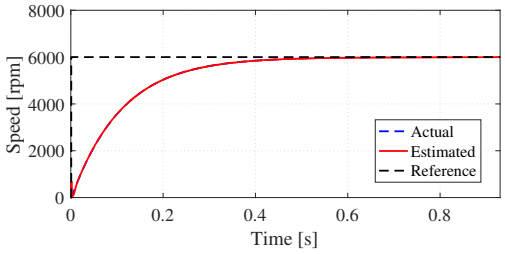

(b) n est. ($n = \frac{60\omega_r}{2\pi n_p}$, speed).

Figure 6.51: Estimation of speed using SCVM having 6000 rpm reference speed, $\omega_{lim} = \frac{2\pi 400 n_p}{60}$ rad/s. Static and kinetic load equal.

As an example of how the performance might get affected by the speed limitation in the lowpass filter of the SCVM, a simulation was done where the speed limit was lowered to 100 rpm. This means that for speeds lower than 100 rpm, the leakage term coefficient will be speed dependent. However, for speeds above the limit, the term is constant, $\lambda\omega_{lim}$. The results are seen in Figure 6.52 and the simulation was stopped earlier by the software due to solver issues as for previous simulations. The only difference between the case in Figure 6.51 and this case is the change from a

speed limitation of 400 rpm to 100 rpm and the performance differences are clearly visible in Figure 6.52. It is seen that the estimation seems to fail shortly at 0.05 and 0.13 seconds when reaching almost 2000 rpm and 4000 rpm respectively. The estimation suddenly drops and the angle error increases dramatically. It is also seen that after a fast decline in the estimation, the speed is better estimated again and the angle error reaches a new level after 0.05 seconds and 0.13 seconds respectively. It is difficult to explain why this happens since the SCVM depends on the output of the controllers which in turn depends on the output of the SCVM, but when looking at Figure 6.52a, the angle error is seen to increase as the time goes towards 0.05 seconds. As in Figure 6.51a, the angle error increases during the speed ramping.

A further investigation was made using a simpler machine model having the incremental and absolute inductances equal and static, and no cross-coupled inductances. This was done to see if the machine model was the cause behind these estimation errors. The speed limitation was set to 100 rpm as well and the results are seen in Figures 6.53a to 6.55. It is seen that the same behaviour has appeared, see e.g. Figures 6.53a and 6.53b where the angle error is seen to increase and the estimated speed is seen to decrease as spikes. Thus, this has nothing to do with the machine model. It seems to be a pure SCVM problem. In Figure 6.54a it is seen that the angle error seems to increase with 360 degrees during each spike. This is also visible in Figures 6.54b and 6.55 where the torque and the currents are changing signs. The torque reference is seen to increase during a spike, see Figure 6.54b. This is probably since the estimated speed decreases quickly, so the speed controller tries to increase the torque reference so that the speed is controlled towards its reference. Since the speed limitation makes the $\widehat{e}_d$ term in (5.15) to decrease earlier now than for the 400 rpm speed limit case, this is believed to be the reason behind the spikes in the estimation of the speed. As the speed decreases below the speed limitation, the leakage term coefficient increases again and the estimation seems to recover. Since the SCVM is seen to work satisfactorily with a speed limitation of 400 rpm, see e.g. Figure 6.51, this is to be used for the rest of the simulations.

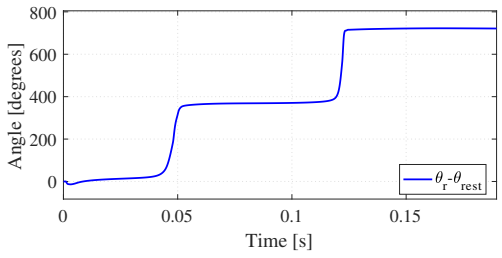

(a) Angle error

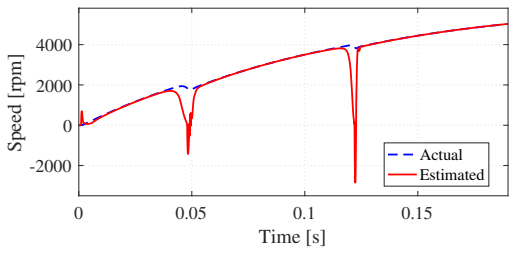

(b) n est. ($n = \frac{60\omega_r}{2\pi n_p}$, speed).

Figure 6.52: Estimation of speed using SCVM having 6000 rpm reference speed, $\omega_{lim} = \frac{2\pi 100 n_p}{60}$ rad/s. Static and kinetic load equal.

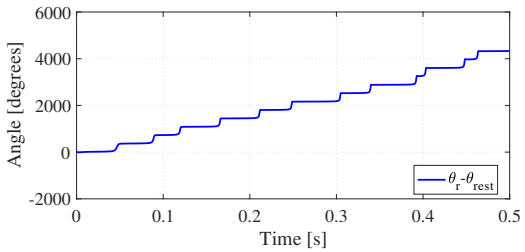

(a) Angle error

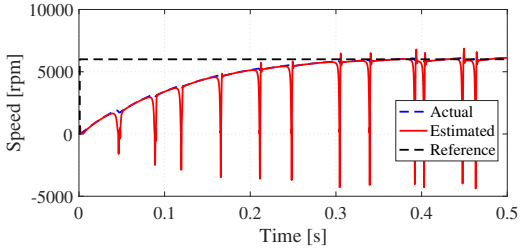

(b) n est. ($n = \frac{60\omega_r}{2\pi n_p}$, speed).

Figure 6.53: Estimation of speed using SCVM having 6000 rpm reference speed, $\omega_{lim} = \frac{2\pi 100 n_p}{60}$ rad/s. Simpler machine model.

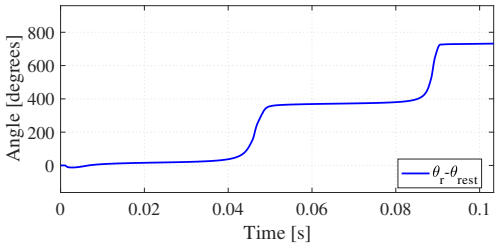

(a) Angle error (zoom)

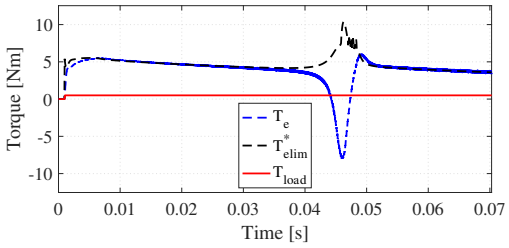

(b) Torque

Figure 6.54: Zoomed in angle error figure and the torque during the speed increase.

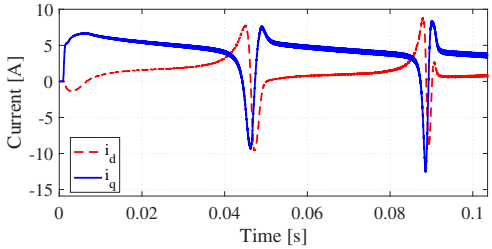

Figure 6.55: Actual dq-currents.

The SCVM was tested for different static friction loads as was done with the signal injection method having a speed reference of 1000 rpm at 0.001 seconds and an initial rotor angle of 0 degrees. For all static load tests, the dynamic load was set equal to the static load as was done for the signal injection tests. In Figure 6.56 the static friction load is 2 Nm and it is seen that the SCVM works fine since the machine is able to rotate and reaches its reference speed. The steady-state angle error is about -0.73 degrees. However, as seen at steady-state and in Figure 6.57a, the angle estimation error has a ripple. Since, no actual machine signals are measured, except the $\alpha\beta$-current, the SCVM is dependent only on the dq-current and dq-voltage reference signals (in the estimated dq-frame). These depend on the rotor angle estimation error, so trying to determine the source of this ripple is

difficult. Further, the almost instantaneous angle error step when the speed reference is stepped at 1 ms is probably due to the neglected current derivatives in (5.16). When i_q is stepped to overcome the static load torque, see Figure 6.57b, this change is not taken into account when estimating the back-emf which results in an error. This estimation error is then integrated. As the rotor speed becomes nonzero, the leakage term in (5.15) becomes nonzero. In Figure 6.56a, it is seen that as the rotor starts turning, the estimation error decreases.

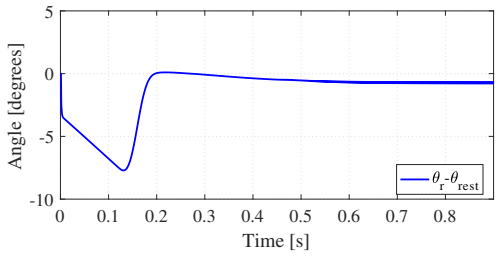

(a) Angle error

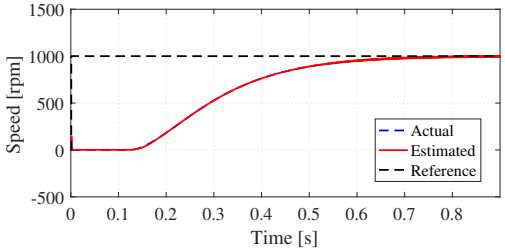

(b) n est. ($n = \frac{60\omega_r}{2\pi n_p}$, speed).

Figure 6.56: Estimation of position and speed having 1000 rpm reference speed using SCVM, $\omega_{lim} = \frac{2\pi 400 n_p}{60}$ rad/s, $\alpha_{sc} = 10$ rad/s, $\alpha_{cc} = 3000$ rad/s, and $C = 2$ Nm.

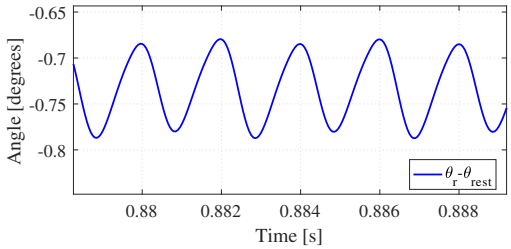

(a) Angle error (zoomed in).

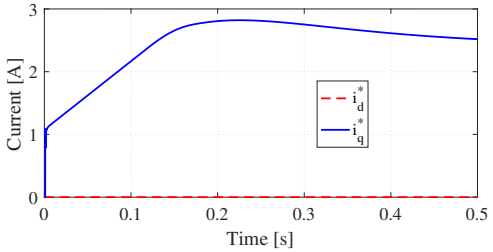

(b) Current reference.

Figure 6.57: Angle error investigation, SCVM (2 Nm static load).

When increasing the static load to 5 Nm, the SCVM is still able to estimate the speed and position of the rotor, as seen in Figure 6.58 but now, the steady-state error is about 9.47 degrees and the angle error is seen to increase in magnitude worse than in Figure 6.56a. This is due to the same principle discussed earlier, the increasing currents make the angle estimation at standstill worse as the torque is developing in order to overcome the static load, see Figure 6.59. The actual machine dq-current looks a bit different compared to the reference current. This is due to the angle estimation error. There is also a ripple in the actual current, this is due to the inverter switching as discussed earlier.

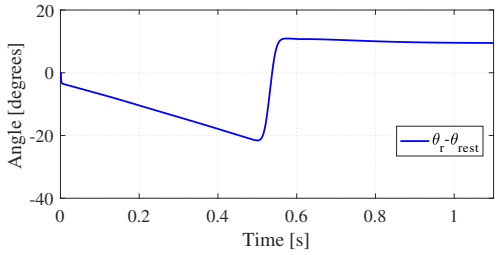

(a) Angle error.

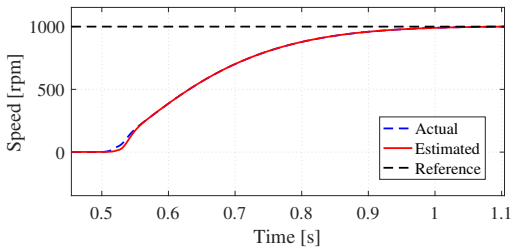

(b) n est. ($n = \frac{60\omega_r}{2\pi n_p}$, speed).

Figure 6.58: Estimation of position and speed having 1000 rpm reference speed using SCVM, $\omega_{lim} = \frac{2\pi 400 n_p}{60}$ rad/s, $\alpha_{sc} = 10$ rad/s, $\alpha_{cc} = 3000$ rad/s, and $C = 5$ Nm.

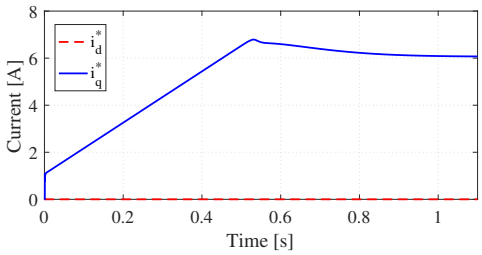

(a) Reference.

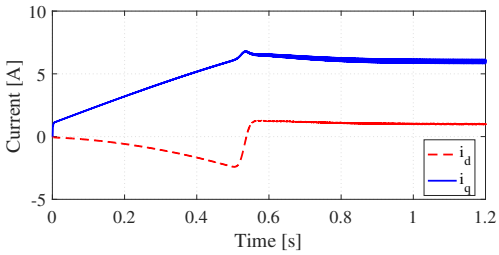

(b) Actual.

Figure 6.59: Current references and actual machine dq-currents.

In Figure 6.60, the torque reference, the machine torque and the load torque is seen for this case with static load of 5 Nm. At steady-state there is a ripple in the machine torque due to the inverter switching, see Figure 6.60b. As the machine torque overcomes the static load of 5 Nm, there is a sign change in the load torque during a very short time span. This is due to the speed-sign dependence of the load model, see (2.20), and that the speed is oscillating a little before it starts to ramp towards its reference. The sudden decreasing step in the torque just before 0.4 seconds is due to a step change in the absolute inductances that influences the developed reluctance torque in the machine, see Figure 6.61. The absolute inductances are dependent on the machine dq-current levels which are switched (as mentioned earlier), this results in some ripple in the inductances as well.

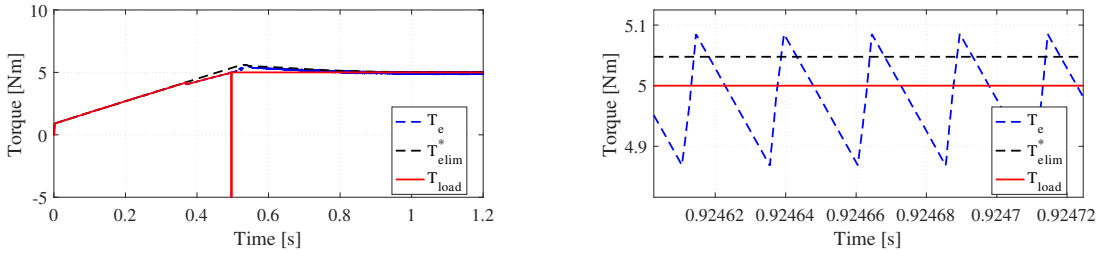

(a) Torque. **(b)** Torque (zoomed in).

Figure 6.60: Developed torque, reference torque and load torque.

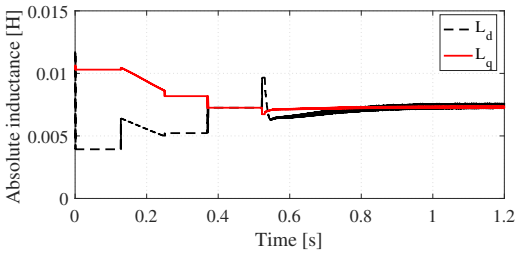

Figure 6.61: Absolute inductances.

As a conclusion, the SCVM is compared with the signal injection method when the rotor is completely stuck having a static friction load of 13 Nm, see Figure 6.62. The angle error is declining during the whole simulation. This is since the machine draws a high current to overcome the load but does not move. This makes the estimation in the SCVM to fail. The developed torque reaches almost 6 Nm (see Figure 6.63a) due to the actual negative d-current (see Figure 6.63b), which is the result of the wrongly estimated angle. The negative d-current makes it possible for the reluctance torque, visualized in Figure 6.64a, to decrease the total machine torque from its peak after almost 0.8 seconds. The steps in the developed torque are seen to be from the reluctance torque and ultimately from the absolute d- and q-inductance of the machine, plotted in Figure 6.64b. The q-inductance is seen to decrease as the q-current increases while the d-inductance increases with decreasing d-current. This is probably due to saturation and flux levels. The ripple seen in the torque seems to be inherited from the inductances as they are seen there as well. However, looking in Figure 6.65, the ripple is zoomed in and it is seen that the ripple is more like spikes. The reason behind these spikes might be due to the inverter switching.

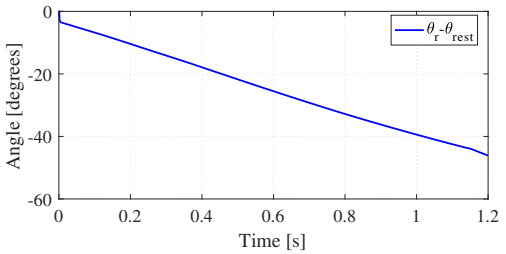

(a) Angle error

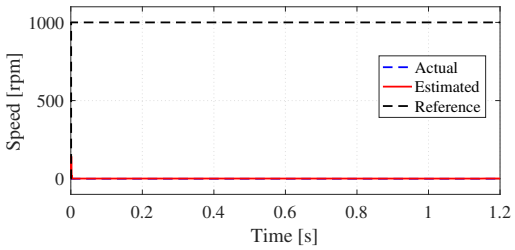

(b) n est. ($n = \frac{60\omega_r}{2\pi n_p}$, speed).

Figure 6.62: Position and speed estimation, 1000 rpm reference speed using SCVM, $\omega_{lim} = \frac{2\pi 400 n_p}{60}$ rad/s, $\alpha_{sc} = 10$ rad/s, $\alpha_{cc} = 3000$ rad/s, and 13 Nm static load.

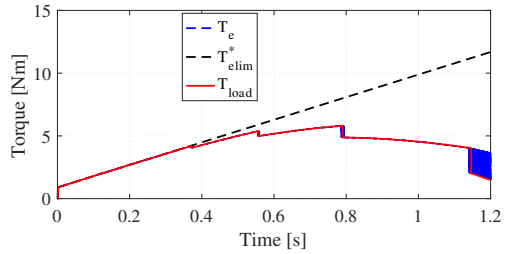

(a) Torque versus limited reference torque

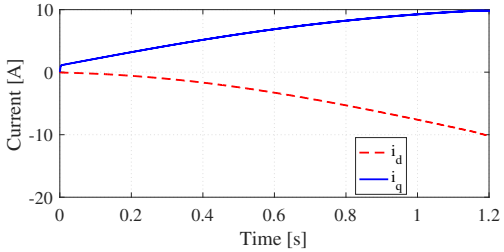

(b) Actual dq-current

Figure 6.63: Torque and currents when trying to start the machine.

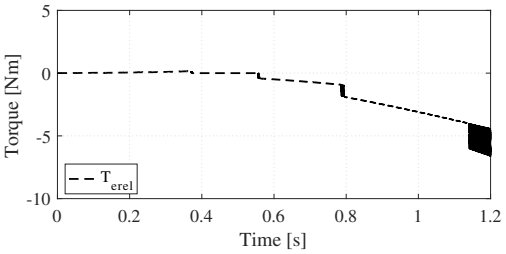

(a) Reluctance torque

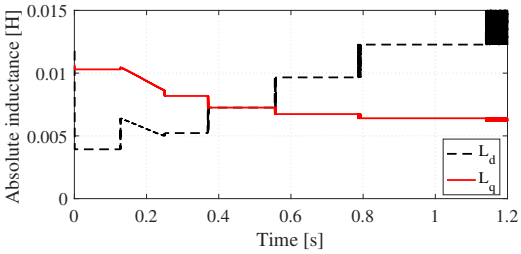

(b) Absolute dq-inductances

Figure 6.64: Reluctance torque and absolute inductances.

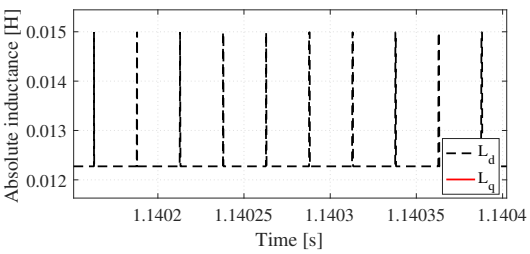

Figure 6.65: Absolute dq-inductances (zoomed)

Although the machine is forced to standstill by the high static load for both methods, it is evident that the signal injection method has a better estimation performance than the SCVM, compare especially the 5 Nm case (Figures 6.48 and 6.58) and the 13 Nm case (Figures 6.43 and 6.62). For the 13 Nm case, the differences are most evident, the signal injection based system manages to keep a constant steady-state angle error while the error for the SCVM keeps growing negative. The larger angle error of the SCVM is due to the neglected current derivatives in the estimation of the back-emf. The maximum torque that the machine produces was about 11 Nm for the signal injection while it reached about 6 Nm for the SCVM before it also declined.

As a last test, the resistance used in the SCVM was overestimated with 10% for when having 2 Nm and 9 Nm static load and the results are seen in Figures 6.66 and 6.67. Comparing Figure 6.56a (perfect estimation of the stator resistance) and Figure 6.66a there are differences. When having a perfect estimation of the resistance, the angle error is negative before going towards zero as the rotor starts turning, as seen in Figure 6.56a. In Figure 6.66a The angle error first becomes negative and then turn positive before it declines towards zero as the rotor starts spinning. So, the instantaneous drop in angle error is, as has been discussed earlier, due to the neglected current derivatives. Then, the back-emf error is integrated and when the resistance is 10% overestimated, it seems that the angle error goes positive. An overestimation of the resistance might change the sign of the estimated back-emf according to (5.16) and this could explain the reason behind the sign-change of the angle error seen in Figure 6.66a compared with Figure 6.56a. As the static load increases to 9 Nm and the stator resistance is still overestimated, the angle error becomes even worse, see Figure 6.67. It is interesting to see the difference between Figure 6.62a where the static load torque is 13 Nm and Figure 6.67. The angle error seems to become worse when having less load torque (9 Nm) but a wrongly estimated resistance.

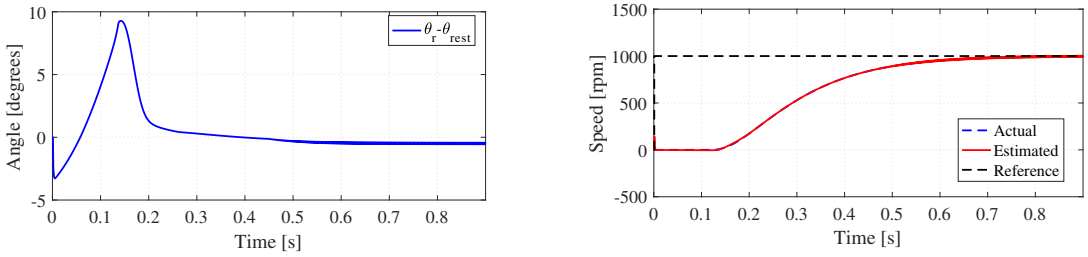

(a) Angle error

(b) n est. ($n = \frac{60\omega_r}{2\pi n_p}$, speed).

Figure 6.66: SCVM, 2 Nm static load and $\widehat{R}_s = 1.1R_s$.

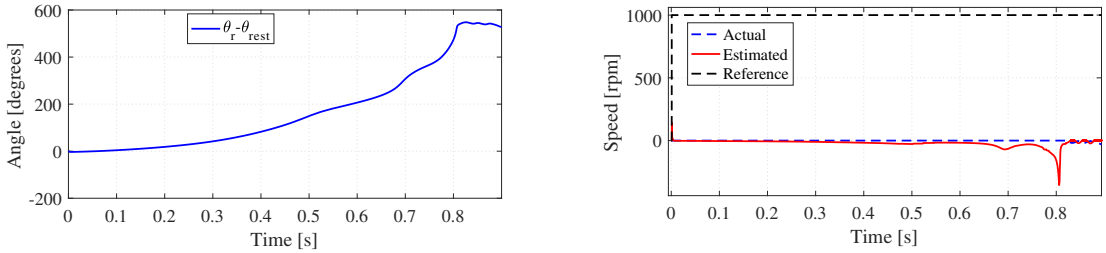

(a) Angle error

(b) n est. ($n = \frac{60\omega_r}{2\pi n_p}$, speed).

Figure 6.67: SCVM, 9 Nm static load and $\widehat{R}_s = 1.1R_s$.

7
Conclusions

The simulations showed both advantages and disadvantages of the chosen methods. The results of the project indicates that a signal injection procedure should be used instead of the SCVM during standstill and low speeds with higher static loads. However, more investigations (such as better inductance measurements) and more realistic simulations should be made in order to see if the procedure actually is feasible to use in reality.

Tests were conducted showing the performance of the signal injection scheme during standstill angle estimation with and without having parameter errors. With a wrongly estimated l_{qd} compensation the steady-state error was more affected than with a wrongly estimated A_e. It was found that A_e affected the peak value during the angle estimation and it did not affect the steady-state error. For the standstill estimations, the signal injection technique [24] is better to use than the SCVM since there is no back-emf.

Also, it was shown that a magnetic pole identification method could be easily implemented and that it gave satisfying results. However, it was only tested for one test case. Thus, further simulations and tests should be done before implementing it in a real drive system.

It was found that the drill may be operated using high frequency signal injection both for standstill and low speeds, up to almost 2000 rpm which is a third of the nominal speed. However, in reality noise may affect the outcome of the estimation process for the high frequency signal injection scheme and may cause problems. The effect of noise was never investigated due to time limitations. Also, the identification of the model parameters may (as have been already stated) have lead to model parameter errors which could affect the results. Further, since the signal injection method tested relies on the dq inductance difference, this method might not perform as well in reality. This should also be noted since there were a few simulation cases when the inductance difference became negative which made the estimation system unstable.

Problems arose when the load changed quickly as the system using signal injection became unstable. However, for ramped loads, there are indications that, for the chosen control parameters, the signal injection method keeps stable. The SCVM was shown to work for static loads up to at least 5 Nm, and it could also be used up to rated speed. However, when the starting load become high enough, the SCVM did not perform as good as the signal injection method. As a shorter investigation, the effects of having an overestimation of the stator resistance for different static loads was also discussed and it was seen that the angle estimation of the SCVM could become worse for higher static loads when the resistance was overestimated

with 10 %.

The signal injection method could be used for other products that are subjected to high static loads as well. However, it is important that the inductance difference is large enough for a large enough operating area in order to minimize the risks of making the system unstable. The SCVM could be used for systems that does not need high starting torque, e.g. saws that are started before cutting, i.e. at no-load conditions. When the system reaches high speeds, the SCVM can estimate the rotor angle and the speed with good accuracy, as was seen in e.g. the 6000 rpm speed step SCVM simulations.

7.1 Future Work

As part of the future work, more simulations should be made before implementation to ensure the stability of the procedures. This could also include better models of the test setup, electrical system and the mechanical system. Some approximations have been made in the modelling, e.g. the flux harmonics have been neglected. These features could be modelled in more extensive simulations. Further, the measurements of the inductances and the resistance should be done in a more precise manner yielding, hopefully, better model verification results. In this thesis, the measurements have some errors which affects these results. These should be minimized using better measurement procedures. Other measurement procedures might also be tested to see if they yield similar results.

The high frequency injection method might not generally be suitable for SPMSMs in reality since the difference in inductances might be small and measurement noise might thus affect the method negatively. This is also yet another reason to do extensive inductance measurements in order to fully investigate whether or not the method is useful in reality.

The estimation methods uses certain injection amplitudes and frequencies. The importance of the choice of these could be further investigated in order to achieve better estimations and decrease the losses and temperature effects.

Also, for the high frequency signal injection scheme, further investigations regarding the bandwidths of the system should be made to enhance the estimation procedure and performance. Due to long simulation times and problems with the solver settings, this was not investigated in detail. This could be a topic of further research, trying to optimize the bandwidths for a certain application.

Further investigations for low frequency signal injection schemes causing rotor vibrations, such as [30], should be made since these could be better to use for SPMSMs as they do not rely upon differences in inductance. This could be a more realistic option to use for SPMSMs rather than the high frequency signal injection scheme investigated in this project. If this is done, an enhanced mechanical model could also be developed taking into account gaps in the gearbox and such.

The possibility to combine the estimates from two different estimation schemes using a transition function, see e.g. [4], should be investigated having high frequency signal injection during standstill and low speeds while having SCVM for higher speeds. Thus, a combination between the signal injection scheme and the SCVM could be realized to achieve sensorless control for the full speed range. As was seen

in this thesis, the SCVM can handle speeds at least up to rated speed but can not be used for standstill estimation while the signal injection method was shown to work properly for standstill and for speeds up to almost 2000 rpm. Hence, a weighting function should be implemented and tested to see if it is possible to combine these two methods for speeds from standstill up to at least rated speed.

Bibliography

[1] G. P. Shultz, *Transformers and Motors*, USA: Elsevier Inc., 1989. [Online]. Available: http://www.sciencedirect.com/science/book/9780080519586.

[2] A. Hughes, and B. Drury, *Electric Motors and Drives: Fundamentals, Types, and Applications*, 4th ed., UK: Elsevier Ltd., 2013.

[3] B. K. Bose, *Power Electronics and Variable Frequency Drives: Technology and Applications*, USA: Wiley-IEEE Press, 1997. [Online]. Available: http://ieeexplore.ieee.org/xpl/bkabstractplus.jsp?bkn=5263964.

[4] L. Harnefors, *Control of Variable-Speed Drives*, Västerås, Sweden: Mälardalen University, 2002.

[5] P.P. Acarnley and J.F. Watson, "Review of position-sensorless operation of brushless permanent-magnet machines," *IEEE Transactions on Industrial Electronics*, vol 53, no. 2, pp. 352-362, Apr, 2006. doi:10.1109/TIE.2006.870868, [Online]. Available: IEEE Xplore Digital Library, http://ieeexplore.ieee.org/Xplore/home.jsp. Accessed: January 25, 2017.

[6] W. Zine *et al.*, "Investigation of saturation impact on an IPMSM saliency-based sensorless control for automotive applications," in *2016 International Symposium on Power Electronics, Electrical Drives, Automation and Motion (SPEEDAM)*, 2016, pp. 1238-1243. [Online]. Available: http://ieeexplore.ieee.org/document/7525831/.

[7] M. Jansson, L. Harnefors, O. Wallmark, and M. Leksell, "Synchronization at startup and stable rotation reversal of sensorless nonsalient PMSM drives," *IEEE Transactions on Industrial Electronics*, vol. 53, no. 2, pp. 379-387, Apr, 2006. doi:10.1109/TIE.2006.870731, [Online]. Available: IEEE Xplore Digital Library, http://ieeexplore.ieee.org/Xplore/home.jsp. Accessed: January 25, 2017.

[8] F. Hedenus, M. Persson, and F. Sprei, *SUSTAINABLE DEVELOPMENT: History, Definition & The Role of the Engineer*, 3rd ed., Gothenburg, Sweden, 2016. [Online]. Available: http://publications.lib.chalmers.se/publication/230705-sustainable-development-history-definitions-and-the-role-of-the-engineer. Accessed: January 24, 2017.

[9] P.C. Dent, "Rare earth elements and permanent magnets (invited)," *Journal of Applied Physics*, vol. 111, no. 7, pp. 07A721 - 07A721-6, Mar., 2012. doi:10.1063/1.3676616, [Online]. Available: AIP Publishing, http://aip.scitation.org. Accessed: January 30, 2017.

[10] J. Wübbeke, "Rare earth elements in China: Policies and narratives of reinventing an industry," *Resources Policy*, vol. 38, no. 3, pp. 384-394, Sept,

2013. doi:10.1016/j.resourpol.2013.05.005, [Online]. Available: ScienceDirect, http://www.sciencedirect.com. Accessed: January 30, 2017.

[11] J. Pyrhönen, T. Jokinen, and V. Hrabovcová, *Design of Rotating Electrical Machines*, 2nd ed., Chichester, United Kingdom: John Wiley & Sons Ltd, 2014.

[12] M. Seilmeier, S. Ebersberger, and B. Piepenbreier, "PMSM model for sensorless control considering saturation induced secondary saliencies," in *2013 IEEE International Symposium on Sensorless Control for Electrical Drives and Predictive Control of Electrical Drives and Power Electronics (SLED/PRECEDE)*, 2013, pp. 1-8. [Online]. Available: http://ieeexplore.ieee.org.proxy.lib.chalmers.se/document/6684519/. Accessed: March 28, 2017.

[13] G. Pellegrino, T.M. Jahns, N. Bianchi, W. Soong, and F. Cupertino, *The Rediscovery of Synchronous Reluctance and Ferrite Permanent Magnet Motors: Tutorial Course Notes*, Springer International Publishing, 2016.

[14] B.G. Rabbat and H.G. Russell, "Friction Coefficient of Steel on Concrete or Grout," *Journal of Structural Engineering*, vol. 111, no. 3, pp. 399-405, March, 1985. doi:http://dx.doi.org/10.1061/(ASCE)0733-9445(1985)111:3(505), [Online]. Available: ASCE Library, http://ascelibrary.org/. Accessed: May 13, 2017.

[15] R. Grahn and P.-Å. Jansson, *Dynamik*. Lund, Sverige: Studentlitteratur, 1995.

[16] N. Mohan, T. M. Undeland, and W. P. Robbins, *Power Electronics: Converters, Applications, and Design*, 3rd ed., Hoboken, N.J., USA: John Wiley & Sons Inc, 2003.

[17] J.-K. Seok, J.-K. Lee, and D.-C. Lee, "Sensorless speed control of nonsalient permanent-magnet synchronous motor using rotor-position-tracking PI controller," *IEEE Transactions on Industrial Electronics*, vol. 53, no. 2, pp. 399-405, Apr., 2006. doi:10.1109/TIE.2006.870728, [Online]. Available: IEEE Xplore Digital Library, http://ieeexplore.ieee.org/Xplore/home.jsp. Accessed: April 12, 2017.

[18] E. Urlep and K. Jezernik, "Low and Zero Speed Sensorless Control of nonsalient PMSM," in *2007 IEEE International Symposium on Industrial Electronics*, 2007, pp. 2238-2243. [Online]. Available: http://ieeexplore.ieee.org.proxy.lib.chalmers.se/document/4374956/. Accessed: April 12, 2017.

[19] R. Krishnan, *Permanent Magnet Synchronous and Brushless DC Motor Drives*, CRC Press/Taylor & Francis, 2010.

[20] H. Zhaobin, Y. Linru, and W. Zhaodong, "Sensorless initial rotor position identification for non-salient permanent magnet synchronous motors based on dynamic reluctance difference," *IET Power Electronics*, vol. 7, no. 9, pp. 2336-2346, Sept, 2014. doi:10.1049/iet-pel.2013.0720, [Online]. Available: IEEE Xplore Digital Library, http://ieeexplore.ieee.org/Xplore/home.jsp. Accessed: February 7, 2017.

[21] Y. Li, H. Lu, W. Qu, S. Sheng, and Z. Wang, "Sensorless control of PMSM based on low frequency voltage injection at low speeds and standstill," in *2013 IEEE*

ECCE Asia Downunder (ECCE Asia), 2013, pp. 781-787. [Online]. Available: http://ieeexplore.ieee.org/document/6579191/. Accessed: February 7, 2017.

[22] A. Consoli, G. Scarcella, and A. Testa, "Sensorless control of PM synchronous motors at zero speed," in *1999 IEEE Industry Applications Conference. Thirty-Forth IAS Annual Meeting*, 1999, pp. 1033-1040. [Online]. Available: http://ieeexplore.ieee.org/document/801632/. Accessed: February 7, 2017.

[23] J. Agrawal and S. Bodkhe, "Experimental Study of Low Speed Sensorless Control of PMSM Drive Using High Frequency Signal Injection," *Advances in Electrical and Electronic Engineering*, vol. 14, no. 1, pp. 29-39, Mar., 2016. doi:10.15598/aeee.v14i1.1564, [Online]. Available: ProQuest Central, http://search.proquest.com/. Accessed: February 14, 2017.

[24] J.-H. Jang, J.-I. Ha, M. Ohto, K. Ide, and S.-K. Sul, "Analysis of permanent-magnet machine for sensorless control based on high-frequency signal injection," *IEEE Transactions on Industry Applications*, vol. 40, no. 6, pp. 1595-1604, Nov., 2004. doi:10.1109/TIA.2004.836222, [Online]. Available: IEEE Xplore Digital Library, http://ieeexplore.ieee.org/Xplore/home.jsp. Accessed: February 23, 2017.

[25] O. Wallmark, L. Harnefors, and O. Carlson, "Sensorless control of PMSM drives for hybrid electric vehicles," in *2004 IEEE 35th Annual Power Electronics Specialists Conference*, 2004, pp. 4017-4023. [Online]. Available: http://ieeexplore.ieee.org/document/1355186/. Accessed: February 16, 2017.

[26] Y. Zhao, "Position/speed sensorless control for permanent-magnet synchronous machines," Ph.D. dissertation, Electrical Engineering, University of Nebraska, Lincoln, USA, 2014. [Online]. Available: http://proxy.lib.chalmers.se/login?url=http://search.proquest.com.proxy.lib.chalmers.se/docview/1530422555?accountid=10041. Accessed: February 23, 2017.

[27] P. García, D. Reigosa, F. Briz, C. Blanco, and J. M. Guerrero, "Sensorless control of surface permanent magnet synchronous machines using the high frequency resistance," in *2011 IEEE Energy Conversion Congress and Exposition*, 2011, pp. 2709-2716. [Online]. Available: http://ieeexplore.ieee.org.proxy.lib.chalmers.se/document/6064132/. Accessed: February 24, 2017.

[28] X. Luo, Q. Tang, A. Shen, and Q. Zhang, "PMSM Sensorless Control by Injecting HF Pulsating Carrier Signal Into Estimated Fixed-Frequency Rotating Reference Frame," *IEEE Transactions on Industrial Electronics*, vol. 63, no. 4, pp. 2294-2303, Apr., 2016. doi:10.1109/TIE.2015.2505679, [Online]. Available: IEEE Xplore Digital Library, http://ieeexplore.ieee.org/Xplore/home.jsp. Accessed: February 16, 2017.

[29] J. Holtz, "Acquisition of Position Error and Magnet Polarity for Sensorless Control of PM Synchronous Machines," *IEEE Transactions on Industry Applications*, vol. 44, no. 4, pp. 1172-1180, Jul., 2008. doi:10.1109/TIA.2008.921418, [Online]. Available: IEEE Xplore Digital Library, http://ieeexplore.ieee.org/Xplore/home.jsp. Accessed: February 16, 2017.

[30] S. Bolognani, S. Calligaro, and R. Petrella, "Sensorless quasi-standstill and very low-speed position detection in non-salient PMSMs based on current injection and back-EMF observer," in *3rd IEEE International Symposium on Sensorless Control for Electrical Drives (SLED 2012)*, 2012, pp. 1-7. [Online]. Available: http://ieeexplore.ieee.org.proxy.lib.chalmers.se/document/6422813/. Accessed: April 13, 2017.

[31] R. Antonello, F. Tinazzi, and M. Zigliotto, "Benefits of Direct Phase Voltage Measurement in the Rotor Initial Position Detection for Permanent-Magnet Motor Drives," *IEEE Transactions on Industrial Electronics*, vol. 62, no. 11, pp. 6719-6726, Nov, 2015. doi:10.1109/TIE.2015.2448514, [Online]. Available: IEEE Xplore Digital Library, http://ieeexplore.ieee.org/Xplore/home.jsp. Accessed: January 25, 2017.

[32] Y. Wang *et al.*, "Initial Rotor Position and Magnetic Polarity Identification of PM Synchronous Machine Based on Nonlinear Machine Model and Finite Element Analysis," *IEEE Transactions on Magnetics*, vol. 46, no. 6, pp. 2016-2019, Jun., 2010. doi:10.1109/TMAG.2010.2042690, [Online]. Available: IEEE Xplore Digital Library, http://ieeexplore.ieee.org/Xplore/home.jsp. Accessed: February 16, 2017.

[33] X. Wu, H. Wang, S. Huang, K. Huang, and L. Wang, "Sensorless Speed Control with Initial Rotor Position Estimation for Surface Mounted Permanent Magnet Synchronous Motor Drive in Electric Vehicles," *Energies*, vol. 8, no. 10, pp. 11030-11046, Oct., 2015. doi:10.3390/en81011030, [Online]. Available: MDPI Open Access Journals, http://www.mdpi.com/1996-1073/8/10/11030. Accessed: February 15, 2017.

[34] D.D. Reigosa, F. Briz, M.W. Degner, P. García, and J. M. Guerrero, "Temperature Issues in Saliency-Tracking-Based Sensorless Methods for PM Synchronous Machines," *IEEE Transactions on Industry Applications*, vol. 47, no. 3, pp. 1352-1360, May, 2011. doi:10.1109/TIA.2011.2126033, [Online]. Available: IEEE Xplore Digital Library, http://ieeexplore.ieee.org/Xplore/home.jsp. Accessed: April 11, 2017.

[35] Y. Hua, M. Sumner, G. Asher, Q. Gao, and K. Saleh, "Improved sensorless control of a permanent magnet machine using fundamental pulse width modulation excitation," *IET Electric Power Applications*, vol. 5, no. 4, pp. 359-370, Apr. 2011. doi:10.1049/iet-epa.2010.0108, [Online]. Available: IEEE Xplore Digital Library, http://ieeexplore.ieee.org/Xplore/home.jsp. Accessed: April 14, 2017.

[36] Q. Gao, G. M. Asher, M. Sumner, and P. Makys, "Position Estimation of AC Machines Over a Wide Frequency Range Based on Space Vector PWM Excitation," *IEEE Transactions on Industry Applications*, vol. 43, no. 4, pp. 1001-1011, July, 2007. doi:10.1109/TIA.2007.900464, [Online]. Available: IEEE Xplore Digital Library, http://ieeexplore.ieee.org/Xplore/home.jsp. Accessed: April 14, 2017.

[37] Y. Hua, G.M. Asher, M. Sumner, and Q. Gao, "Sensorless Control of Surface Mounted Permanent Magnetic Machine Using the Standard Space Vector PWN," in *2007 IEEE Industry Applications Annual Meeting*, 2007, pp. 661-667. [Online]. Available:

http://ieeexplore.ieee.org.proxy.lib.chalmers.se/document/4347854/. Accessed: April 14, 2017.

[38] Y. Duan and M. Sumner, "A novel current derivative measurement using recursive least square algorithms for sensorless control of permanent magnet synchronous machine," in *Proceedings of The 7th International Power Electronics and Motion Control Conference*, 2012, pp. 1193-1200. [Online]. Available: http://ieeexplore.ieee.org.proxy.lib.chalmers.se/document/6259005/. Accessed: April 14, 2017.

[39] M. Schroedl, "Sensorless control of AC machines at low speed and standstill based on the "INFORM" method," in *Industry Applications Conference, 1996. Thirty-First IAS Annual Meeting, IAS '96.*, 1996, pp. 270-277. [Online]. Available: http://ieeexplore.ieee.org.proxy.lib.chalmers.se/document/557028/. Accessed: April 14, 2017.

[40] R. Ni, K. Lu, F. Blaabjerg, and D. Xu, "A comparative study on pulse sinusoidal high frequency voltage injection and INFORM methods for PMSM position sensorless control," in *IECON 2016 - 42nd Annual Conference of the IEEE Industrial Electronics Society*, 2016, pp. 2600-2605. [Online]. Available: http://ieeexplore.ieee.org.proxy.lib.chalmers.se/document/7793021/. Accessed: April 14, 2017.

[41] M. Schrödl and C. Simetzberger, "Sensorless control of PM synchronous motors using a predictive current controller with integrated INFORM and EMF evaluation," in *2008 13th International Power Electronics and Motion Control Conference*, 2008, pp. 2275-2282. [Online]. Available: http://ieeexplore.ieee.org.proxy.lib.chalmers.se/document/4635602/. Accessed: April 13, 2017.

[42] T. Glad and L. Ljung, *Reglerteknik: Grundläggande teori*. 4th ed., Lund, Sweden: Studentlitteratur AB, 2014.

[43] J. Lee *et al.*, "Sensorless Control of Surface-Mount Permanent-Magnet Synchronous Motors Based on a Nonlinear Observer," *IEEE Transactions on Power Electronics*, vol. 25, no. 2, pp. 290-297, Feb. 2010. doi:10.1109/TPEL.2009.2025276, [Online]. Available: IEEE Xplore Digital Library, http://ieeexplore.ieee.org/Xplore/home.jsp. Accessed: March 23, 2017.

[44] J.A. Solsona and M.I. Valla, "Disturbance and nonlinear Luenberger observers for estimating mechanical variables in permanent magnet synchronous motors under mechanical parameters uncertainties," *IEEE Transactions on Industrial Electronics*, vol. 50, no. 4, pp. 717-725, Aug. 2003. doi:10.1109/TIE.2003.814866, [Online]. Available: IEEE Xplore Digital Library, http://ieeexplore.ieee.org/Xplore/home.jsp. Accessed: May 21, 2017.

[45] F. Abry, A. Zgorski, X. Lin-Shi and J.-M. Retif, "Sensorless position control for SPMSM at zero speed and acceleration," in *Proceedings of the 2011 14th European Conference on Power Electronics and Applications*, 2011, pp. 1-9. [Online]. Available: http://ieeexplore.ieee.org/document/6020505/. Accessed: May 19, 2017.

[46] L. Jiaxi, Y. Guijie, and Y. Pengfei, "Rotor Position Estimation for PMSM Based on Sliding Mode Observer," in *2007 International Conference on Mechatronics and Automation*, 2007, pp. 3684-3689. [Online]. Available:

http://ieeexplore.ieee.org.proxy.lib.chalmers.se/document/4304159/. Accessed: April 13, 2017.

[47] R. Yan, B. Li, and F. Zhou, "Sensorless control of PMSMs based on parameter-optimized MRAS speed observer," in *2008 IEEE International Conference on Automation and Logistics*, 2008, pp. 1573-1578. [Online]. Available: http://ieeexplore.ieee.org.proxy.lib.chalmers.se/document/4636404/. Accessed: April 13, 2017.

[48] J. Hu, L. Xu, and J. Liu, "Magnetic Pole Identification for PMSM at Zero Speed Based on Space Vector PWM," in *2006 CES/IEEE 5th International Power Electronics and Motion Control Conference*, 2006, pp. 1-5. [Online]. Available: http://ieeexplore.ieee.org/document/4778074/. Accessed: February 15, 2017.

[49] D. Raca, P. García, D.D. Reigosa, F. Briz, and R.D. Lorenz, "Carrier-Signal Selection for Sensorless Control of PM Synchronous Machines at Zero and Very Low Speeds," *IEEE Transactions on Industry Applications*, vol. 46, no. 1, pp. 167-178, Jan., 2010. doi:10.1109/TIA.2009.2036551, [Online]. Available: IEEE Xplore Digital Library, http://ieeexplore.ieee.org/Xplore/home.jsp. Accessed: February 14, 2017.

[50] M. Barcaro, M. Morandin, T. Pradella, N. Bianchi, and I. Furlan, "Iron saturation impact on high frequency sensorless control of synchronous permanent magnets motor," in *2016 XXII International Conference on Electrical Machines (ICEM)*, 2016, pp. 1085-1091. [Online]. Available: http://ieeexplore.ieee.org/document/7732660/. Accessed: February 7, 2017.

[51] Mathworks, "Second-Order Filter," mathworks.com, 2017. [Online]. Available: https://se.mathworks.com/help/physmod/sps/powersys/ref/secondorderfilter.html. Accessed: May 19, 2017.

[52] A. R. Setty, S. Wekhande, and K. Chatterjee, "Comparison of high frequency signal injection techniques for rotor position estimation at low speed to standstill of PMSM," in 2012 IEEE 5th India International Conference on Power Electronics (IICPE), 2012, pp. 1-6. [Online]. Available: http://ieeexplore.ieee.org/document/6450521/.

A

Appendix: Derivation of the SPMSM State-Space Model

In this part, the nonlinear state-space model of the SPMSM is going to be derived. Starting with (2.13) and writing it in d- and q-components respectively, then the electrical machine model becomes

$$u_{d,s} = R_s \cdot i_{d,s} + l_{dd} \cdot \frac{di_{d,s}}{dt} + l_{dq} \cdot \frac{di_{q,s}}{dt} - \omega_r L_q \cdot i_{q,s} \tag{A.1}$$

$$u_{q,s} = R_s \cdot i_{q,s} + l_{qq} \cdot \frac{di_{q,s}}{dt} + l_{qd} \cdot \frac{di_{d,s}}{dt} + \omega_r (L_d \cdot i_{d,s} + \lambda_{PM}) \tag{A.2}$$

where $l_{dd} = \frac{\partial \lambda_{d,s}}{i_{d,s}}$, $l_{dq} = \frac{\partial \lambda_{d,s}}{i_{q,s}}$, $l_{qd} = \frac{\partial \lambda_{q,s}}{i_{d,s}}$, and $l_{qq} = \frac{\partial \lambda_{q,s}}{i_{q,s}}$ and these represent the incremental inductances in the dq-frame which are also found in (2.14). The mechanical machine model is still the same as in (2.16) to (2.17).

The following state vector is chosen, $\underline{x} = \{x_1, x_2, x_3, x_4\}$

$$x_1 = i_{d,s}, x_2 = i_{q,s}, x_3 = \omega_r, x_4 = \theta_r \tag{A.3}$$

where ω_r and θ_r are the electrical speed and position respectively. Hence, the time derivative of the state vector $\underline{x}$ is written as $\underline{\dot{x}}$ and its elements are

$$\dot{x}_1 = \frac{di_{d,s}}{dt}, \dot{x}_2 = \frac{di_{q,s}}{dt}, \dot{x}_3 = \frac{d\omega_r}{dt}, \dot{x}_4 = \frac{d\theta_r}{dt} \tag{A.4}$$

Further, the following outputs are chosen, $\underline{y} = \{y_1, y_2, y_3, y_4, y_5, y_6, y_7, y_8, y_9, y_{10}, y_{11}, y_{12}\}$

$$\begin{aligned} &y_1 = i_{d,s}, y_2 = i_{q,s}, y_3 = T_e, y_4 = \Omega_r, y_5 = \theta_{r,mech}, y_6 = L_d, \\ &y_7 = L_q, y_8 = l_{dd}, y_9 = l_{dq}, y_{10} = l_{qd}, y_{11} = l_{qq}, y_{12} = T_L. \end{aligned} \tag{A.5}$$

where Ω_r is the mechanical speed and $\theta_{r,mech}$ is the mechanical rotor position. The inputs to the machine is chosen as $\underline{u} = \{u_1, u_2, u_3\} = \{u_{d,s}, u_{q,s}, T_{L,ext}\}$.

In order to find the final state-space expressions of the machine model, the derivatives of the current components in (A.1) and (A.2) should be solved for. But as can be seen, $u_{d,s}$ and $u_{q,s}$ depend on both d- and q-current components as well as on their derivatives. Hence, in this derivation, the d-current derivative in (A.1) is solved for first and written as a function of the q-current component and its derivative yielding a nonlinear expression. Then, the q-current derivative in (A.2)

is solved for and the expression for the d-current derivative is used. Therefore, it should be possible to use these state-space equations by first calculating the q-current derivative and then use this to get the d-current derivative. So, the d-current derivative from (A.1) is expressed as

$$\frac{di_{d,s}}{dt} = \frac{1}{l_{dd}} \cdot (u_{d,s} - R_s \cdot i_{d,s} - l_{dq}\frac{di_{q,s}}{dt} + \omega_r L_q \cdot i_{q,s}). \tag{A.6}$$

Inserting (A.6) into (A.2) and solving for the q-current derivative yield

$$\begin{aligned} u_{q,s} = R_s \cdot i_{q,s} + l_{qq} \cdot \frac{di_{q,s}}{dt} + l_{qd} \cdot \left[\frac{1}{l_{dd}} \cdot (u_{d,s} - R_s \cdot i_{d,s} - l_{dq}\frac{di_{q,s}}{dt} + \omega_r L_q \cdot i_{q,s})\right] \\ + \omega_r(L_d \cdot i_{d,s} + \lambda_{PM}) \end{aligned} \tag{A.7}$$

and rewriting (A.7) yields

$$\begin{aligned} u_{q,s} = R_s\Big(i_{q,s} - \frac{l_{qd}}{l_{dd}} i_{d,s}\Big) + \frac{di_{q,s}}{dt}\Big(\frac{l_{dd}l_{qq} - l_{dq}l_{qd}}{l_{dd}}\Big) \\ + \omega_r\Big(\frac{l_{qd}}{l_{dd}} L_q \cdot i_{q,s} + L_d \cdot i_{d,s} + \lambda_{PM}\Big) + \frac{l_{qd}}{l_{dd}} u_{d,s}. \end{aligned} \tag{A.8}$$

Notice that the d-current derivative is not existent in (A.8) and the q-current time derivative can thus be solved for easily and may be expressed as

$$\begin{aligned} \frac{di_{q,s}}{dt} = \frac{l_{dd}}{l_{dd}l_{qq} - l_{dq}l_{qd}}\Bigg(u_{q,s} - R_s\Big(i_{q,s} - \frac{l_{qd}}{l_{dd}} i_{d,s}\Big) \\ - \omega_r\Big(\frac{l_{qd}}{l_{dd}} L_q \cdot i_{q,s} + L_d \cdot i_{d,s} + \lambda_{PM}\Big) - \frac{l_{qd}}{l_{dd}} u_{d,s}\Bigg). \end{aligned} \tag{A.9}$$

Concluding the electrical state-space derivation, the time derivative of states x_1 and x_2 are described in (A.6) and (A.9) respectively. The cross-coupling effects are a result of the general machine modelling made in Section 2.2.2. Further, since the incremental inductances are nonlinear functions of the current components, these add extra nonlinearity to the equations.

Continuing the state-space representation of the machine using the mechanical equations found in (2.16), (2.17), and (2.19), the nonlinear state-space model of the SPMSM can be described using the following four main equations

$$\dot{x}_1 = \frac{1}{l_{dd}} \cdot (u_1 - R_s \cdot x_1 - l_{dq} \cdot \dot{x}_2 + x_3 \cdot L_q \cdot x_2) \tag{A.10}$$

$$\begin{aligned} \dot{x}_2 = \frac{l_{dd}}{l_{dd}l_{qq} - l_{dq}l_{qd}}\Bigg(u_2 - R_s\Big(x_2 - \frac{l_{qd}}{l_{dd}} x_1\Big) \\ - x_3\Big(\frac{l_{qd}}{l_{dd}} L_q \cdot x_2 + L_d \cdot x_1 + \lambda_{PM}\Big) - \frac{l_{qd}}{l_{dd}} u_1\Bigg) \end{aligned} \tag{A.11}$$

$$\dot{x}_3 = \frac{n_p}{J} \cdot \left(\frac{3n_p}{2} \cdot \left[\lambda_{PM} \cdot x_2 + (L_d - L_q) \cdot x_1 \cdot x_2 \right] - T_L \right) \tag{A.12}$$

$$\dot{x}_4 = x_3. \tag{A.13}$$

The load torque is modelled as below

$$T_L = \begin{cases} T_e & \text{if standstill and } |T_e| \leq C \\ \mu_k mgr \cdot sign(\omega_r)/k + T_{L,ext} & \text{else} \end{cases}$$

where $C = \mu_s mgr/k$ is the static friction torque (in later simulations C is swept to several values), μ_s is the static friction coefficient, μ_k is the kinetic friction coefficient, m is the mass of the concrete drill, g is the gravitational constant, r is the radius of the drill bit, k is the gear box ratio (high speed versus low speed), and $T_{L,ext}$ is an extra load torque constant which could be used e.g. to apply load steps.

When the electric torque is less than (or equals) the static friction and the machine is standstill, (A.12) is set to zero to mimic the effects of static friction. This implies that the load torque equals the electric torque according to (A.12). As the electric torque overcomes the static friction, (A.12) is used as it is and the load torque equals the kinetic friction torque and the extra load torque $T_{L,ext}$.